Numerical and experimental study of silicon crystallisation by Kyropoulos process for photovoltaic applications

Ahmed Nouri

THÈSE

Pour obtenir le grade de

DOCTEUR DE L'UNIVERSITE DE GRENOBLE ALPES

Préparée dans le cadre d'une cotutelle internationale *entre l'Université Grenoble Alpes* et l'Université de Laghouat
Spécialité : Matériaux, mécanique, génie civil, électrochimie

Présentée par
Ahmed Nouri

Thèse dirigée par **Kader Zaidat** et **Iben Khaldoun Lefkaier**
et codirigée par **Yves Delannoy, Guy Chichignoud** et **Bachir Helifa**

préparée au sein des laboratoires : SIMaP-EPM et LPM
dans Les écoles Doctorale : IMEP-2 et SM

Numerical and Experimental study of silicon crystallisation by Kyropoulos process for photovoltaic applications

Thèse soutenue publiquement le **07 Mars 2017**.
devant le jury composé de :

M. Kheirreddine, Lebbou
Directeur de recherche à l'Université de Lyon 1, (Président)
M. Matias Velázquez
Chargé de recherche à l'institut ICMCB, CNRS, Bordeaux, (Rapporteur)
M. Aissa Belgacem-Bouzida
Professeur à l'Universite de Batna, (Rapporteur)
M. Bachir Bentria
Professeur, Université de Laghouat, (Examinateur)
M. Kader Zaidat
Professeur à l'Université Grenoble Alpes, (Directeur de Thèse)
M. Iben Khaldoun Lefkaier
Professeur à l'Université de Laghouat, (Directeur de Thèse)
M. Yves Delannoy
Professeur à l'Université Grenoble Alpes, (Co-Directeur de Thèse)
M. Guy Chichignoud
Chargé de recherche, CNRS, Grenoble, (Co-Directeur de Thèse)
M. Bachir Helifa
Maitre de conférences, Université de Laghouat, (Co-Directeur de Thèse)

To those who believe in a better world for the future generations . . .

To my family.

Abstract

Kyropoulos technique is a top seeding crystal growth process with the potential to produce large diameter ingots of high crystalline quality. The crystal grows inside the melt at low thermal gradient without contact with the crucible. Despite its advantages, the technique has not been fully investigated for the production of silicon.

3D numerical modeling of the full furnace was performed to understand the effect of heat transfer and fluid dynamics on solidification. An experimental Kyropoulos setup with a square crucible and three heating elements (top, bottom and side heaters) was developed in parallel to grow silicon ingots for photovoltaic applications.

The obtained numerical results explained why no growth was possible in the starting configuration. Radiation heating was more concentrated on the center and heat loss from the sides was high. The addition of a radiation shield tube in the central zone and the increase of side heating created a cold area around the seeding zone. Growth from the seed was possible in these conditions and crystal enlargement was achieved by decrease of power in the upper heater. To enhance the growth conditions, a third configuration was created by adding a cold heat sink in the top to provide local central cooling of the melt and better heat extraction from the seed.

The crystal growth in Kyropoulos process for silicon was found to be sensitive to symmetry loss. Numerical investigation showed that a strong coupled effect between radiations heat exchange in the top and melt flow is the leading cause for dissymmetric growth. The sudden increase of emissivity of silicon during solidification coupled with the slowdown of melt flow near the crystal increased the growth rate of any appearing dissymmetry towards one preferential direction. Control of the top radiation cooling, by keeping the top heater temperature close to melting point, and addition of crystal rotation to homogenize the melt allowed a consistent symmetric crystal growth.

The investigation showed that it is possible to control the shape of the final ingot to have a square horizontal section using two main approaches: by fluid dynamics control or by structural growth kinetics control.

Numerical simulation showed that it is possible to have a square horizontal cross section of the ingot using the balance between heat diffusion and advection in the melt. Two different cases could be obtained according to the values of Peclet number. For the case of higher Peclet number, the square horizontal cross section was made by the flow coming from the four corners

of the crucible, while in the case of lower Peclet number , the crystal square horizontal cross section was inherited directly from the walls of the crucible. For the latter case, the square shape of the ingot section could not be fully completed in the corners due to the localized effect of higher Peclet number in the corners.

Structural growth kinetics control was also used to obtain a square ingot cross section. The developed experimental prototype succeeded to stabilize monocrystalline faceted growth in the <111> direction giving silicon crystals with a perfectly square horizontal cross section.

Résumé

Le procédé Kyropoulos et un procédé de croissance cristalline par trempe de germe permettant potentiellement de produire des lingots de grand diamètre et de haute qualité cristalline. La croissance progresse dans un bain à faible gradient thermique et sans contact avec le creuset. Malgré ses avantages, le procédé Kyropoulos n'a pas été exploité pour la production du silicium.

Le présent travail a pour but d'étudier l'utilisation du procédé Kyropoulos pour produire des cristaux de silicium de haute qualité avec une section horizontale carrée. Un model numérique 3D du processus, avec calcule de la thermique, de la mécanique des fluides et de la solidification, a été créé pour comprendre l'effet des transferts thermiques et de la mécanique des fluides sur la solidification.

Un dispositif expérimental doté d'un creuset carré et de trois zones de chauffe (haut, bas et coté) a été développé en parallèle pour faire croitre des cristaux de silicium pour des applications photovoltaïques.

L'analyse numérique a permis de comprendre l'effet de la répartition du chauffage par rayonnement au-dessus de la charge de silicium et de quantifier les pertes thermiques à travers les côtés dans le dispositif expérimental. Ces bilant ont permis de développer différente configurations fonctionnelles du four. L'ajout d'un écran contre le rayonnement autour de la zone de trempe et l'augmentation du chauffage des cotés ont permis de créer une zone froide autour du germe et d'orienter les boucles de convection pour devenir descendantes au centre. La croissance à partir du germe était possible par diminution de la puissance dans l'élément chauffant du haut. Afin d'améliorer encore les conditions de croissance, une troisième configuration du procédé a été développée par l'ajout d'un échangeur thermique froid autour du

germe pour augmenter le refroidissement de la zone centrale et améliorer l'extraction de chaleur à partir du germe.

L'étude a montré que le procédé Kyropoulos pour le silicium est sensible à la croissance dissymétrique. La cause principale pour cette dissymétrie de croissance étant un effet conjugué entre l'augmentation de refroidissement par rayonnement, lié au changement d'émissivité du silicium durant la solidification, et le ralentissement des boucles de convection dans le bain du côté du cristal. Le contrôle du rayonnement, en gardant la température de l'élément chauffant du haut proche de la température de fusion du silicium, et l'homogénéisation du bain par ajout de la rotation du cristal ont permis d'avoir une croissance symétrique du cristal à partir du germe.

Le présent travail propose deux méthodes de contrôle possibles pour obtenir une section horizontale carrée du lingot de silicium: un control basé sur la mécanique des fluides et un control basé sur la cinétique de croissance structurale.

Les résultats numériques montrent qu'il est possible d'obtenir un lingot de section horizontale carrée en utilisant les transferts thermiques par diffusion et par advection dans le bain. Deux cas peuvent être distingués suivant le nombre de péclet: dans le cas à nombre de péclet élevé la forme carrée de la section horizontale du lingot est issue de l'écoulement venant des quatre coins du creuset, tandis que dans le cas à faible nombre de Péclet, la forme carrée de la section horizontale du lingot est issue directement des faces du creuset. Pour ce dernier cas, la forme de la section horizontale du lingot n'était pas complètement carrée aux coins à cause d'un fort écoulement localisé dans les coins.

Pour le cas de contrôle de forme par la cinétique de croissance structurale, le prototype expérimental développé a permis de stabilisé la croissance facettée des facettes <111> dans le silicium donnants des mono cristaux de section horizontale de forme carré.

Acknowledgement

I would like to express my sincere thanks to my phD director dr Kader Zaidat for his guidance, patience, and continuous feedback. His effort to provide opportunities for discovery and acquirement of new scientific insight made this thesis an ongoing adventure.

I would like to thank my phD director Khaled Lefkaier for his guidance and encouragements. His remarks and advises were a great support to reshape my choices in order to accomplish this work.

I would like to thank my co-director Yves Delannoy for his most appreciated guidance and support. I am grateful that he made himself available to help and guide me through this work. His incisive insight have been an important asset during this work.

I would like to thank my co-director Guy Chichignoud for his constant support and guidance. His investment in my thesis was a foundation that helped to shape this work.

I would like to thank my co-director Bachir Helifa for his valorous availability and guidance. His will to support me unconditionally gave me confidence to move forward and beyond.

I would like to thank the members of the jury who honored me by accepting to review and comment my work

I am grateful to Professor Thierry Duffar for receiving me for discussions. His valuable explanations and comment are most appreciated.

I am also thankful to Professor Yves Fautrelle for accepting to discuss my work.

I am grateful to Professor Koichi Kakimoto for receiving me in his laboratory. I am most thankful for the valuable discussions that brought great insight into my work.

I am also thankful to Dr Gao Bing and Dr Satoshi Nakano for their kind availability and contribution in this work.

I am deeply grateful to our most appreciated engineering and technical team at SIMaP-EPM laboratory for their help and support.

I am thankful to Dr Francois LISSALDE for welcoming me in Cyberstar Company. Our discussion were most appreciated.

I am thankful to the team of our project partners in CEA-INES for the valuable and most appreciated discussions.

I would like to thank all the members in our EPM-SIMaP laboratory who were generously available for help and advice. I am also grateful to my friends and fellow student phD in the laboratory for the amazing good company and well appreciated discussions.

I acknowledge the efforts of our administrative team in SIMaP laboratory as well as in the Doctorate school IMEP-2 who provided the best environment to complete this work.

The funding for this work was provided by The French National Research Agency (ANR) and the Tenerrdis Competitive Pole.

List of abbreviations and Symbols

DS	*Directional solidification*	
CZ	*Czochralski process*	
HEM	*Heat exchange method*	
DO	*discrete ordinate radiation model*	
S2S	*Surface to surface radiation model*	
T_0	*Melting temperature*	*°C*
ρ_s	*Density solid*	*kg / m³*
ρ_l	*Density liquid*	*kg / m³*
η	*Dynamic viscosity*	*kg / (m s)*
λ_s	*Heat conductivity solid*	*W / (m K)*
λ_l	*Heat conductivity liquid*	*W / (m K)*
ε_S	*emissivity of solid*	*-*
ε_L	*emissivity of liquid*	*-*
T_m	*Melting temperature*	*°C*
ρ	*Density*	*Kg / m³*
μ	*Dynamic viscosity*	*Kg / (m s)*
Cp	*Specific heat*	*J / (kg K)*
β	*Volumetric expansion rate*	*1 / K*
α	*Thermal diffusivity*	*m² / s*
Q_L	*Latent heat*	*j / kg*
γ	*Marangoni parameter*	*N / (m K)*
ε_{eq}	*Equivalent emissivity*	*-*
σ	*Boltzman constant*	*j/K*
T_{ext}	*Exterior temperature*	*°C*
T_{wall}	*wall temperature*	*°C*
h	*Convective heat transfer coefficient*	*W/(m²k)*
T_{ar}	*Argon temperature*	*°C*
ΔT	*Temperature difference*	*°C*
U	*Velocity*	*m / s*
η_{eff}	*Effective thermal conductivity*	*J / (kg K)*
η_{tur}	*turbulent thermal conductivity*	*J / (kg K)*
L	*Characteristic length*	*m*
G	*Gravitational acceleration*	*m / s²*
f_{buo}	*Buoyancy volumetric force*	*N/m³*
f_{vis}	*viscous volumetric force*	*N/m³*

f_{mar}	*Marangoni volumetric force*	N/m^3
Uref	*Reference velocity*	*m / s*
Cp	*Heat capacity*	*J*
ν	*Kinematic viscosity*	m^2 / s
T_{sol}	*Solidus temperature*	*K*
T_{liq}	*liquidus temperature*	*K*
S	*Momentum sink term*	
A_{mush}	*Mushy zone parameter*	$kgm^{-3}s^{-1}$
$\vec{v}$	*Melt velocity vector*	*m/s*
$\overrightarrow{v_p}$	*pull velocity vector*	*m/s*
τ	*Characteristic braking time*	*s*
Q_{rad}	*radiative heat exchange*	*J*
Q_{conv}	*convective heat exchange*	*J*
ε_0	*Small number*	
Pr	*Prandtl number*	
Gr	*Grashoff number*	
Pe	*Péclet number*	
f_L	*Liquid fraction*	

Table of Figures

List of Tables

Table of Contents

General Introduction

The energy company proposed to cover the electricity consumption in my apartment from renewable sources for an additional fees of 2 euros per month. Regardless all its virtues, renewable energy is still not the default choice due to the lack of cost effectiveness. The motivation behind the present work is part of the actual global effort to develop alternative processes that has the potential to produce high quality silicon ingots with the possibility of cost reduction . . .

One of the most expensive steps in the production of photovoltaic solar cells based on crystalline silicon is the production of the wafer. The actual dominating growth processes for the production of monocrystalline silicon are still not fully cost effective for photovoltaic applications.

The production methods of high quality monocrystalline ingots have reached limitations of shape and size control due to instability issues. On the actual market, there is no mature technique applied to silicon that can promote a larger size monocrystalline ingots with a flat aspect ratio. In addition, the actual dominating seeding techniques for the production of silicon ingots do not offer shape control, in order to obtain a square ingot geometry.

The present work investigates a less common technique for silicon process, named Kyropoulos technique, as a promising alternative for the production of large flat silicon ingots. This technique, very well known for sapphire production, offers several advantages making it a good candidate for the production of high quality silicon single crystals for photovoltaic applications. In the literature, only one experimental investigation of Ravishankar [1] presented in 1985 a high efficiency crystalline silicon solar cells obtained from an ingot produced by Kyropoulos technique. Regardless these promising results, the process was not further explored. This top seeding technique is highly complex and requires advanced investigation tools, such as 3D numerical simulation, for the development of liability and reproducibility.

Kyropoulos process provides an unconfined crystal growth environment at low thermal gradient with a possibility to reshape the cross horizontal section of the ingot into a square shape. In theory, the ingot horizontal growth is only limited by the crucible size; thus, the technique can increase the total mass growth rate. The listed advantages fits well for the production of monocrystalline silicon ingots intended for the photovoltaic industry with a potential decrease of the final cost.

The process has an unstable thermal configuration where the top part of the melt is at lower temperature. Such solidification processes at high temperature are extremely hard to monitor by experimental observation which slows down considerably there development. The main objective of the thesis is to promote the development of a working experimental Kyropoulos

process for silicon using numerical simulation. A direct insight into the ongoing coupled complex physical phenomena is required to answer the following needs:

- Understanding the, convective and radiative, heat fluxes exchanged inside the furnace
- Redesigning the furnace geometry and finding the working parameters to make the seeding point as the coldest zone in the melt.
- Understanding the required heat extraction approach to enlarge the ingot diameter from the seed without contact with the crucible walls.
- Understanding the effect of convection on the resulting final shape and dimensions of the final ingot.
- Studying the effect of inter-coupled phenomena on solidification interface as well as the stability of symmetry growth

An experimental part of the thesis validated the resulting development from the numerical investigations. This work was a part of a research project named PICKS project (Procédé Innovant de Croissance Kyropoulos for Silicon). The goal of this project was to investigate and develop a Kyropoulos process to produce monocrystalline silicon ingots for photovoltaic applications. The project was composed of several main tasks shared by three organizations. CyberStar industrial partner was the constructor of the furnace. CEA-INES laboratory was responsible for the characterisation of the obtained crystals for solar cells production and the development of reusable crucibles. EPM-SIMaP laboratory was in charge of the experimental and numerical development of Kyropoulos crystal growth process for silicon.

The thesis is organized in four main chapters.

1. The first chapter describes the existing techniques for the production of crystalline silicon as well as the actual Kyropoulos process applied mainly for the production of sapphire. Advantages and disadvantages of the different processes are discussed and compared in order to highlight the expected benefit from the application of Kyropoulos process for the production of crystalline silicon. An outlook of Kyropoulos process is then presented to get familiar with the main characteristics of the technique.

2. The second chapter details the creation of the numerical model. The different numerical tools used in the thesis are enumerated and explained. The assumptions and approximations considered in the 3D model are justified according to the ongoing physical phenomena. Measurements of experimental data coupled with numerical analysis are presented as part of the calibration process of the numerical model. The same chapter presents the experimental setups, on a construction point of view, at different stages of the development process.

3. The third chapter presents the numerical results for the different configurations resulting from the development process. Temperature distribution, velocity profiles and heat fluxes exchange are illustrated to explain the functioning of the furnace. Accordingly, each development step of the furnace design and working parameters is explicated based on the ongoing physical phenomena. The chapter will also discuss the limits of this process.
4. The final chapter projects the numerical analysis on the experimental crystal growth to highlight some recurring unexpected phenomena. Numerical investigation will be used to analyse the observed recurrent loss of symmetry during the growth. Solutions to grow symmetric crystals are proposed and validated numerically and experimentally. The chapter will present experimental results obtained in the present thesis showing symmetric growth of monocrystalline crystals of silicon. The presented crystals have faceted growth where the horizontal cross section, perpendicular to the crystalline orientation <100>, grows into a square shape due to the four facets <111> in silicon.

The presented results in the thesis, aims to demonstrate the feasibility and the potential of Kyropoulos technique for crystalline silicon production. A listing of several resulting outlooks is expected to resurge at the end to complement the final assessment about the full potential of the process especially concerning the process scaling for large dimensions ingots as well as the estimation of the final cost at industrial scale furnaces.

Chapter 1

I. Context and state of the art

This first chapter explains the contexts motivating the present work. It projects the investigated process on the industrial field and the actual market where it will be compared with existing processes in order to highlight its advantages and disadvantage. A state of the art concerning the evolution of the investigated process is presented in order to position the present work in the frame of the actual needs.

I.1. Motivation

The discovery of photovoltaic energy is without doubt one of the most important scientific breakthroughs; yet, its use remained limited due to its higher cost compared to the other sources of energy. Despite this reticence of the global energy market, several statements continued to insist on the importance of photovoltaic energy as a solution for rising environmental issues and strategic considerations; but, a new factor is about to reshape the considerations for the photovoltaic market. In the last decade, photovoltaic energy was reported at grid parity in several places around the world which announces a new upcoming era for solar energy.

The Photovoltaic industry will have to answer a demand for cost effective photovoltaic products satisfying several rising expectations. More efficient and elaborated production processes will be of great importance to follow the upcoming demand of a market constantly looking for lower price and higher quality.

I.1.1. Environmental and economic context

The modern human way of life is deeply dependent on an important consumption of energy. In fact, the growing demand for energy is so rapid (Figure 1. 1) that the present natural resources are not sufficient to cope with it. Increasing concerns are rising about the over depletion of our energy sources mainly fossil and nuclear.

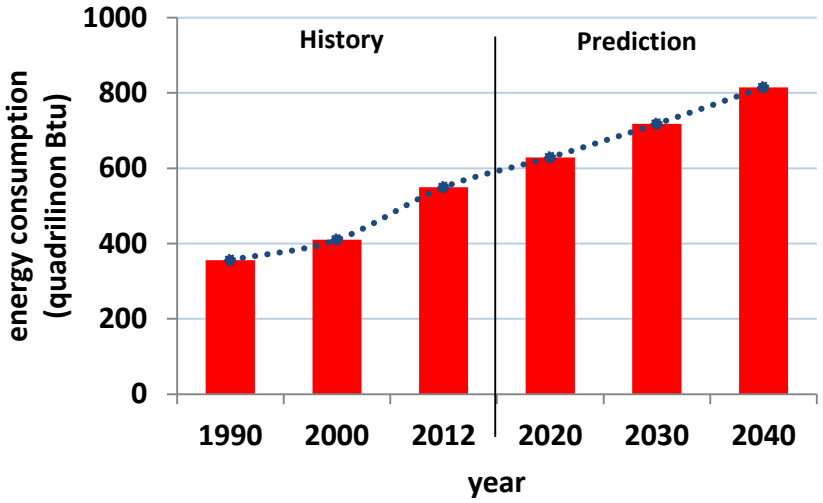

Figure 1. 1. World global energy consumption from 1990 to 2040 [1]

Furthermore, the environmental damage caused by these polluting processes to produce energy reached an alarming point jeopardizing already health and life. It became obvious beyond any doubt that these conventional sources of energy must be replaced by better alternatives. The unnatural increase of detrimental excessive CO_2 emission of the modern era is directly related to our consumption of energy. If the current growth of energy consumption should continue, which is more likely to happen, the world needs to produce at least 45% [2] of green energy to stabilize the level of CO_2 emissions at a constant threshold (Figure 1. 2).

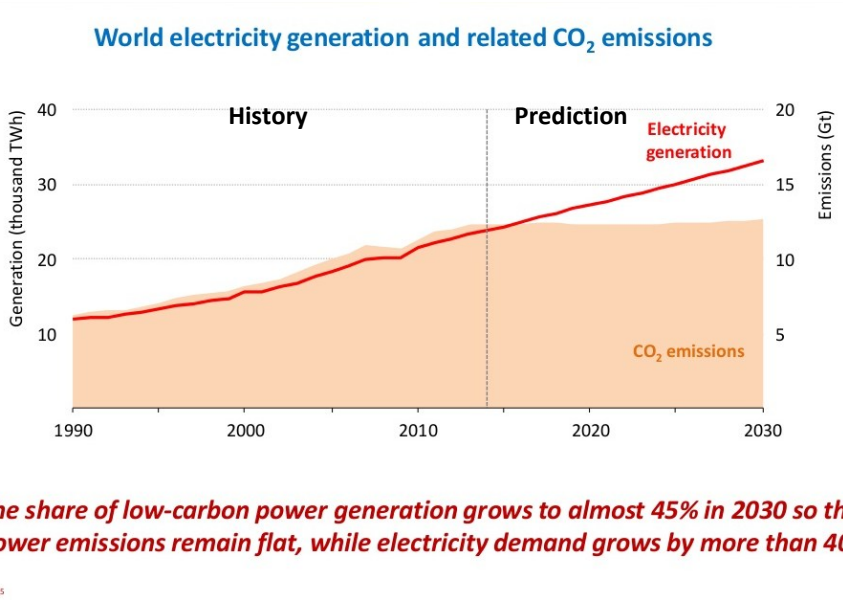

Figure 1. 2. CO_2 emissions level with world electricity generation [2]

The production of such consequent amount of clean energy is technically not possible for most of the current green energy sources in our procession. Among the several available technologies for green energy production, photovoltaic technology is actually one of the rare reliable green energy sources that could satisfy this important demand on a global scale.

Photovoltaic energy contribution to the global energy production is still quite low mainly due to economic consideration. (Figure 1. 3) Shows that, currently, only 3.5% of the global energy production is coming from photovoltaic sources. Most of this photovoltaic energy production is based on silicon. Alongside the fact that this material has the physical properties to be a major candidate for photovoltaic energy production, the interest in silicon is urged by great perspective for grow and development due to several key reasons: Firstly, the photovoltaic technology is renewable and reliable in most places; Secondly, the main raw material, Silicon, is the second most abundant element in the Earth's crust, Thirdly, silicon is a nontoxic material that can be manufactured to very high degree of purity at a reasonable cost and last but not least photovoltaic energy is simply less invasive on the environment with the potential to produce high amount of energy on more regular basics compared to other sources of green energy.

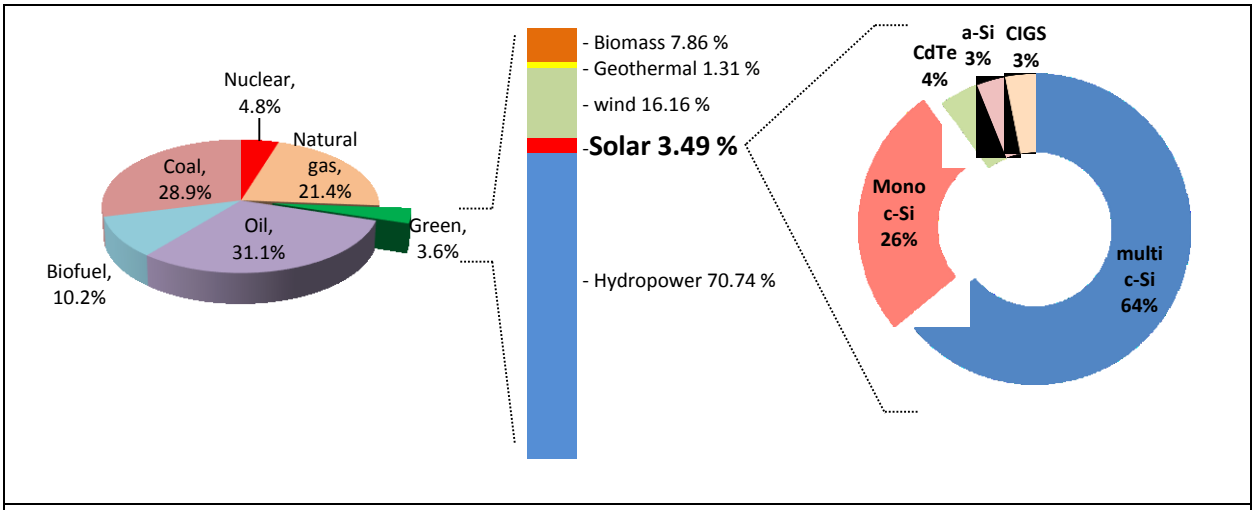

Figure 1. 3. Share contribution of different sources of energy to the global energy production market between 2013-2014 [3],[4]

The photovoltaic industry production continues to increase and more growth is expected in the upcoming years. At the present time, Different technologies are actively under development to produce photovoltaic energy; however, the crystalline silicon technology has around 90% of the market share of PV module production to date (Figure 1. 3). Compared to the other photovoltaic technologies, crystalline silicon offers good compromise between reliability, durability and efficiency in typical outdoor conditions (meteorological condition, temperature,

sun exposure). Furthermore, the technology to produce crystalline silicon is well advanced and largely spread thanks to an extended prior use by the electronic industry.

The price of this evolving technology has been dropping continuously since several years and more active ongoing development and research is expected to make this technology economically competitive. According to the world energy outlook 2015 report [2], a 40% decrease of photovoltaic energy cost is predicted to be reached in 2040 (Figure 1. 4); the cost of oil and gas may increase in parallel if no new major natural reserves are discovered.

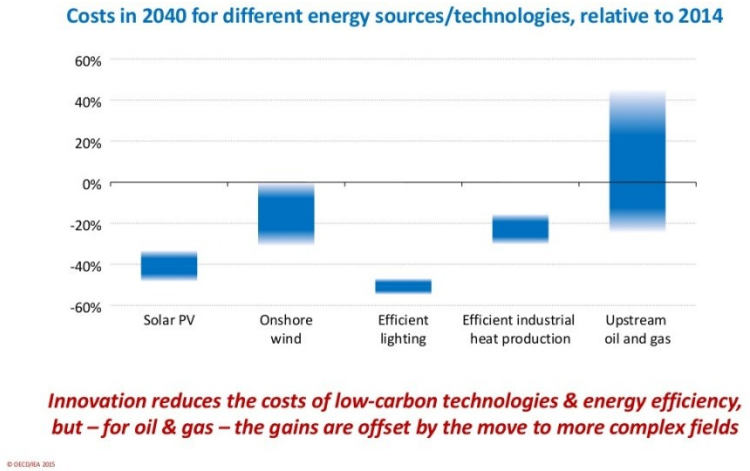

Figure 1. 4. prediction of price evolution for different energy sources[2]

The evolution Prediction of the PV modules cost presented in (Figure 1. 5) shows a continuous regular decrease for the upcoming decades.

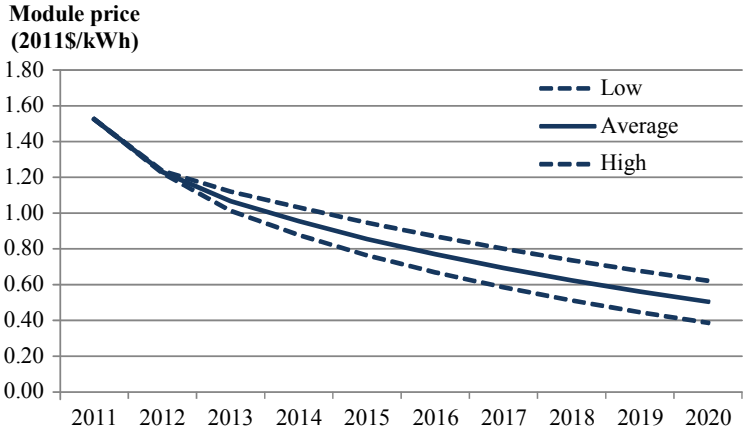

Fig. 7. Module price predictions until 2020.

Figure 1. 5. PV Module price prediction M.Glachant & all [5]

Such decrease is partly dependent on the ongoing development to reduce the production cost of silicon substrate and the spread of photovoltaic energy consumption around the world. If the price of the photovoltaic technology continues to drop as predicted, the energy market will reach a point where the price of photovoltaic energy becomes at full grid parity. A case of study for Germany, as a leader in photovoltaic energy, shows that photovoltaic electricity plants and grid installations in 2013 were already competitive compared to wind turbine, biogas and even natural gas turbines (Figure 1. 6.a). An estimated evolution of the kWh cost until 2030 predicts a continuous decrease of the photovoltaic energy cost towards full grid parity (Figure 1. 6.b).

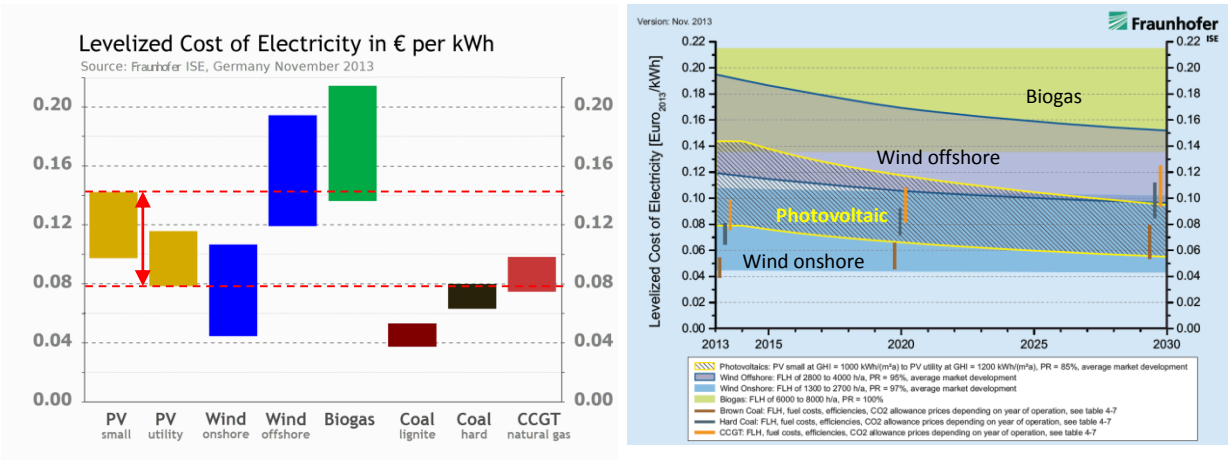

Figure 1. 6. a)-Cost of electric energy for different sources in Germany in 2013; b)-Prediction of the cost evolution for different electric energy sources until 2030 in Germany [6]

(Levelized cost of electricity in Euro per kWh (LCOE) forms the sum of all accumulated costs for building and operating a plant and comparing this figure to the sum of the annual power generation.)

An important share of solar cells production in the last decade was based on electronic grade silicon which turned out to be an Expensive unnecessary alternative. The consumption of Silicon, initially produced for other technologies, was not a viable solution for the Photovoltaic industry. One should consider that the desired qualities in electronic grade silicon are not necessarily the most beneficial for photovoltaic use. The important demand for good quality solar grade Silicon ingots motivated the industry to optimize new processes dedicated to silicon for photovoltaic application. In fact, most of the new Silicon manufacturing plants are actually dedicated to Photovoltaic applications [7]. For the last decades, Global silicon production capacity has been increasing year by year, from 32 500 tonnes in 2004 to 232 697 tonnes in 2010 at an annual cumulative growth rate of 38% (table 1).

Table 1. 1. Analysis of silicon production and demand from 2003 to 2010 (in tonnes) **[8]**

Year	Poly-Si capacity	Poly-Si demand (CI-semiconductor)	Poly-Si demand (PV)	Available PV poly-Si	Poly- Si stock
2003	26,700	17,000	9000	9700	700
2004	28,800	19,350	14,032	9450	-4582
2005	30,200	20,085	18,181	10,115	-8066
2006	34,500	21,166	16,705	13,334	-3371
2007	38,050	23,071	17,435	14,979	-2456
2008	48,550	26,301	24,089	22,249	-1840
2009	53,800	26,837	28,233	26,973	-1260
2010	58,800	27,632	32,108	31,168	-940

Lack (-) or excess (+) of polycrystalline silicon in the worldwide market.

Because of the present economic recession, the growth rate of photovoltaic production slowed down mainly due to economic considerations. Several silicon production factories using conventional crystal growth processes are struggling financially to keep up with the still existing lack of parity for PV energy. There is a need for process optimization and process innovation that can reproduce, robustly and continuously, the desired higher efficiencies of solar cells advertised by the actual development on an industrial scale and at lower cost. Any processes that can help make this technology cheaper and more efficient are simply a worthy investment which motivates the present work investigating the potential of Kyropoulos process to produce cost effective and high quality silicon ingots for photovoltaic application.

I.1.2. Technological context

The production of photovoltaic crystalline silicon cells is a multistep process. However, the cost is not divided equally between these steps. At the present time, growing and slicing large silicon ingot is the dominant industrial approach to manufacture silicon wafers for photovoltaic applications [ref]. 50% of the cell price is actually coming from the cost of the final wafer. Ingot production and sawing operation results usually in almost half of the raw silicon material going to waste from kerf loss. Such situation is a major drawback since it increases consequently the production price of the final wafer.

In order to overcome this challenge, several new crystal growth processes are being developed or optimized specifically for this need in order to reduce as much as possible material waist. Beside the required material quality, the development of these new or optimized processes is highly affected by the desired final ingot shape and dimensions. In order to be efficient and cost-effective, the optimization of these silicon production processes needs to comply with these main points, the ingot should have:

1. Good crystalline quality with low defects density
2. Optimum shape and size in order to reduce kerf loss
3. Low chemical contamination rates
4. Homogenous properties from top to bottom

In our days, there are two major solidification processes used for the production of PV Silicon ingots:

- Czochralski solidification process
- Directional solidification process

Some new promising processes are also currently into development:

- Cast seed method for silicon[9] [10][11]
- Non-contact method for silicon[12]

In the scope of the present investigation, we propose an innovated silicon ingot production process that has the potential to answer several of the required improvement in the photovoltaic industry:

- The Kyropoulos solidification process for silicon

The following part will describe each one of the prior listed processes by mean of their advantages and disadvantages in order to show the potential of the investigated process of Kyropoulos for silicon

I.1.2.1. Czochralski process:

The Czochralski process dominates the production of monocrystalline silicon worldwide. The basic principle is carried out by melting a charge of high purity silicon in a fused crucible. A powerful lateral resistor is used as the main heater (Figure 1. 7.a). Ones the melt is at the right temperature slightly above the melting point in the seeding central spot, a monocrystalline silicon seed is dipped into the melt. The seed is then slowly pulled upward and rotated simultaneously. The crucible can be rotated to homogenize and stabilize the melt flow.

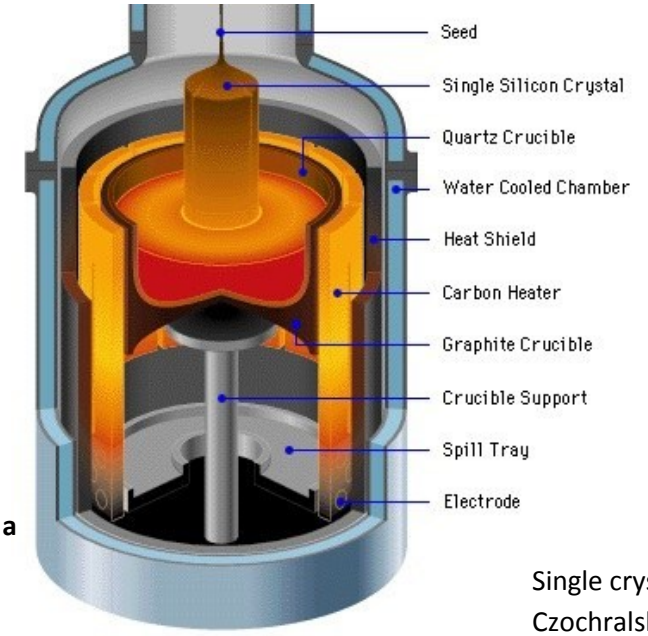


b

Single crystal of silicon produced with the Czochralski process. Deutsche museum

Figure 1. 7. Schematic view of Czochralski solidification process [7]

The starting of a conventional Czochralski solidification process happens in two phases. At the beginning, a conical growth from the seed is formed at low pull velocity to reach the final desired diameter of the ingot. This diameter is limited by the stability of the equilibrium between the melt and the crystal. Ones the final diameter is reached, the pulling velocity is adjusted to about 1mm/min to continue the crystal growth process. Slower pull velocity will increase the ingot diameter while higher pull velocities will decrease the ingot diameter. During the Czochralski process, the solid liquid interface is slightly above the free surface connected to the melt by a liquid silicon meniscus.

Czochralski process can produce high quality monocrystalline silicon ingots (Figure 1. 7.b) of 300 mm diameter and 2m length. The general standard size of a Czochralski silicon ingot is a cylinder of 200 mm diameter and 1 m length [11]. The ingot has only the seed as a holding point and

therefore it has no contact with the crucible which reduces mechanical stress and eliminates multiple germination sites. Since the seed have the tendency to be a source of dislocations, an additional necking step was added just after the dipping to create an elongated thinner neck that allows the release of progressing dislocation through the exterior walls of the neck before they reach the main growing crystal.

The Czochralski process is a very energetic process that requires relatively extended operating time. The process is mainly heated by a powerful side heater to melt the charge of the silicon and to control the radial growth of the crystal. Large part of the heat in the melt is extracted through the growing ingot. The maximum radial diameter of Czochralski ingots is limited by stability issues. The final ingots are extended in the axial direction giving high aspect ratio (length/diameter) cylinders. The cross section of a Czochralski ingot is circular. As a geometric fact, the cut losses to pass from a circle to a square section will be at least 30% to get the square shape wafer. Furthermore, a wafer is about 150 µm thick and the slicing wire has a diameter around 180 µm which means that 50% of the silicon will be lost in slicing operations. The cost lost associated to this is clearly way too high[13].

I.1.2.2. Directional Solidification Process for Silicon (DSS):

Great part of multicrystalline silicon ingots are produced by a DSS process (DS process for Silicon) (Figure 1. 8). The production process is carried out by melting a charge of high-quality polycrystalline silicon in a quartz crucible. Once the melt is suitably homogenized, the solidification process is realized by extracting the heat from the bottom. As a consequence, solidification starts from the bottom using the crucible inner base as a nucleation site. The controlled solidification process might be carried out by gradually removing the crucible from the hot zone downward while the heat is extracted from the base of the crucible; or, as an alternative, the crucible remains in a fixed position while the lateral heating resistances are moved upwards.

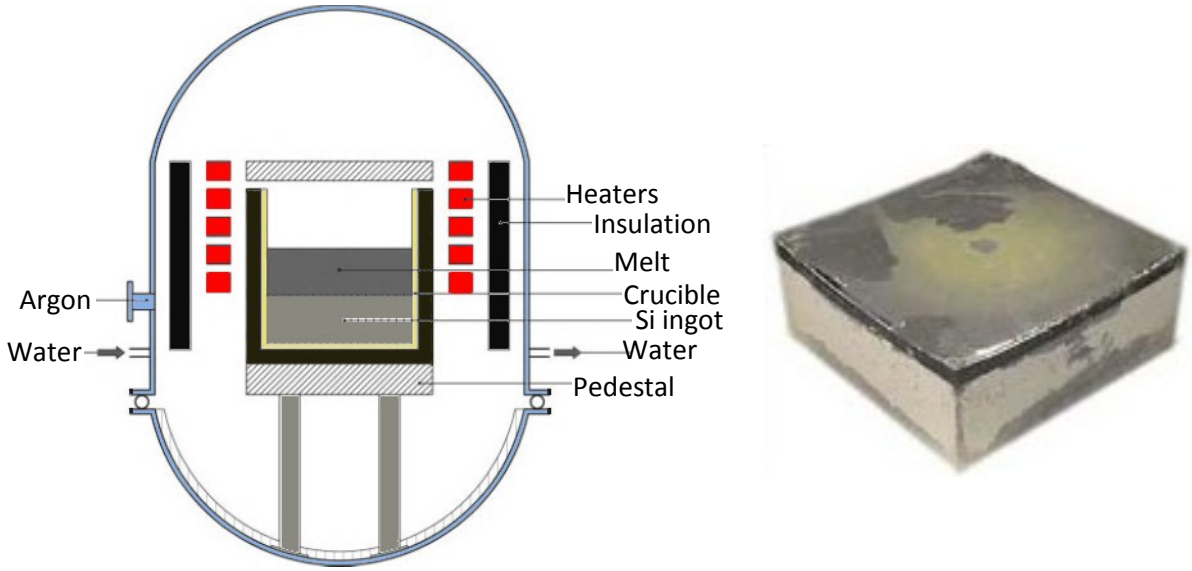

Figure 1. 8. Schematic view of directional solidification furnace ,on the right, a multi crystal Si ingot obtained by DSS process [14].

The ideal case of fully directional solidification should have purely axial heat flow to insure a stable horizontal solidification interface preventing undesired crystallization from the crucible side walls. However, the crystallization is not perfectly one directional in DSS commercial furnaces since it is technically difficult to prevent heat leaks from the crucible walls.

DSS processes have the advantage of producing large ingots of polycrystalline silicon up to 850 kilograms in each run cycle of 60 to 70 h. The obtained final ingot from DSS processes takes the shape of the square crucibles which limits, to some extent, the kerf loss during the cutting operation. The generic size of DSS ingot has roughly a horizontal section of 1000x1000 mm^2 and an axial depth of about 20-25 cm [15]. Compared to Czochralski ingots, DSS ingots have rather a flat form factor.

The DSS process provides a less costly alternative to CZ crystallization; however, the crystalline quality is lower. The DSS process produces multi-crystalline ingots rather than single-crystalline. The obtained ingots are usually subject to high contamination risk. The direct solid contact between the ingot and the crucible introduces impurities which further contribute to inferior device performance [12]. The ingots show a typical contamination zone all around the side edges. This impurity diffusion effect is visible in the lifetime map of the cross section of a multi-crystalline DSS ingot where the edge area have low charge carrier lifetime. Such observation underlines the importance of the problematic contact between the ingot and the crucible as well as the quality of the final residual melt solidified on the top of the ingot at the

end of the process. DSS ingots present high density of dislocations because of the mechanical stress resulting from solid contact between the ingots and the crucible.

The solar cell efficiency is a crucial criterion to promote the evolution of PV market. One of the major optimization points of energy conversion efficiency is the quality of the silicon wafer. The highest solar cell efficiencies are obtained by single crystal wafer with low defect density and low contamination rate. In addition, it is also highly desirable to obtain homogenous quality through the entire ingot which is more feasible for monocrystalline ingots than polycrystalline ones.

Newer Optimized versions of DSS processes can yield ingots with large, columnar grains that are parallel to the growth direction. Such ingots return high quality wafers since the vertical parallel grain boundaries don't obstruct the traveling path of minority carrier and therefore not deteriorating the cell efficiency. Furthermore, the presence of these well-engineered grain boundaries captures different harmful impurities from the grains area. High efficiency solar cells (> 17 %) were produced at the industrial scale using such wafers. Even higher efficiencies are expected to result from ongoing development of such wafers manufacturing [16].

I.1.2.3. Seed-Cast process for Silicon:

The seed cast process for silicon is an emerging case of process development. Basically, the seed cast process is a highly optimized DSS method by adding the seed feature coming from the Czochralski process. Several high quality mono-crystalline silicon seeds are laid on the bottom of the crucible (Figure 1. 9). The crucible is placed on a cooled platform to allow the directional heat extraction and to prevent the seeds from melting. The silicon melt is placed on the top of the seeds bedding. The solidification process is initiated by heat extraction from the bottom of the crucible. The crystal growth starts from the seeds while avoiding as much as possible crystallization from the walls of the crucible. In the ideal case, the crystal seeds orientation laid in the bottom are swept vertically all the way to the top during solidification. The seed casting method can yield ingots of consequent size. The ingots can be constituted of very large grains and the obtained wafers are qualified as mono-like wafers.

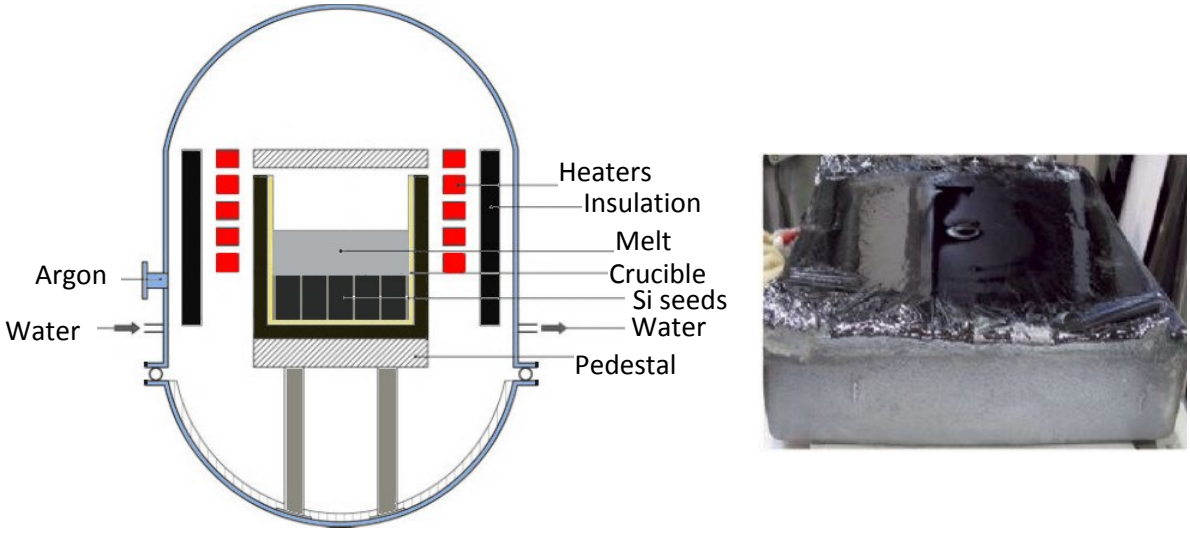

Figure 1. 9. Schematic view of seed-cast process furnace[7],on the right, a mono-like Si ingot obtained from a single seed [14].

The process includes some of the most favorable features in conventional silicon ingots production for PV: mono-like crystalline wafers, lower production cost, high productivity and full square-shape.

On the other side, this crystal growth process is still facing a number of mass scale problems that need to be resolved: it still has extended defects formation during the growth process, and the used seeds are expensive if their consumption is not optimized. Several studies reported that the junction between the seeds in the cast-seed method is source of high density of defects in the growing crystal [11].

I.1.2.4. Kyropoulos process:

In 1926 Spyro Kyropoulos proposed a process where the solidified crystal had no contact with the crucible to avoid mechanical stress cracking in his alkali halide crystals [ref]. The process was then optimized to become the most effective method to produce sapphire boules for optical applications in the current time [14].

The essence of this method is based on dipping a seed in the surface of a melted charge. The surface of the melt is usually slightly above the melting temperature. In recent Kyropoulos processes [17], the growth is sustained by a continuous cooling of the melt. The crystallization front progresses gradually inside the melt with no rotation. It is to be emphasized that, unlike Czochralski process, the crystal growth happens below the surface of the melt and not on top of it. During the growth process, the crystallization front takes a convex shape towards the growth direction.

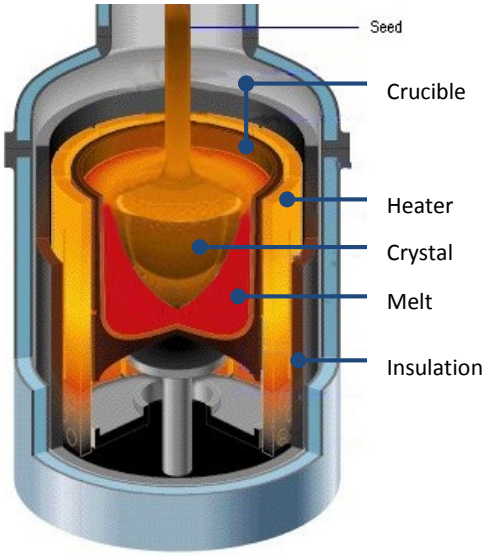

90 kg sapphire crystal grown by F.J.Bruni using Kyropoulos method [17]

Figure 1. 10. Schematic view of Kyropoulos solidification process. On the right, a sapphire crystal obtained by Kyropoulos method.

Kyropoulos furnaces are originally based on a powerful side heater (Figure 1. 10). New optimized generation of Kyropoulos furnaces has been developed with three, instead of one, independent resistive heating element, two side heaters (upper side and lower side heaters) and one bottom heater for more precise control of the temperature gradient at the different stages of the process [17]. The three heating configuration resulted in a shorter overall process time for the same crystal mass and higher yield of crack free and bubble free crystals. At the end of the Kyropoulos

process for Sapphire, the resulting ingot has an irregular shape and usually occupies almost the whole crucible with few residual melt left at the bottom. A comparison between the presented processes is summarized as follow:

Table 1. 2. Adaptation possibility of Kyropoulos Process for Silicon Production

KYROPOULOS PROCESS	CZ	DSS	DSS seed cast	Kyropoulos
Single crystal ingot	✓	✗	!	✓
Large ingots with flat form factor	✗	✓	✓	✓
Square shape ingot	✗	✓	✓	✗
No contact with the crucible	✓	✗	✗	✓
Seeding possibility	✓	✗	✓	✓
Control of initial defects density	✓	✗	✓	✓
Lower thermal gradient	✗	✓	✓	✓

According to the summary in table 2, Kyropoulos has several advantages to offer that worth more in depth investigation and few drawbacks; however, there is still one important point to address since, unlike the other listed processes, Kyropoulos is not an actual process for silicon. Current materials elaborated by Kyropoulos have major differences compared to silicon and a direct projection is not easy to make which bring us to the next important question:

I.1.3. Is Kyropoulos process adaptable for silicon?

On a technical point of view, Kyropoulos process is applicable and fully adaptable for bulk silicon production. However, the implementation of a new process in the industry is not a spontaneous task and therefore requires full justification of gain and improvement. Tab.3 shows a comparison between different crystal growth processes. The Kyropoulos operating parameters and yield are not for silicon, yet the values are a good approximation of the expected orders of magnitude. Compared to Czochralski, Kyropoulos process have a low growth rate; however, this low growth rate is compensated by the larger area of the solid liquid interface in Kyropoulos process which ends up by a high total mass growth.

Table 1. 3. Comparison of different operating parameter for the production of Silicon ingots between the major existing processes and the expected Kyropoulos process for silicon**[18]**

	Czochralski process	**Directional solidification**	**Expected Kyropoulos**
Growth rate (cm/h)	4.5–9.0	1.2–1.8	1 – 5
Diameter or size (cm)	15–30	69×69, 84×84	> 400
Crystal structure	Single	Multi or Single	Single
Feedstock requirement	High/moderate	Low	High/moderate
Solar cell efficiency	17–23	16–19	Comparable to CZ[19]
Comments	Mature	quality improvement	under development

Tab.4 summarizes the adaptation possibility of Kyropoulos for silicon:

Table 1. 4. Adaptation possibility of Kyropoulos Process for Silicon Production

Key points to improve	Conventional Kyropoulos	optimization for silicon
▪ Bigger ingots to raise the yield capacity	yes	yes
▪ Production of square shaped ingots	no	possible
▪ No contact with the crucible ▪ reduce chemical contamination	yes	yes
▪ Use of a seed	yes	yes
▪ Possibility for growth in low thermal gradient.	yes	yes
▪ Easy Dissociation of the final crystal	yes	yes
▪ Increase the solidification interface velocity	difficult	difficult
▪ Increase of volumetric solidification growth rate	yes	yes

Referring to table 2 and table 4, Kyropoulos process has several improvements, and only few drawbacks, that can be investigated for the production of silicon for photovoltaic applications. Such combination of advantages is not applicable to any other silicon production process.

I.2. Kyropoulos process outlook

The Kyropoulos technique is a crystal growth process designed to produce large size bulk crystals of high quality with low dislocation density. Such advantages are due to the low stress growth environment resulting from low temperature gradient resulting usually in low thermal gradient curvature and unconfined crystal growth. From a technical point of view, Kyropoulos process can be used for a wide range of materials. However, the process was designed originally as a well suited solution to grow large ingots of materials with low thermal conductivity and high thermal expansion coefficient. Such materials, usually brittle, are extremely hard to grow using other crystal growth processes[20].

In the same perspective, the advantages of the Kyropoulos technique can be highly beneficial for the production of high quality large silicon ingots for photovoltaic applications. Furthermore, compared to Czochralski, the technique has the potential to produce ingots with different shape, which could be cubic rather than cylindrical, and a more effective form aspect ratio, which could be flat rather than elongated. Ones may also expect a reduction of chemical contamination usually originated from the crucible wall and the high fraction of diffusion distance in crystals of limited size. In conjunction to the prior optimistic outcomes of Kyropoulos, the conventional crystal growth processes, CZ, DSS are failing to satisfy some of the modern needs for several materials. The DSS still has the drawback of limited crystal quality and the CZ still has the drawback of high form aspect ratio.

Regardless the several challenges in Kyropoulos technique, some materials that were hardly considered for this process at its early ages seem now good candidates, including crystalline silicon for photovoltaic application.

I.2.1. Kyropoulos process evolution:

Kyropoulos crystal growth method was a process created out of necessity to produce challenging materials requiring specific growth environment. The Kyropoulos technique was first proposed by *Spyro Kyropoulos* to grow large alkali halides crystals [21]. Such brittle materials were extremely hard to grow using other crystal growth processes even in small sizes. This is due to the fact that alkali halides materials have exceedingly poor resilience which can easily deteriorate the material under mechanical and thermal stresses. Such crystals tend to loose consequent part of their optical quality or even fracture during removal from the crucible or

during cooling. In his approach, illustrated in (Figure 1. 11), Kyropoulos proposed to grow the crystal in an unconfined environment to limit frictional induced stress during the growing and the final removing of the crystal. The crystal was obtained by dipping a shaft into a melted charge to grow bulk crystals inside the melt. The shaft was a double wall tube cooled with air flow. The cooling of the shaft was reported to be controlled by the air flow rate intensity flowing through the shaft.

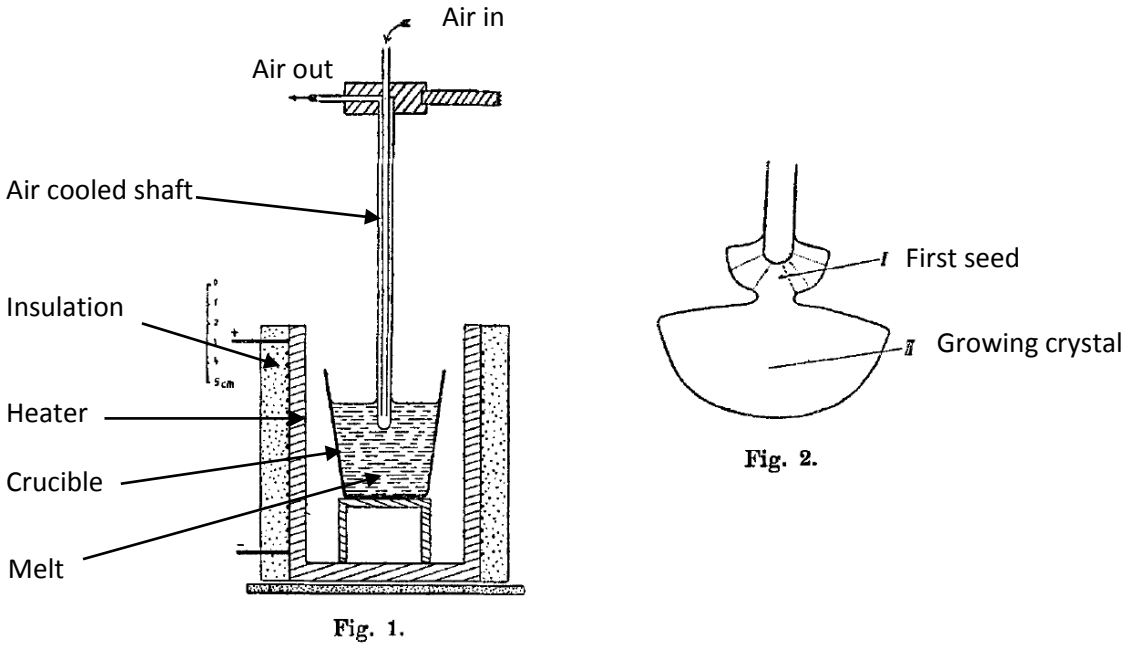

Figure 1. 11. Growth process as proposed by Spyro Kyropoulos

The dipping operation was performed in two steps. A small crystal is formed on the shaft in a first dip. The obtained crystal was pulled out and dipped again as a seed. A probability to obtain single crystals was reported to be higher by limiting as much as possible the contact zone between the melt and the crystal in the hope to grow from a zone with a single orientation and therefore obtain a single crystal.

Although successful growing of alkali halide crystals was reported in Kyropoulos publication [21], little information was provided on the size and the shape of the crystals. The crystal was lifted up outside the melt before it touches the crucible wall. It was reported that better crystal quality was obtained at slower cooling and careful control of air flow rate. A top cover was used to reduce radiation exchange; no further information was given about the motivation for the radiation shield.

The shape of the crystal in this configuration for a steady state condition can be predicted by a profile of the temperature field given as Laplace equation (eq.1). If the seed is supposed at constant temperature which is describing the boundary condition in eq.2 and that the cooling is dominated by the heat extraction from the seed which is describing the boundary condition in eq.3, the growth can be described as an axisymmetric case and the solidification interface is an ellipsoid of rotation. Assuming that the melt is at homogenized temperature, the shape of the crystal will be clause to the solution of heat diffusion in the crystal at stationary state. The equation can be given in the form:

$$\frac{1}{r}\frac{\partial T}{\partial r} + \frac{\partial^2 T}{\partial r^2} = -\frac{\partial^2 T}{\partial z^2} \quad (1)$$

The relative boundary conditions can be written under the assumption that the seed is maintained at constant temperature and all the heat is extracted from the seed. Supposing that the origin "O" is at the center of the contact between the seed and the melt, we may write:

$$T = T_0 \quad \text{when} \quad Z = 0 \ \text{and} \ \ 0 < r < R \quad (2)$$

$$\frac{\partial T}{\partial r} = 0 \quad \text{when} \quad Z = 0 \ \text{and} \ \ r > R \quad (3)$$

$$T = T_m \quad \text{at solid\_liquid interface} \quad (4)$$

where R is the seed radius and T_m is the melting temperature

Similar development with comparable experimental data for the case KCl crystals was presented by E.Schönherr [22]. The obtained solution of the crystal interface is an ellipsoids with focal points (r,z) = (R , 0) and (-R , 0), where R is the radius of the seed. The thickness of the obtained crystal was 4/5 the radius of the crystal. The obtained crystals radius was less than 15 mm (Figure 1. 12).

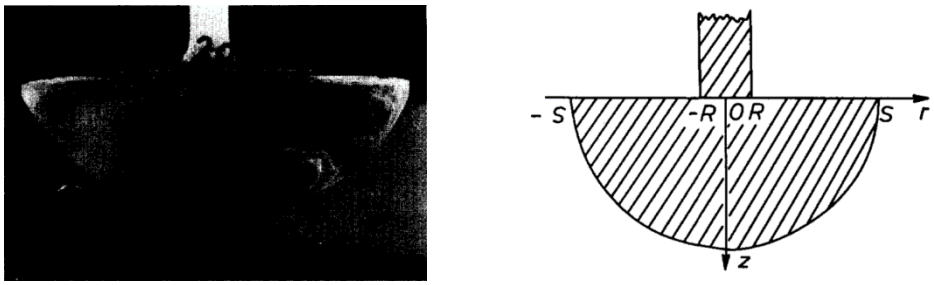

Figure 1. 12. KCl crystal grown by Kyropoulos process, on the right, shematic representation of the crystal

Later publication by Korth [23] presented a modified Kyropoulos technique related to Dr. Hilsch and Dr. Bauer. The process included more consequent cooling parts targeting the top of the seeding zone (Figure 1. 13). The growth was established from a seed fixed on a water cooled shaft. An additional cold spiral tube was placed above the surface of the melt to improve axial heat extraction.

The added cold source on the top of the melt surface aimed to improve the vertical thermal gradient to promote the growth of the crystal in the vertical direction. One major challenge in this technique was the fact that radial growth was faster than vertical growth. The reported obtained crystal was flat bun shape with 8 cm in diameter and 2 cm thick. Obviously, it was hard to promote the vertical growth even with new added cold sources. The emerged state of the crystal and the lack of knowledge of temperature distribution and convection in the melt were limiting the improvement of the process. Using the only available certainty about the availability of a cold zone on the top of the melt, a slow upward pull was deployed as a solution to grow more mass in the vertical direction.

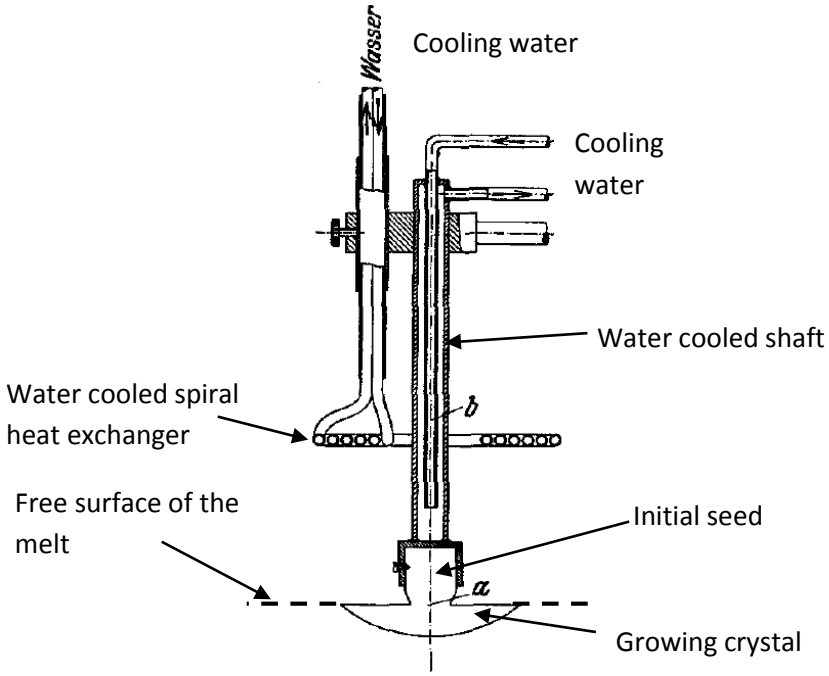

Figure 1. 13. Modified Kyropoulos process with a cold source on the top proposed by Korth [23]

MENZIES AND J. SKINNER reported several observations about the Kyropoulos technique in their publication [24]. They explained that the crystal growth in Kyropoulos technique could be sustained by the cooling of the seed itself, which they qualified as old school approach, or by

lowering the furnace temperature. The latest approach was favored. The chuck was kept at constant cooling by water while the growth of the crystal was sustained by global decrease of the melt temperature. An attentive guess from the reader may perhaps support the same approach since lowering the furnace temperature lowers the thermal gradient in the growing crystal which is generally a good practice for higher crystal quality.

The rate of growth was controlled either by adjusting the cooling temperature of the chuck or by accelerating the decrease of the furnace temperature. Continuous decrease of the furnace temperature would eventually bring the melt close to the freezing temperature and the temperature gradient across the surface of the growing crystal will become very small. At these conditions, spontaneous crystallization was reported as possible where the growth rate can no longer be controlled. The publication noted that the outward radial growth was faster than the downward axial growth in this technique and therefore extra engineering of the cooling method was required. The vertical growth was also reported to be carried out using an alternation of growth inside the melt followed by a certain pull. Although clearly mentioned that the growth was inside the melt, few details were known about the fraction of the crystal immersed below the melt free surface. Furthermore, no pull was required for crystals with diameter clause to the crucible diameter since the level of the melt will decrease naturally, and fast enough, due to the volumetric contraction of the growing solid crystal. This fact will have reversed effect for material with higher density in solid state such as silicon and requires further investigation to predict the displacement of the free surface of the melt.

The Kyropoulos process was reported as sensitive to asymmetries in the furnace that may cause asymmetric crystal growth; rotation of the crystal was proposed as a possible fix.

Further development provided by Katherine Chamberlain [25], working on potassium bromide crystals, introduced the idea of non-uniform side heating to promote a more consequent enlargement of the crystal inside the melt. In fact, potassium bromide has very low thermal conductivity decreasing considerably heat extraction from the seed even with water cooling. To overcome this, the side heating was separated into a lower and an upper part. As a consequence, a slow reduction of heating power in the upper side heater provided much larger growth of the crystal. The lack of further information on convection at this phase of development was a major limiting factor for the development of the process. It is without doubt that the challenges in such study are beyond the scope of heat conduction alone. The profile obtained from simple conduction resulting from a uniform lateral heating should have allowed high radial enlargement. Furthermore, Interesting experimental observation made in the same publication denotes that undesired parallel crystal growth from the boundaries may occur whenever the main crystal starts to grow too fast. In other word, at very fast cooling where the transient nature

dominates, the growth process prediction, especially nucleation sites, is very difficult. All the prior works are lacking information about the transient progression of solidification which limited the development of working parameters around equilibrium states.

The attempts and evolutions to improve Kyropoulos process stayed limited by the listed challenging difficulties that remained unsolved and misunderstood. The immersed state of the growing crystal inside the melt in Kyropoulos process complicated the understanding of the growth progression. There was no proper control of the central cold zone enlargement into the deep melt and no control of the solidification interface shape. Both points are closely related to the heat transfer by convection in the melt which is very hard to monitor and to study experimentally for crystal growth processes at high temperature. As a consequence, the Process stayed limited to a restricted number of extremely brittle materials while a wide range of new developed materials, mostly less brittle, found main interest in the rising Czochralski technique. Such concerns were summarized by David F.Bliss [20] into several necessary points to reach maturity of Kyropoulos process. The publication puts forward the following crucial points: understanding convection and radiation, using computer aided design to understand thermal environment, thermal stresses and interface shape, relating the process parameters to the control of the crystal diameter and shape, modeling of fluid dynamics as well as heat transport and scaling the system for large crystal production.

I.2.2. Crystal quality and defects control using growth condition

Despite these difficulties, the interest in Kyropoulos technique subsisted for some specific needs. In our days, Kyropoulos is known to excel at producing high quality large bulk sapphire crystals of extremely low dislocation density [20]. Published experimental data [26] show a significant improvement of defect density reduction obtained by Kyropoulos process compared to CZ and HEM (Heat Exchange Method) processes for sapphire. A low defect density of 100 pits/cm^2 was reported in this work for grown Kyropoulos sapphire crystals. This value was reported as one order of magnitude better than industry standards for epitaxial wafers which has 1000 pits/cm^2.

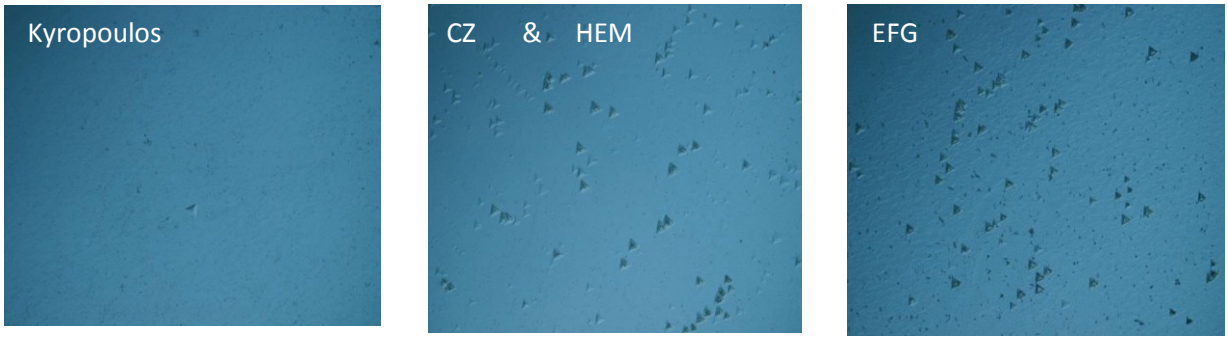

Figure 1. 14. Defect density of different sapphire materials obtained by different processes [26].

Presented pictures in the paper (Figure 1. 14) of etch pit characterization for dislocations show more than 50 times less dislocation density, in sapphire crystals obtained by Kyropoulos compared to other methods; no further information was provided for the area were the sample are taken from and the size scale was not specified as well. The reported sapphire ingots were as large as 200 kg demonstrating lower defect and lower stains. Further work denoted the importance of the low gradient inside the melt as a leading cause to grow large crystals with unusual low residual stress. High quality Sapphire crystals of 500 mm in diameter were obtained using a Kyropoulos configuration that reduces substantially the power consumption required per unit mass of grown crystal. according to the same publication, the described Kyropoulos process overcomes the other processes in quality, size and manufacturing cost per weight [26] .

Defect density in crystal growth processes may have several reasons[28]. An unconfined crystal growth can still be subject to high defect density generation due to thermal stress. The latest is commonly related to the thermal gradient in the ingot during solidification; however, the accurate cause is in fact the increase of the second derivative of spatial temperature variation[27].

Higher crystal quality is then dependent on the decrease of the curvature of thermal gradient in the crystal during cooling.

Generation of dislocation requires extremely high stress usually not encountered in bulk crystal solidification with low thermal stresses. Most of dislocation appearance in such cases is related to dislocation movement and multiplication. The choice of a good quality seed with very low defect density and the use of necking technics are two efficient approaches to lower defect density.

I.2.3. Kyropoulos process for silicon

The use of Kyropoulos technique for Silicon production is quite limited to nonexistent. In the literature, only one paper of Ravishankar[19] (Ravishankar, 1985) presented an experimental study to grow Silicon ingot using Kyropoulos technique for photovoltaic applications. Ravishankar investigated the potential of the method to grow large ingot with a flat aspect ratio (height/diameter) while the conventional CZ process was extremely hard to be cost effective directly by scale-up due to the large aspect ratio (height/diameter). A silicon seed was dipped into a slightly super-cooled silicon melt using cylindrical crucible. The growth was initiated as a Czochralski process where the seed is pulled up to make a crown. Unlike Czochralski process, the crystal was allowed to continue growing inside the melt limited only by the walls of the crucible. The crystal grew radially and axially at the same time. Pull up velocity between 10 mm/h and 15mm/h was used in parallel with a continuous decrease of the heater temperature to sustain the solidification. The grown ingot contacted the crucible and the pulling was stopped as part of the process. The ingot was then allowed to complete the growing toward the bottom of the crucible. Two approaches were used to detach the ingot from the crucible. A first presented ingot was detached using silicon nitride coating as releasing agent deposited on the internal walls of the crucible. The substance ended up peeling into the melt and acting as nucleation points. As a consequence, the final crystal had several large grains rather than being a single crystal ingot. A second fully monocrystalline ingot was obtained without releasing agent. The ingot was remelted partially at the end to detach from the crucible and pulled out from the residual melt. In order to detach the ingot, the heater was raised to full power in the hope to remelt a thin film of silicon between the ingot and the wall to detach the ingot. As a consequence, a substantial amount of the ingot melted before it could be taken out. Cylindrical silicon ingot of 8.6 kg with 15 cm diameter was produced. The obtained single crystal had relatively low dislocation density (less than 10^{-4}). Solar cells made from the single crystal ingot had comparable efficiency (up to 13.4%) with solar cells made from Czochralski ingots. The obtained ingot was free of carbon which puts under interest the effect of this technique on the carbon contamination processes. Because of the fact that radial growth was faster than axial growth inside the melt, which is true for most of the prior listed Kyropoulos investigations, Ravishankar suggested that the melt should have a small aspect ratio depth/width in order to reach enough axial growth before the crystal reaches the side walls of the crucible. Such design will imply a configuration with a shallow met in a wide crucible with deep impact on the melt flow regime.

Recent works published by Nakajima et al [12]presented results of a comparable technique to grow silicon ingots from a dipped seed without any contact with the crucible. The method was referred to as a Noncontact Crucible Method. A low temperature zone was reported inside the melt where the crystal can grow naturally from a seed with a gradual pulling rate of 0.2 to 0.3 mm/min. The melt had a low depth/width aspect ratio. A solidification front captured

by rapid extraction of the growing ingot showed that the crystal had a flat bun shape with a maximum immersed length of 2.7 cm in a melt of 3 cm depth. Large single crystals measuring up to 26 cm were obtained in a 33 cm diameter crucible using a melt with a depth of about 4 cm. The single crystal had a low dislocation density of $1.9x10^3$ per cm^2 in practically all the ingot except on its borders where it increased locally to $6.8x10^3$ per cm^2 [29]. High lateral growth yield was achieved and crystals with diameters of 80-90% of the crucible diameter were reported [30]. A contamination zone with low minority carrier lifetime was observed at the borders of the ingot, with a width almost independent of the crystal size. This puts interest in large ingots to make the contamination region fraction very small compared to the whole ingot. The technique was able to stabilize facet growth, producing ingots with a horizontal section as a perfect square shape delineated by the silicon <111> facets using a seed with the orientation <100> in the growth direction. A later publication [29] suggested that convection is believed to be suppressed by the large low temperature region. No further details were given concerning the flow regime below the crystal. a recent publication for the non-contact crucible method [31] introduced an update of the heating configuration with two heater zones. The first heater is a lateral heater around the crucible and the second heater is a horizontal plate placed below the crucible. The growth was reported to take place by a decrease of the first heater then sustained by a decrease of the second heater. The maximum diameter of the crystal was reported to be mainly dependent on the temperature reduction of the first lateral heater and not strongly affected by the temperature of the second bottom heater. Large aspect ratio ingot/crucible was achieved and ingot of diameter 45 cm was obtained in a crucible of diameter 50 cm. The publication reported that the diameter aspect ratio crystal/crucible was not much affected by the size of the crucible but mainly by the temperature decrease. According to these results, larger diameter crucible can then be used to obtain larger ingots. The reported oxygen contamination was quite low $1x10^{18}$ cm^{-3}. The oxygen concentration did not depend strongly on the diameter aspect ratio crystal/crucible.

At the exception of the Kyropoulos case for sapphire, the prior listed development works did not investigate the effect of convection on the solid liquid interface. It is noticeable that each configuration is different and a general statement concerning convection effect is not easy to make; therefore, it is crucial to understand the key points relating fluid dynamics to the solidification process.

I.2.4. Melt flow characteristics and numerical simulation

Crystal growth from a melt at high temperature is mostly controlled by heat transfer. The kinetic undercooling of the growth interface and the variation of the freezing point resulting from solutes are, in general, rather small in comparison to the effect of global thermal transport [32]. It is common to approach melt growth, especially for high purity substances, as a heat transfer

problem including conduction, radiation and convection, next to the phase change. These phenomena are the outcome of a combination between the physical properties of the material and the operating parameters of the process.

While thermal conductivity is mostly related to the material, convection heat transfer is, in great part, the outcome of operating parameters. The melt convection effect have been extensively investigated, experimentally and numerically, for some crystal growth processes that are widely spread, especially DSS and Czochralski, however, most of the rest of crystal growth processes are mostly conducted by experience and little is known about the convection role during the growth. This investigation will find interest in the study of DSS process providing insight into the general silicon melt behavior and the effect of the square horizontal section of the crucible on the silicon melt. Similarly, Czochralski process for silicon provide insight on the thermal configuration in Kyropoulos since it is also a top seeding process. Results of Kyropoulos for sapphire will also be discussed briefly since it is one of the rare top seeding processes that stabilize the solidification interface fully below the free surface of the melt without contacting the crucible.

A large number of metal and semiconductor melts, such as Silicon, have a low Prandtl number, where the thermal gradient is not confined to a boundary layer. Because of this fact, it was reported that the heat transport rate is not dramatically increased by natural of forced convection[32]; however, it is also mentioned that such convective flow at low Prandtl number is very readily to become time dependent where resulting temperature oscillations may affect the microscopic growth rate. The melt convection effect on the heat transport during directional solidification for solar silicon was often neglected [33], [34]. No clear explanation was provided for this approximation, but presented experimental values of temperature were, usually, in good agreement with the calculated ones. A reference case study [35] outlined the importance of Gr and Ra numbers on the behavior of low Prandtl number fluids. According to the same publication, the melt flow strength and the morphology of convective cells are important criteria that affected the solidification interface shape. Such result implies how convection contribution was not flattened by the high thermal conduction of the melt under certain operating conditions.

DSS processes for PV silicon use square section crucible. The melt is cooled from the bottom to initiate the growth from the base of the crucible which is the reverse of CZ and Kyropoulos configurations. Because of the non-axisymmetric nature of the square shape, such numerical problem has to be three dimensional. The processes can be highly sensitive to the placement of the crucible and the alignment of the heating elements. even a small tilt of 3° of the whole furnace implies modifications of the melt flow pattern [36]. The case presented in this publication had an average vertical thermal gradient about 10k/cm in the crystal and 2-3k/cm in

the melt. It is noted also that the tilt of the solid liquid interface, rather than the whole crucible, disturbed the flow pattern in a similar way which shows that the melt flow can be highly sensitive to its interaction with the melt cavity shape and size. Published results for DSS solidification process in a square section crucible[37] for silicon reported an important effect of convection on solidification interface shape in industrial scale DSS furnaces for silicon. The thermal gradient in the melt was 1-3 k/cm, the given growth rate was 10 mm/h. In this work, several simulations show the influence of the square shape crucible on the melt flow pattern. It is also noticeable that this effect becomes stronger when the flow is stronger. The four corners of the crucible oriented the melt flow toward a four symmetry profile; the later seems to loose symmetry at slower melt flow. Similar point should be addressed with caution for our case where we are more likely to obtain a four symmetry flow. We suspect that this type of flow will be highly probable in the Kyropoulos configuration because of the reinforced central cold spot in the dipping zone.

The Marangoni effect in DSS process was found to be localized on the surface of the melt. The influence on the deep melt, or on the solidification interface, was reported as negligible except at the final stage of the solidification were the solid liquid interface is too clause to the surface of the melt[38].

The Czochralski process is quite similar to Kyropoulos process especially during the first dipping step; however two major differences are to be considered: the Czochralski has a cylindrical crucible and the melt as well as the crystal are under high thermal gradient. The typical value of thermal gradient in a Czochralski configuration is about 15-20 k/cm in the melt and about 30-50 k/cm in the crystal near to the solidification interface[39]. Using experimental measurement, it was confirmed that thermal gradient in the CZ crystal increases when the growth rate increases whereas thermal gradient in the melt only increases slightly.

The silicon flow in the Czochralski process is very complex. The melt rises at the heated crucible walls, due to buoyant forces then turns inwards radially toward at the melt surface to flow down again toward the base of the crucible to make a full loop. In addition, the crucible rotation is also added to stabilize the melt reducing the buoyancy driven flow. The heat loss from the surface of the melt are reported to produce a destabilizing vertical temperature gradient in the upper region of the melt that can give rise to Bernard-like convection [32]. For a certain value of the Rayleigh number, in natural convection, the melt motion is reported to become time periodic. This transition occurs most readily for low Prandtl number fluid such as silicon. Further increase of the Rayleigh number will give a time dependent flow and then a fully turbulent. This behavior is geometry sensitive. For our case, such effect should be treated with caution since the crystal grows inside the melt altering consequently the melt cavity shape. The publication proposes several solutions to delay the appearance of time dependence; either by making the

system more isothermal or by reducing the effect of gravitational field. As an example, magnetic damping of silicon melt has been found extremely effective in reducing temperature fluctuations.

In large scale Czochralski industrial furnaces, the flow is mainly turbulent [40],[41] and highly dependent on the internal shape of the crucible. It was reported as well that such condition is closely related to the form aspect ratio of the melt. Deeper melt have more potential to become unstable.

An experimental investigation on flow instability in Czochralski for silicon presented by Kakimoto [42] introduced the effect of melt depth on the flow. It was reported that, for a deep melt of silicon the flow instability takes place regardless crucible and crystal rotation. The result also suggested that natural convection overcomes the flow generated by crucible and crystal rotation. An added observation outlined that this limited effect may be attributed to the small size of the crystal. For the deep melt and crystal rotation of 10 rpm, the flow was time dependent and non-axisymmetric. The amplitude of temperature fluctuation was 10° with and without crucible rotation. For the shallow melt, the flow was time independent and axisymmetric where the temperature fluctuation was about 2° with no rotation, 3° at 3 rpm crucible rotation. A later case of shallow melt with crystal rotation at 30rpm was time dependent and non-axisymmetric where the temperature fluctuation was about 50° [42]. The publication stated that the thermal instability can be a direct consequence of the flow instability.

Very few information are available about the melt flow behavior and the solidification interface movement during Kyropoulos process. To our knowledge, we did not find any simulation work investigating heat transfer and fluid dynamics in a Kyropoulos process for silicon. In the literature, only few numerical studies investigated Kyropoulos process mostly for sapphire. Unlike Czochralski process, the interface shape in Kyropoulos process changes continuously during the whole growth process, which reduces the industrial productivity of the process.

Sapphire melt has several major differences altering consequently the flow nature, compared to silicon melt. The flow in Kyropoulos for sapphire is mainly a combination of buoyant and Marangoni flows. Most of the presented simulation investigations in the literature consider the flow as laminar. This is mainly due to the high viscosity of the melt and the low thermal gradient giving a Grashoff number equal to 1.4×10^5 and a Marangoni number in the range 4×10^3 [43],[44].

In Kyropoulos growth for sapphire, both the area of the free surface and the melt height decrease consequently during the full process therefore the flow pattern in the melt varies as well, however, the melt flow is suspected to be laminar due to the high viscosity of Sapphire melt. The Marangoni convection in Kyropoulos process for sapphire was reported without major effect

on the flow or the crystal during the early growth stage; however, the effect on the crystal becomes important in the late growth stage[45]. Few other publication presented a simulation of Kyropoulos for sapphire were the melt was considered as turbulent, it is not clear if the final numerical results confirms this assumption [46], [47].

Table 1. 5. Comparison of silicon and sapphire properties [46]**,** [48] **,**[49]**.**

Parameter	**Unit**	**Si**	**Al_2O_3**
Melting temperature, T_0	°C	*1412*	*2054*
Solid density, ρ_s	kg / m^3	*2332*	*3970*
Liquid density, ρ_l	kg / m^3	*2533*	*3030*
Dynamic viscosity, η	kg / (m s)	*0.00086*	*0.057*
Heat conductivity of solid	W / (m K)	*22*	*05*
Heat conductivity of liquid	W / (m K)	*66*	*2.05*
Volumetric expansion rate	1/K	*$1.4x10^{-4}$*	*$5 x 10^{-6}$*
Emissivity of solid, ε_S	-	*0.7*	*0.87*
Emissivity of liquid, ε_L	-	*0.2 - 0.3*	*0.33*

The fact that Sapphire is transparent to radiation increases consequently the heat extraction next to the solidification interface. It was reported that internal radiation enhances temperature distribution by increasing heat transfer between the different surfaces, which weakens both natural and Marangoni convections in the melt, and reduces stress level in the crystal[43].

The melt flow in Kyropoulos process has a central top cold zone in the upper part of the melt to initiate the seeding process. The resulting temperature profile should be decreasing, vertically from bottom to top and horizontally from side to center. The melt becomes highly instable and a natural convection may rise due to buoyancy forces. According to the prior, the flow in a Kyropoulos configuration for silicon will alter consequently the temperature distribution in the melt and therefore the growth of the solidification interface inside the melt. The strength and stability of the convective flow is dependent on the melt properties on one side and on the thermal gradients in the melt on the other side.

Prior numerical work on both Czochralski for silicon and Kyropoulos for sapphire are hardly projectable on Kyropoulos for silicon. The Kyropoulos process is fundamentally different from the Czochralski process since the solid/liquid interface is below the melt surface, and silicon material has major key differences compared to sapphire material as shown in Table 1. 5.

Nevertheless, these prior numerical modeling investigations have a number of similarities useful to the present work.

I.3. Conclusion of chapter one

Photovoltaic energy is one of the most promising renewable energy sources predicted to cover a consequent part of our energy needs. This upcoming demand for photovoltaic silicon ingots expects higher quality and lower cost.

By principle, Kyropoulos process is fully applicable to silicon material. Compared to existing production processes of silicon for photovoltaic application, the Kyropoulos process, investigated in this work, has the potential to produce high quality monocrystalline large silicon ingots with a flat aspect ratio suitable for photovoltaic applications. Combined with the large size of the ingot, the expected growth rate (1-5 mm/h) will allow high mass production rate.

Theoretically, the growth of the ingot in Kyropoulos process is only limited by the borders of the crucible which offers the possibility to affect the shape of the final ingot using the shape of the crucible. It is interesting to investigate the effect of a square crucible on the shape of the final ingot to make it squarer in order to diminish the kerf losses during the making of wafers.

The process have not been fully investigated; only one work of Ravishankar reported a high efficiency cells produced using monocrystalline silicon wafer from Kyropoulos process, the obtained wafer were reported to have low carbon contamination rate.

The process is complex and extremely difficult to be monitored experimentally, therefore numerical modeling is required to study the ongoing physical phenomena especially the effect of radiation and melt convection on the solidification process.

The advantages of Kyropoulos process for crystal growth are highly beneficial for the production of high quality silicon wafers which motivates the investigation of the process for such application. In order to bring the process to full maturity, the feasibility of the process needs to be proven and developed. Numerical and experimental investigation are then required to investigate the process.

Chapter 2

II. Numerical model construction and experimental setup description

This chapter describes the numerical model and the experimental setup used in the current work.

The chapter explains the creation of the simulation domain as well as the boundary conditions. The included physical phenomena in the numerical model will be discussed. Justifications are given about the simplification of the furnace geometry.

A calibration of the model is presented using thermal experimental data. Comparisons between numerical and experimental results are discussed to validate the numerical model.

A first set of numerical results is then presented to show the coupling between the three heating element and the temperature distribution in the furnace.

The chapter presents as well the evolution of the experimental setup during the thesis, on a construction point of view.

The main challenge in any numerical investigation of an experimental crystal growth process is to reproduce accurately the solidification process at reasonable calculation cost. For the present work, the model is supposed to predict the growth of a rotating crystal inside a silicon melt taking into consideration fluid dynamics in the melt which is strongly coupled with heat transfer by conduction, convection and radiation.

The accuracy of such complex process modeling requires full understanding of the real experimental setup in order to reproduce an optimal numerical geometry. In addition, such investigation should also identify the pertinent physical variables used to compare numerical results and acquired experimental data. The corresponding numerical values that should represent the measured experimental temperatures by thermocouples requires full understanding of the furnace environment and the evolved heat transfer modes.

II.1. Experimental Setup

II.1.1. Description of the experimental furnace

II.1.1.1. General design of the furnace in the original state as a directional solidification machine

The experimental furnace used for the present work was a CyberStar furnace originally designed as a directional solidification setup DS (Figure 1). The later was modified to operate as a Kyropoulos machine.

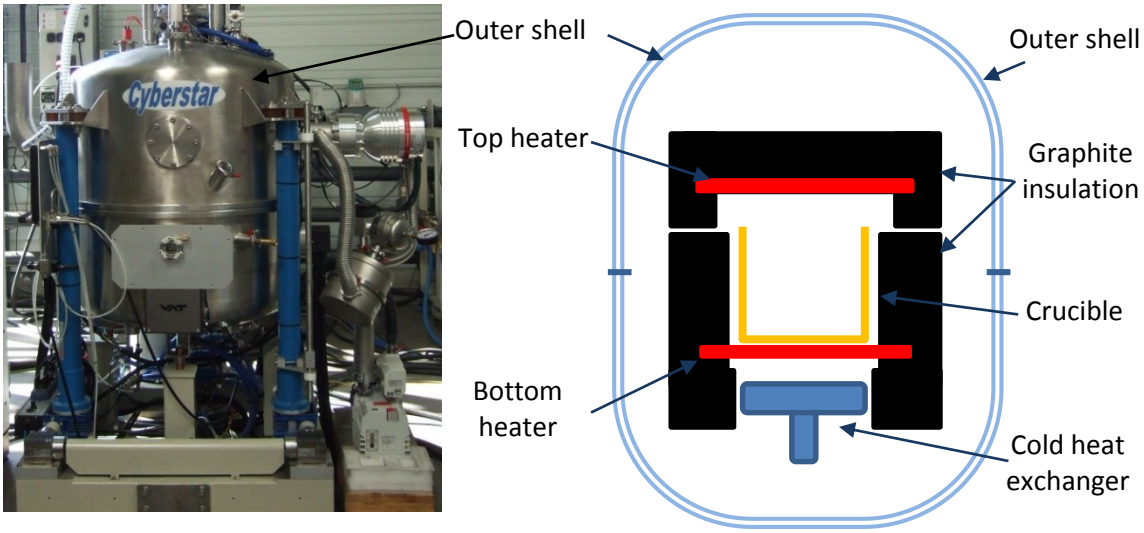

Figure 2.1. Real and schematic view of the furnace at starting configuration

The schematic representation of the furnace in Figure 2.1 shows the furnace in its starting configuration was mainly heated by a bottom and a top heater. The exterior steel shell of the furnace was a cylindrical container with a diameter of 800 mm and a height of about 1000 mm. The steel shell was composed by a top and lower parts coming in contact at roughly middle height. The mobile top part translates vertically allowing the opening and the closing of the furnace.

The core of the furnace was designed for G2 size crucible with a square horizontal cross section about 36x36 cm. The crucible and the heaters, were surrounded by a rigid graphite foam insulation. The silicon charge was heated by conduction from the bottom of the crucible and by radiation from the top. The power distribution in the top and bottom heaters was

adjusted to create the required vertical thermal gradient. A heat exchanger cooled with water was placed bellow the lower heater to improve heat extraction from the bottom of the crucible in the DS configuration.

II.1.1.2. Transformation of the furnace into a Kyropoulos machine

Kyropoulos technique is a top seeding process where the top central part of the melt is the cold zone during the full process. Such configuration is the reverse of the conventional directional solidification process in the vertical direction. Figure 2.2 shows the expected evolution of the vertical thermal gradient between DS and Kyropoulos processes.

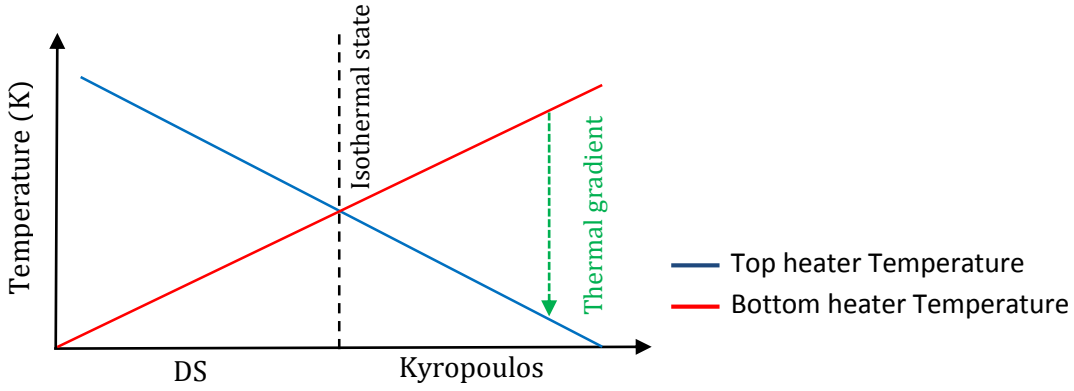

Figure 2.2. Evolution of the vertical thermal gradient from Directional solidification to Kyropoulos configuration

Intuitively, the reverse of the power balance in the top and bottom heaters of a DS machine should reverse the vertical thermal gradient making the top as the cold zone. The effect of this change of power balance in the top and bottom heaters do not necessarily give the required horizontal thermal gradient. Additional modifications of the furnace were needed to obtain a horizontal thermal gradient that increases from the center to the edges. The latest requirements led to three main modifications:

a) The establishment of the top central cold zone requires the redesign of the heating elements and their surroundings to focus the heating power more on the edges of the silicon charge in order to create a central cold zone on the free surface of the melt.

b) The unconfined crystal growth requires precise control of vertical and horizontal thermal gradients by redesign of the insulation as well as the cold sources to control heat fluxes extraction from the different sides of the silicon charge.

c) The furnace requires a top seeding mechanism with a suitable passage for the seed to the melt surface.

The new furnace kept evolving according to the obtained results. Several configurations were investigated. We hereby present the major evolutions of the furnace on a construction point of view. These modifications were based on the need to enhance the cold top central seeding zone in the melt. Figure 2.3 shows a schematic and real view of the interior parts of the furnace for the new Kyropoulos configuration.

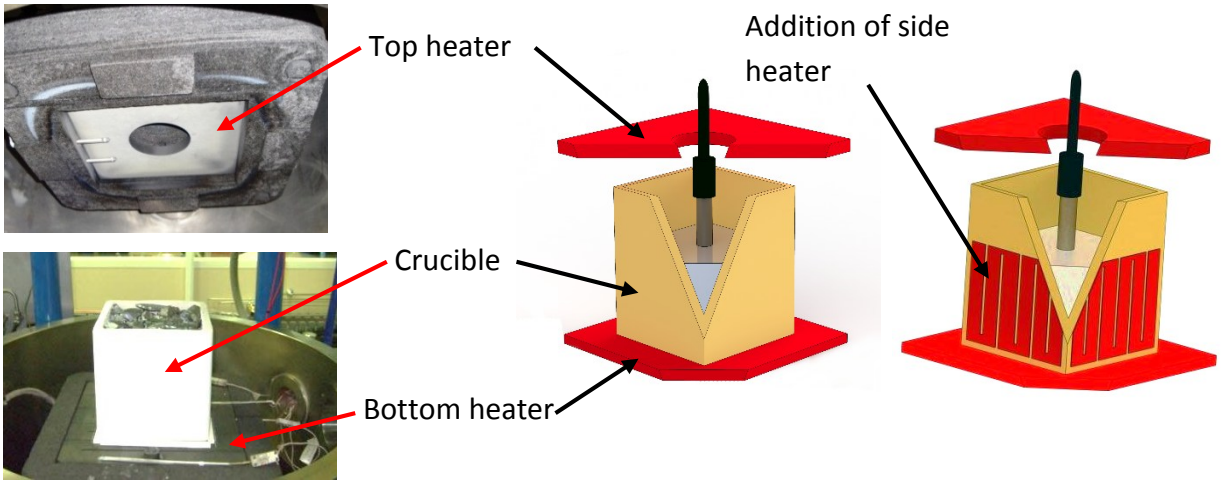

Figure 2.3. The heating elements for the new Kyropoulos configuration

The starting configuration had only a top and a side heating elements. There was no side heater in the starting point. The side heater was added in a later stage of the development.

A central circular cut with a diameter of 100 mm was created in the top parts including the insulation casing and the top heater (Figure 2.3). The top cut provided free passage for the seeding shaft to reach the melt; the top cut was also expected to enhance the cooling of the central seeding area on the surface of the melt by local radiation cooling.

A seeding shaft with vertical translation and axial rotation was added on the top of the furnace to accomplish the seeding procedure. The seed holder was a graphite cylinder of a diameter equal to 30 mm connected to a high sensitivity balance to monitor the apparent weight during the dipping of the seed as well as the crystal enlargement.

In order to enhance the control of the horizontal thermal gradients, a lateral heating element was added around the crucible to control locally heat losses from the crucible lateral walls.

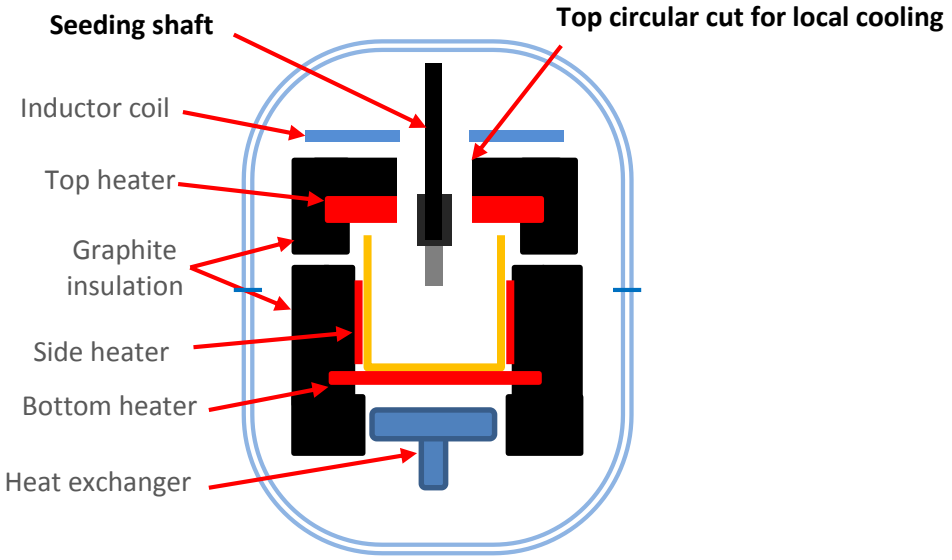

Figure 2.4. Schematic representation of the developed Kyropoulos configuration

The final configuration had three independent heat sources (Figure 2.3):

- a graphite resistor was placed below the crucible
- a graphite susceptor was placed on top of the crucible
- a side resistor was placed on the exterior side walls of the crucible.

Unlike other existing top seeding processes, the developed process for this investigation (Figure 2.4) had a square crucible rather than a cylindrical one. This choice was made to affect the shape of the final crystal in order to have a square horizontal section ingot. The crucible was 240 mm height over a square horizontal cross section 185x185 mm. About 9.5 Kg of silicon was used as charge. The melt had a depth of about 110 mm.

The crucible and the heating elements where surrounded by an insulation casing 100 mm thick on the side and about 30 mm thick on the top. The insulation was built with the superposition of several rigid graphite foam blocks. The whole insulation casing was placed inside a double layer stainless steel shell cooled with water (Figure 2.4).

The furnace had three main cold sources: the outer steel shell, the top inductor coil and the bottom heat exchanger. The listed parts are marked with blue color in Figure 2.4. The cooling of these parts was provided by a continuous flow of water and therefore considered at constant temperature close to ambient. The bottom heat exchanger was a plate with a square horizontal cross section of 300 x 300 mm and a thickness equal to 30 mm placed at about 25 mm below the lower resistor. Although not required by principle, the bottom heat exchanger was helpful to approximate the instant heat flux loss from the resistor to the outside environment for monitoring purposes.

The inductor coil was a circular spiral copper tube placed on top of the insulation casing. The inductor total diameter was about 250 mm. The distance separating the inductor coil and the top graphite susceptor was about 30mm.

The furnace had a pumping system for primary and secondary vacuum. The interior of the furnace was filled with a continuous flow of argon in an open circuit allowing to work under low pressure. Several inlets of argon were placed around the furnace to target different areas. The main jet of argon was blown from the top, directly upon the surface of the melt, to evacuate volatile impurities species away from the internal chamber. The argon was evacuated from the top of the steel shell.

II.1.1.2. 1 Modified configuration with a ceramic shield against radiation

A refractory tube was added around the seed and the seed holder to shield the central zone from the top heating element (Figure 2.5).

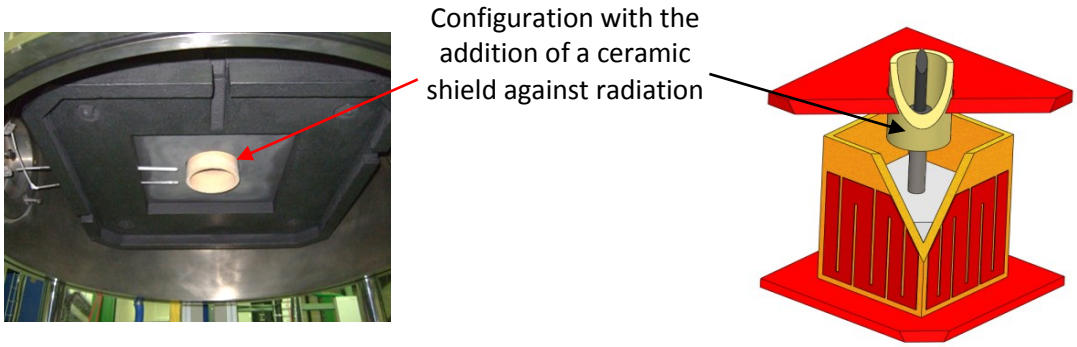

Figure 2.5. Addition of a ceramic shield inside the central top cut around the seeding parts

Figure 2.5 shows a real and schematic view of the added ceramic tube against radiation. More details about the screening effect on the seed and the silicon melt will be elaborated in the numerical results chapter.

The added radiation shield was a Zirconia ceramic tube with an external diameter of 95 mm and a thickness equal to 5 mm. the ceramic tube was about 300 mm in length. The tube was placed at fixed position. Its top was at the same level as the top of the insulation casing and its bottom was at the same level with the top of the crucible which is about 120 mm above the melt surface. Note that higher screening efficiency of the tube could be obtained if its bottom is closer to the melt surface in order to fully cover the seeding shaft and the central seeding zone; however, technical considerations limited the allowed length for the shield tube in order to allow maximum filling of the crucible with silicon chunks.

II.1.1.2. 2 Modified configuration with a water cooled tube for local heat extraction

In order to improve heat extraction from the seed and the top central zone, a cold copper tube cooled with water was added around the seeding shaft Figure 2.6. The bottom of the tube was at the same level as the base of the top heater. The tube was a long double layer copper cylinder of about 450 mm long. The external diameter of the tube was equal to 90 mm and the inner diameter was equal to 35 mm. The cold tube had two main functions:

- the tube shielded a part of the seeding shaft against radiative heat coming from the top heater

- At the same time, the cold tube provided a heat extraction sink for the seed holder as well as all the surrounding components by radiative cooling.

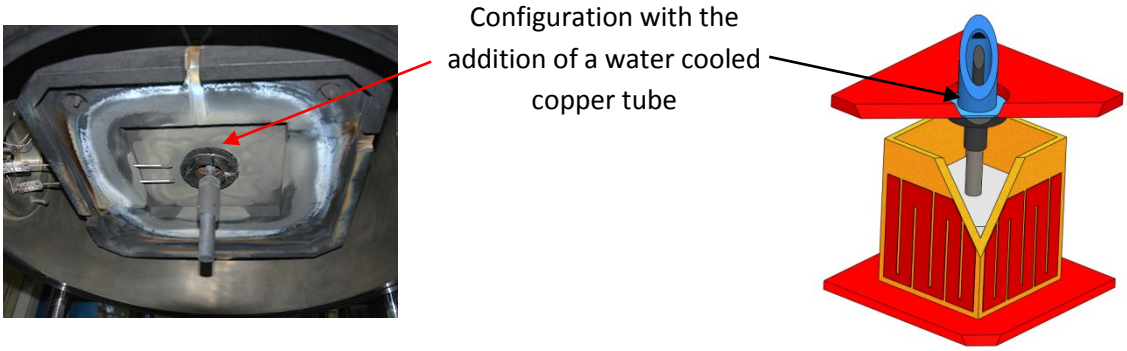

Figure 2.6. Addition of a cooled copper tube around the seeding parts as a heat sink

Next to these major modifications, continuous ongoing work kept modifying the insulation design, the seeding system, and the heating element configuration. These modifications will be mentioned along the manuscript when relevant.

II.1.2. Monitoring and measurement of experimental data

Important set of measurement instruments for temperature and flow were placed in the furnace to collect experimental data. The furnace was monitored by mean of thermocouples placed in key zones to acquire temperature readings during the full process. Figure 2.7 shows the placement of all the thermocouples in the furnace.

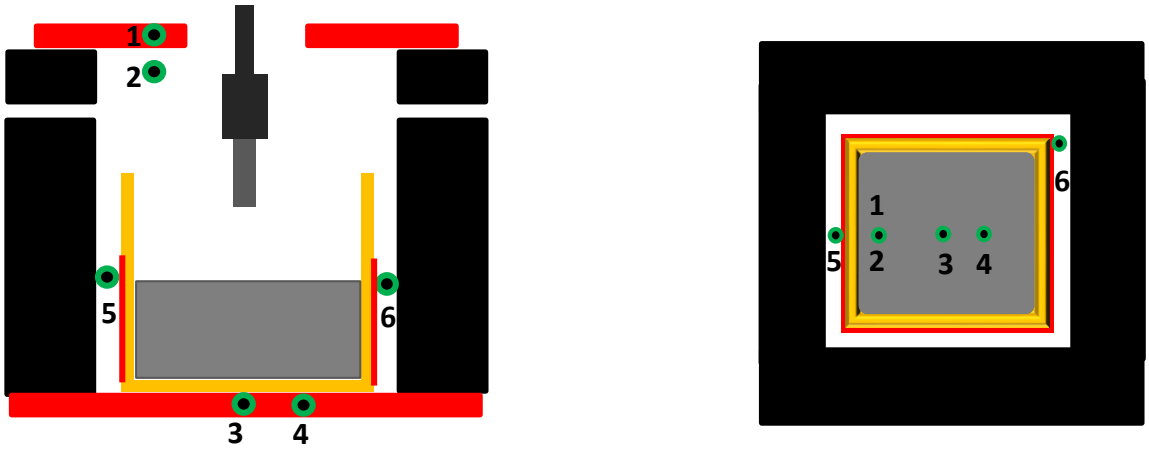

Vertical cross section view Top view cross section

Figure 2.7. Placement of thermocouples in the experimental furnace

The interpretation of the physical meaning of measured temperatures is highly related to the placement of the thermocouples. The thermocouples placed completely inside an opaque solid were considered as representative of the temperature of the solid itself, while the thermocouple placed in the argon atmosphere were representative of a weighted influence of all surrounding radiative surfaces. The thermocouples placed in the argon atmosphere served more for qualitative interpretations rather than quantitative measurements.

Thermocouple 1, 3 and 4 were, more or less, placed inside the heating elements and therefore giving the punctual temperature of the heating elements.

Thermocouple 2 was placed below the susceptor and its temperature was representative of all the radiating surfaces in the inner chamber including the silicon melt free surface and the inner walls of the crucible. At operating dipping conditions, the inner cavity was more or less isothermal and the readings of this thermocouple where predictable.

Thermocouples 5 and 6 presented in were affected by the lateral heater, the temperature of the facing internal wall of the insulation casing, the lower resistor and the exterior wall of the crucible. The values given by these thermocouples were particularly difficult to interpret since they are affected by several radiating surfaces at different temperatures.All the main streams of cooling water in the furnace were regulated by gate valves and monitored by flow meters and thermocouples.

Figure 2.8 shows a typical configuration of the water cooling circuit used for calibration purposes. The monitoring system of the water cooling circuit was designed to quantify experimentally the main heat fluxes exchanges in sensitive parts of the furnace. The heat evacuated by the outer steel shell helped to estimate the heat losses from the hot central core in the furnace, mainly radiated from the outer walls of the insulation casing. The heat evacuated by the induction coil was used to estimate the fraction of power passed by induction to the top heater as the effective top heating power in the process. The heat evacuated by the bottom heat exchanger was mainly received from the bottom heater. An experimental order of magnitude of the power passing through the crucible base to the silicon melt could then be estimated.

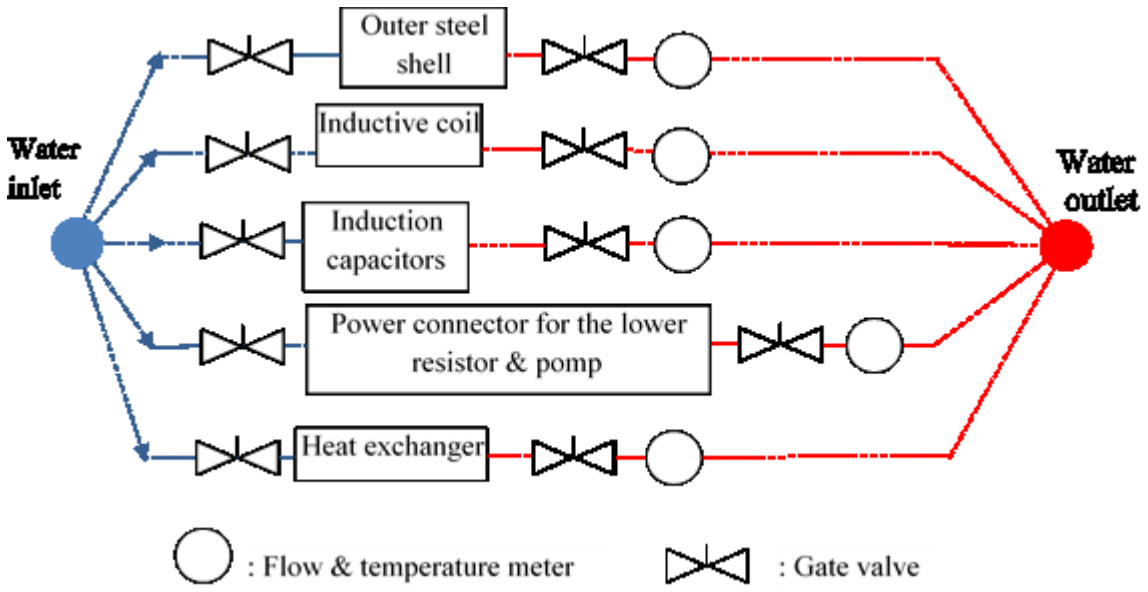

Figure 2.8. Monitoring of cooling water circuit in the experimental furnace

The range of temperature variation for each part of the cooling circuit at operating conditions in our configuration was between 3 and 25 °C. The error of the temperature measurement related to the equipment precision was 1.5 °C which is for example equivalent to 1500 W error in heat quantity estimation in the outer steel shell. The impact of this temperature measurement error on absolute values of heat power estimation increases for higher water flow rate; such notice is clearly illustrated in the heat extraction balance presented Figure 2.9 were error bares are larger for higher flow rates.

In addition, the estimation of heat extraction for cooling circuits with low variation in temperature (3°K) presented a 50% relative error in temperature measurement diminishing considerably the liability of heat loss value estimation. When possible, the flow rate of water in these circuits was decreased as low as possible to obtain higher temperature variation of the cooling water for better measurement accuracy. The flow rate measurements given by the flow meter were verified manually to be accurate.

A comparison between flow rates measured manually and flow rate read directly on one of the flow meters taken as an example. The average relative deviation was less than 2% in all the flow rate measurement devices (Appendix 2).

Most of the electric power injected in the lower heating resistor was transformed into volumetric heat inside the heating resistor. As a consequence, the effective heating power in the lower resistor was considered equal to the total electric power consumed by it. This heat power was assumed unifromly distributed in the lower resistor. The value of the electric power delivered to the lower resistor was calculated by mean of the voltage and the current values given by the power generator. The accuracy of these readings was verified by experimental measurements. The current deviation was less than 4% while the voltage had less than 0.2% deviations (Appendix 2).

Concerning the top heater, the effective heating power was the fraction of power transmitted from the inductor to the graphite susceptor. The rest of the power was lost as heat due to the electric resistance of the water cooled inductive coil. This heat loss did not contribute to the heating of the furnace core since it was evacuated outside the furnace by the cooling water running inside the inductive coil.

The effective heating power in the top heater was determined experimentally. The inductor coil received most of the surrounding heat by radiation since it didn't have any solid contact with the hot parts of the furnace. To lower this radiative heating during our measurements, the inductive coil was isolated by a thin sheet of soft graphite felt as a shield against radiation. For better accuracy, the measurement was done during the very first minute of furnace switch on where the external insulation walls were still at ambient temperature to insure their low participation in the heating of the inductive coil.

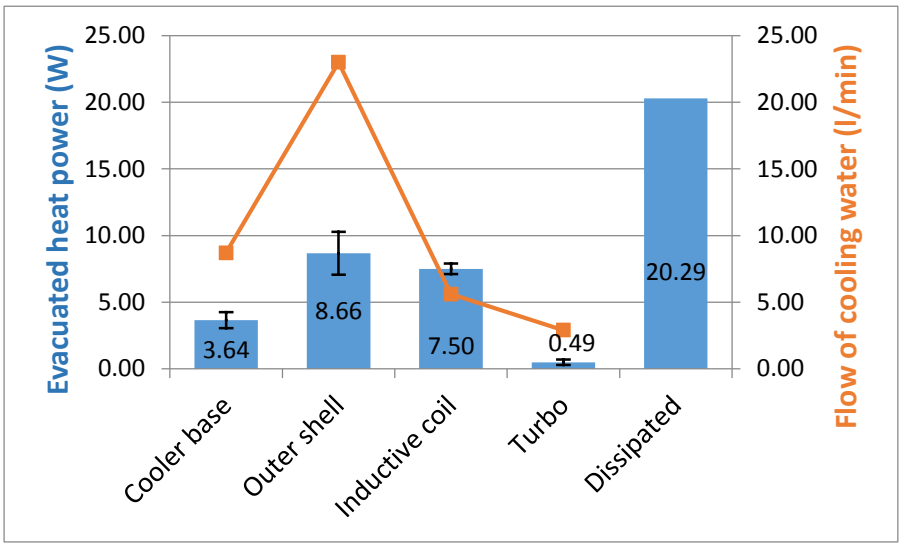

Figure 2.9. Heat power balance to estimate induction efficiency. Error bares based on temperature measurement errors.

The effective heating power in the top susceptor was approximated as the difference between the total injected electric power in the top inductive circuit and the heat loss evacuated from the inductive coil by cooling water. The electrical properties of the heating elements were considered as independent of temperature in the working range (900-1500°C).

According to the obtained results presented in Figure 2.9, the fraction of power passed by induction to the top heater was approximated as follow:

$$P_{eff} = 100 - \frac{P_{ind} \times 100}{P_{total}} = 100 - \frac{8.67 \times 100}{21.46} = 63\ \% \qquad (2.1)$$

Where $\boldsymbol{P_{eff}}$ is the power fraction transmitted to the top heating susceptor

The distance between the inductor and the susceptor in the experimental furnace was kept similar for all experiments in order to keep the same induction coupling conditions.

The furnace had several security systems to ensure the safety of the user and the equipment. These systems were carefully designed in order to not interfere with the process and therefore will not be detailed here.

II.2. Numerical model construction

II.2.1. Definition of the simulation domain and boundary conditions

The simulation domain was created as simple as possible while describing accurately the physical phenomena of interest (heat transfer and solidification). This step was a compromise between the required accuracy of the results and the calculation load. Some secondary features, or even complete volumes, were replaced by boundary conditions.

II.2.1.1. Constitution of the simulation domain

The present numerical study focuses on a solidification process controlled by hot and cold sources. Heat transfer is therefore a leading phenomenon defining the physical equations in this investigation. Since the furnace includes solid and fluid matter, where some of them are transparent to radiation, both conduction, radiation, and convection were considered. In addition, Phase change due to solidification is also included.

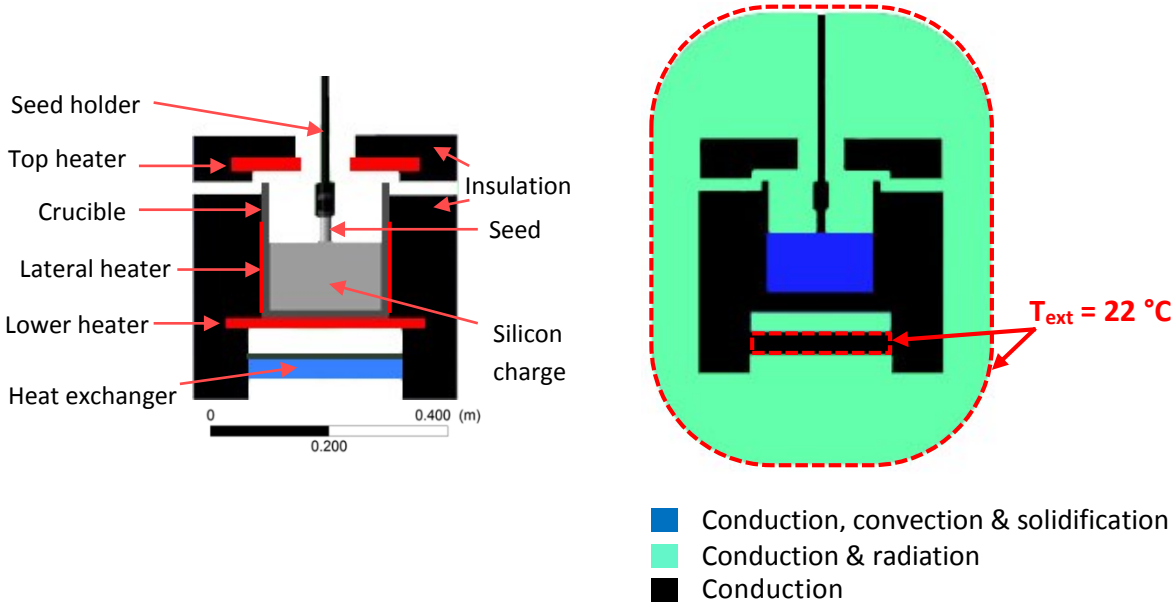

Figure 2.10. Physical phenomena of interest in the different parts of the furnace.

Figure 2.10 shows how the relevant physical phenomena listed earlier are located in the furnace. As a first approach, all parts of the furnace should have been included into the

simulation domain to reach the cold outer container; but, such choice may not be reasonable since it requires extensive calculating power.

II.2.1.2. Boundary conditions and simplification considerations

The volume of the actual studied furnace is about 0.5 m3 where great part of it is surrounding argon atmosphere. This argon atmosphere adds consequent number of calculation nodes to the simulation mesh while it is not the main zone of interest. The argon outside the simulation domain was replaced by a convective and radiative boundary condition to simplify the mesh generation and the node count. Heat exchange by radiation in the outer argon was approximated by radiation heat exchange between the boundary wall of the simulation domain and the wall of the steel shell.

$$Q_{rad} = \sigma \varepsilon_{eq} (T_{ext}^4 - T_{wall}^4) \quad (2.2)$$

Where $\boldsymbol{Q_{rad}}$ is the radiative heat transfer, $\boldsymbol{\varepsilon_{eq}}$ is an equivalent emissivity resulting from the two walls

The external steel shell was water cooled and its temperature considered constant T_{ext}=300k. The radiation condition was considered as a diffuse and gray radiation case between two facing walls where the total radiation emitted by one wall falls on the second one. An equivalent emissivity was calculated using the emissivity of the boundary wall of the simulation domain and the emissivity of the steel shell for the case of tow facing walls:

$$\varepsilon_{eq} = \frac{\mathbf{1}}{\frac{\mathbf{1}}{\boldsymbol{\varepsilon_1}} + \frac{\mathbf{1}}{\boldsymbol{\varepsilon_2}} - \mathbf{1}} \quad (2.3)$$

Where $\boldsymbol{\varepsilon_1}$ and $\boldsymbol{\varepsilon_2}$ are the emissivities of the two facing walls

Although heat convection by argon was reported to be less than 1% compared to heat transfer by radiation for comparable Czochralski furnace [15], we still included the convection of argon outside the simulation domain using convection boundary condition.

$$Q_{conv} = h_{Ar}(T_{Ar} - T_{wall}) \quad (2.4)$$

Where $\boldsymbol{Q_{conv}}$ is the convective heat transfer, $\boldsymbol{h_{Ar}}$ is the convective heat transfer coefficient

The argon temperature out of the simulation domain was taken equal to T_{Ar} = 573k based on values for comparable Czochralski configuration [16]. The outer walls of the simulation domain were not exposed directly to forced jet of argon; an average value of convective heat transfer coefficient has been considered as h_{Ar} = 25 w/m^{2}K [17]. We assumed, as an approximation, that convection effect was uniform on all the exterior walls of the simulation domain.

The seeding shaft passing through the center of the top hole was exposed to a consequent radiative heating coming from the core of the furnace. A cylindrical volume of argon connecting the seeding shaft and the top hole in the insulating casing was added into the simulation domain to account for this radiative heat transfer.

Note that the same situation applies for the interaction between the top surface of the insulation casing and the seeding shaft; however, these two walls had a lower temperature difference and a small view factor and therefore, their radiative heat exchange was neglected.

In the case of the added water cooled tube as heat extractor, an important part of the heat loss from the top of the insulation casing is actually collected by this cold tube. Although this heat loss is not collected by the cold tube it is still accounted for by an exact similar condition presented by the radiation boundary condition. In fact, the assigned radiation boundary condition accounts for radiation to the exterior steel shell having the same temperature and the same emissivity as the cold tube. The boundary condition is perfectly representative of the cold tube, assuming that there is no returning back of radiation heat.

The argon connecting the different parts inside the reactor at the core of the simulation domain was required as a transparent medium to radiation in order to activate the calculation of heat transfer by radiation. On the other hand heat transfer by convection of argon was

neglected. The used argon flow in the present investigation varied from 6 to 17 l/min. According to these values, a maximum of 300 Watts of heat is extracted by argon from the whole internal cavity which has very low impact on the temperature variation in the core of the furnace.

The argon was defined as a solid matter transparent to radiation when the discrete ordinate radiation model (DO) was used. Such consideration was not possible in conjunction with the surface to surface radiation model (S2S) in Fluent software since it requires all transparent medium to radiation to be fluid as a technical specification. The argon inside the simulation domain was defined as a fluid with a constant density and with no thermal expansion to supress buoyant convection. The argon zone inside the simulation domain did not have any inlet or outlet conditions and therefore was not subject to forced convection as well. The boundary condition of the argon inside the simulation domain was defined as completely transparent were all out going radiation fall directly on the exterior steel shell.

The inductor coil on top of the top heater and the heat exchanger below the lower resistor were water cooled; there was no need to include those in the simulation domain since their temperature remained constant during the full process.

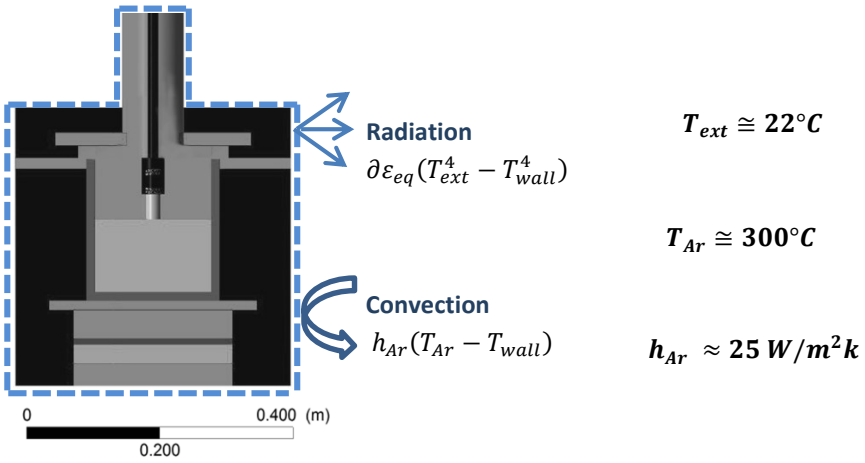

Figure 2.11. The simulation domain with the main corresponding boundary conditions

Combining all prior assumptions, the simulation domain can be defined as presented in (Figure 2.11).

The current configuration had few thin features characterized by high form aspect ratio where the thickness is much smaller compared to the other dimensions. Such features were difficult to mesh and could not be neglected because of their important function or effect. The first thin feature in the furnace was the side resistors with the dimensions 300 x 200 mm over 2-6 mm thick. These graphite plates were modeled as an internal boundary wall with a virtual thickness. The virtual topology had the same material properties and function. A volumetric heat source was directly injected uniformly in these virtual resistors were the energy equation is solved to account for the injected heat source and the conductive heat transfer.

The second thin feature was a quartz plate placed between the top of the insulation casing and the inductor coil to act as an electric insulation. This quartz plate was 430 x 430 and 4 mm thick. The plate was replaced by a virtual topology subject to conductive heat transfer and an exterior radiation boundary condition.

Complex furnaces at high temperature usually present a challenging problem for numerical simulation because of non-perfect contact between the different parts. The bottom and top heating resistors did not have perfect contact with the bearing insulation casing. Such lack of contact was accounted for, when necessary, using an internal boundary condition to replace conductive heat transfer by an equivalent radiative heat transfer based on the assumption that all radiative heat emitted by one cell of the heater wall falls totally on the facing cell of the insulation wall.

II.2.1.3. Creation of the 3D geometry and the mesh and symmetry consideration

A 3D geometry of the simulation domain including all the internal parts of the furnace was created using ANSYS design modeler

The geometric symmetry is a very powerful numerical tool that can produce quick and reliable results for many cases of studies, however, a perfectly symmetric geometry do not

necessarily imply a perfect physical symmetry. It is crucial to consider if the simulated physical phenomena are symmetric according to the considered geometric symmetry. Furthermore, the robustness of the symmetry should be considered as well. Such effect is a physical property of the real process defined as the capacity of a symmetric process to recover its symmetry after the recurrence of a perturbation. The perturbation can be internal such as the shape change of the solid phase; or, it can be external such as an instant injected fluctuation of the temperature or the velocity.

The melt flow and solidification were expected to be highly asymmetric in the present investigation of Kyropoulos process and therefore full geometry of the simulation domain was considered in the final model. Further results in the fourth chapter will show the pertinence of this choice.

The 3D geometry was an assembly of several parts of each component of the real furnace. The created CAD parts had the same morphology and dimensions as the experimental setup. The parts were grouped into one assembly to form the simulation domain

II.2.1.3. 1 . Meshing operation and quality verification

The creation of a mesh in a multi parts system is a complex task since the mesh requirements may changes from one part to another. The generation of the mesh in the present investigation was done in two main steps:

1. At first, a surface mesh was created on a horizontal cross section of the simulation domain. A condition of '' all quad '' was assigned to generate quad cells on the entire section. Sizing functions were applied on the surface to impose finer mesh resolution in the silicon domain (2 to 4 mm cell size) with a gradual increase of the cell size towards the peripherals of the simulation domain (5 to 7 mm). The finer mesh resolution in the silicon domain was required for the calculation of fluid mechanics and solidification.

2. In a second step, the created surface mesh was then swept along the vertical direction to mesh the whole volume of the simulation domain while keeping hexahedral finite volumes. The approach was required to keep the quality of the mesh; but, resulted in a high count of

cells. The mesh generation was based on a conformal mesh transition since non-conformal mesh transition is not compatible with the S2S radiation model in Fluent software.

The geometry of the different parts in the simulation domain had either circular or square horizontal cross sections. The passage from one form to the other was performed using multi-zone meshing algorithm.

The quality of the mesh was verified using standard metrics (especially cells skewness, aspect form ratio and smoothness) to avoid false simulation results and even complete divergence. Since the current work is based on ANSYS Fluent simulation package, the considered metric values were those preconized by Fluent documentation; a maximum skewness limit of 0.8 was used. The maximum size increase between two adjacent cells was kept less than 20% in the silicon melt. The highest value of cell growth rate of 20% was the one assigned to the boundary layers while the rest of the melt had less than 5% size change between adjacent cells in the melt volume.

The corresponding metrics statistics for the created mesh, for skewness are presented in (Figure 2.12).

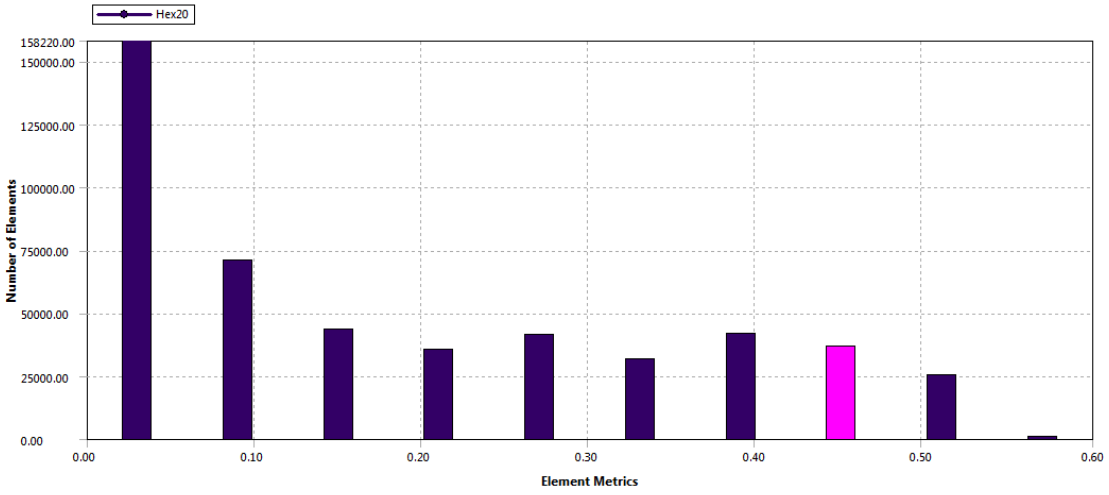

Figure 2.12. Skewness Mesh metrics for quality verification; most of the elements has skewness less than 0.3

The skewness criteria was particularly detrimental for the present investigation and great effort was made to keep it as low as possible as shown in Figure 2.12.

The prior metrics are required conditions but not sufficient. The validity of the mesh can only be satisfied if the spatial resolution of the mesh is high enough to not affect the simulated solution of the physical phenomena. A mesh independent study is one way to check the prior listed condition. Values of temperature, velocity and heat fluxes were compared for several degree of mesh refinement to identify the point where the mesh refinement effect on the solution become negligible. Three degrees of mesh refinement were applied and tested:

1. A mesh with 10^5 cells
2. A mesh with $6x10^5$ cells
3. A mesh with $1.6x10^6$ cells

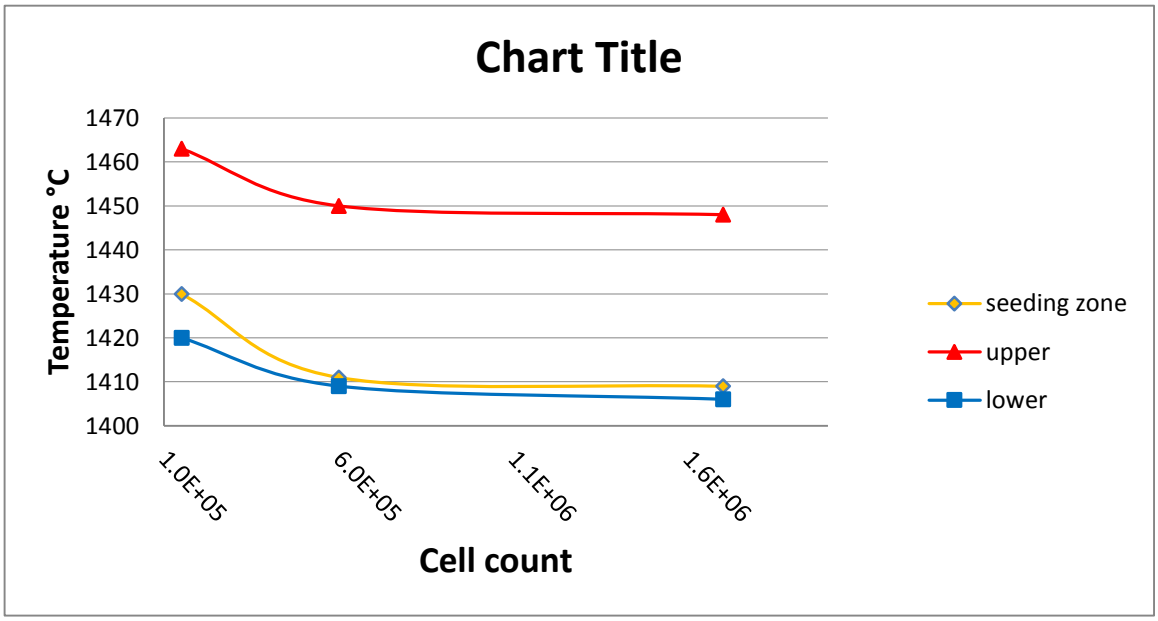

Figure 2.13. Evolution of calculated temperature at different positions in the furnace according to mesh resolution

The melt zone, undergoing a combination of conduction, convection and solidification, required higher mesh refinement compared to the rest of the simulation domain. Figure 2.13

Figure 2.13 shows the temperature evolution according the increase of the cell counts in the mesh for different specific points inside the melt (central seeding contact zone at the surface of the melt) as well as the temperature in the top and lower heating elements.

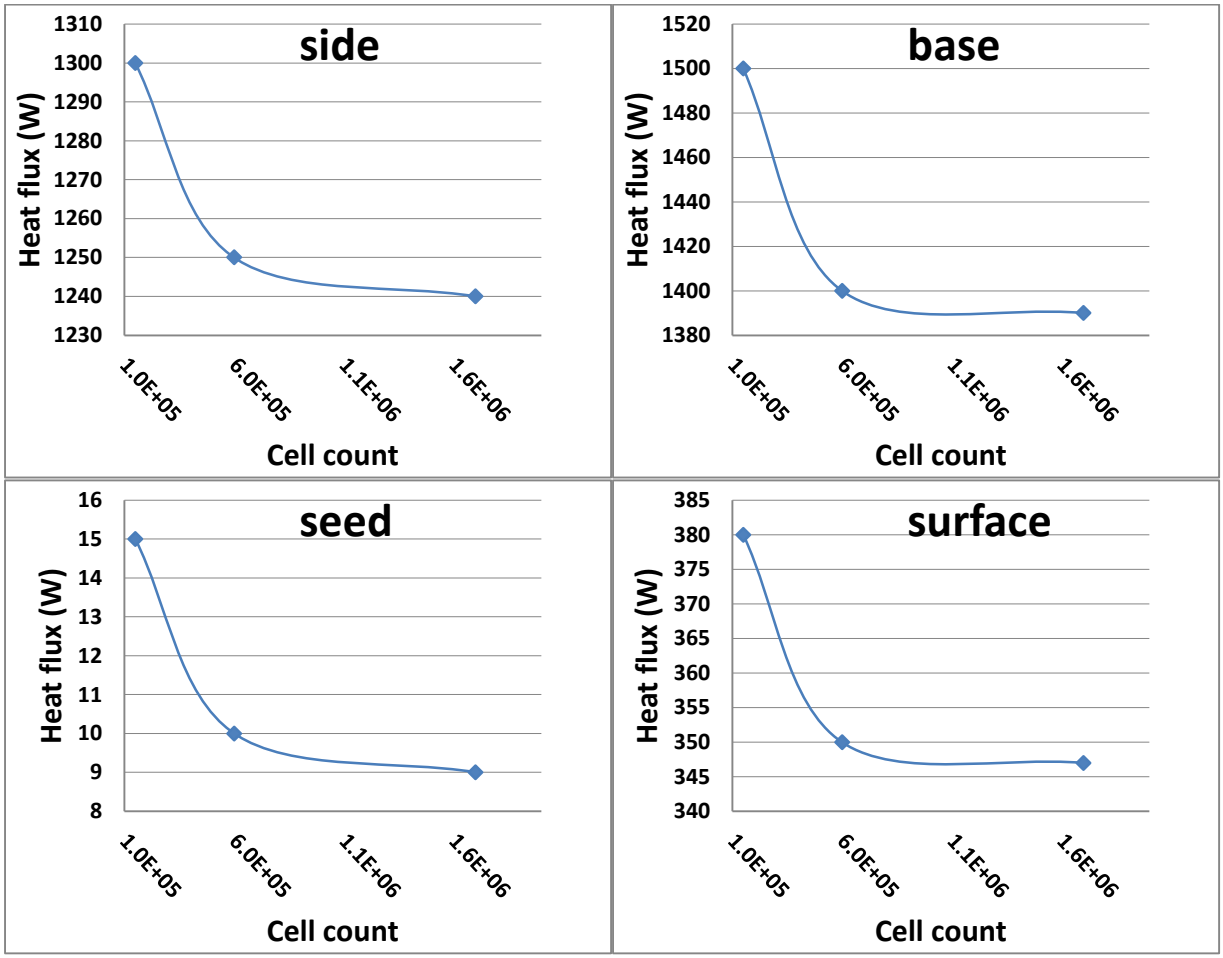

Figure 2.14. Evolution of calculated heat flux at different walls of the silicon charge according to mesh resolution

Figure 2.14 shows the calculated values of heat fluxes for the same geometry under exactly the same condition but with different mesh resolution. The coordinate on the x axis has the total number of finite volumes in the mesh.

Note that, starting from $6x10^5$ cells, for our configuration, the variation of temperature is less than 0.5% in the next step of mesh refinement with a factor of 1.5 more cell count. The

curve shows a clear tendency to a stable value indicating that the calculated solution is no longer dependent on the mesh resolution.

The same behavior can be observed in the evolution of the heat flux exchange at the walls of the silicon melt where the different graphs indicate that the solution do not change mush starting from a mesh with $6x10^5$ cells. Note that the case of the heat flux exchange from the seed present a high error even if the seeding zone is the most refined part in the whole mesh. This error is accentuated by the low value of the monitored physical variable. Inflation layers consideration

Inflation layer were created on the edges of the silicon domain adjacent to the sides walls of the crucible. The inflation was created to simulate flow and heat transfer in the boundary layer next to the side walls. A finer inflation of 20 layers starting from a first layer of 0.1 mm and a growth factor of 1.2 was created and tested to serve for our simulation cases.

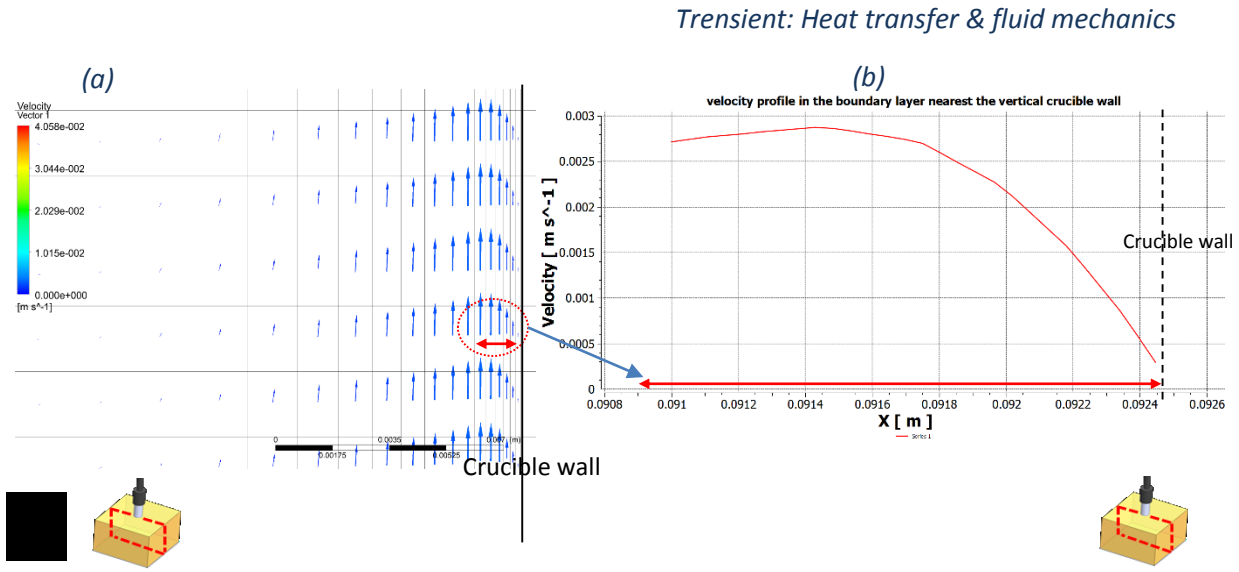

Figure 2.15. Velocity profile in the boundary layer nearest to the crucible vertical wall.

A non-slip condition was assigned near the wall. Heat transfer between the fluid and the wall is quite important for our investigation and may require thin mesh near the wall. The thin viscous sub layer is about 100 times smaller than the log region which requires a very high cell count to be fully meshed.

As a solution, Fluent offers the possibility to use RANS models with wall function to approximate this transition using a lighter mesh density. This solution is quite effective for estimating general velocity profiles however it has its limits and the total log region thickness is about 0.015m.

Figure 2.15 shows the velocity profile in the boundary layer next to the vertical wall of the crucible. The profile was obtained from transient calculation case including heat transfer and fluid dynamics stable for 1000 seconds flow time using 0.1 time step. Physical and experimental conditions for the model making

The melt is 0.120 m deep; its temperature totally above the melting point using the most advanced configuration of the furnace with a top cold tube. The illustrated profile of velocity near the wall is taken at mid vertical depth. The size of the first cell in the boundary layer is 0.001 m corresponding to a value Y+ equal to 30 where the first cell is located in the log region. The boundary layer has 15 cells at 20% growth rate.

II.2.1.4. Force balance for the floating silicon crystal in Kyropoulos process

Unlike most of metals and metalloids, solid silicon has lower density compared to liquid silicon and therefore silicon crystals float on molten silicon.

The main goal for the following discussion is to validate to main assumption in the numerical model:

1. Without pull up, the crystal stays fully immersed in the melt
2. The change of the height of the melt caused by the growth of the crystal is small and can be neglected

The analysis will also help to familiarize the reader with the notion of real and apparent mass in the experimental process. Two main points need to be clarified:

- The balance of the acting forces on the crystal needs to be established in order to understand the apparent weight given by the balance in the experimental setup

The resulting melt height variation during the growth under the assumption of no pull up needs to be calculated in order to make the right approximation of the met free surface position in the numerical model. An immersed silicon crystal in a melt can be subject to three main forces (Figure 2.16):

- Mass of the crystal (including the meniscus mass)
- Buoyancy force
- Tension forces

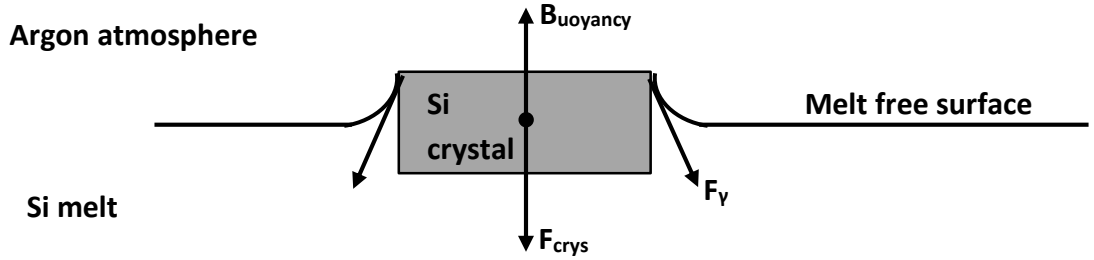

Figure 2.16. The main acting forces on a crystal in Kyropoulos configuration

In the general case, the total resulting apparent weight can be given as:

$$F_M = F_{Cry} + F_{menisc} = \rho_S g V_{Cry} + \rho_L g V_{menisc} \quad (2.5)$$

Were $\boldsymbol{F_{Cry}}$, $\boldsymbol{V_{Cry}}$, $\boldsymbol{F_{menisc}}$, $\boldsymbol{V_{menisc}}$ are respectively the weight and the volume of the crystal and the meniscus, $\boldsymbol{\rho_S}$, $\boldsymbol{\rho_L}$ are the densities of solid and liquid silicon and $\boldsymbol{g}$ is the gravity acceleration vector

The meniscus weight is function of the liquid meniscus volume which can be approximated, for the case of large diameter crystals with flat bottom, as:

$$V_{menisc} = S_c h_{meniscus} \quad (2.6)$$

Where S_c is an equivalent vertical projection of the contact surface and $h_{meniscus}$ is the meniscus height

For Kyropoulos configuration without any pull up of the crystal, a meniscus forms only by the first contact between the seed and the melt at the beginning of the process. After the full solidification of the meniscus, the expansion of the crystal continues inside the melt without meniscus and consequently the top of the crystal is at the same level with the free surface of

the melt. As a consequence, the height of the liquid meniscus is null and therefore no additional meniscus weight is applied at advanced stage of the growth.

The floatability force is a direct consequence of the immersed state of the crystal inside the melt. The balance between floatability and masse forces depends on the ratio between the density of the liquid and solid states. In a similar way, the floatability force can be given as:

$$F_{buoy} = -\rho_L g V_{Cry} \quad (2.7)$$

Were V_{Cry} is the volume of the crystal, ρ_L is the density of liquid silicon and g is the gravity acceleration vector

The weigh and floatability forces of the crystal are both resulting from the gravitational field. Both vectors are vertical but in opposite directions. For the tension forces, we assume that the crystal is axis symmetric and therefore the resulting horizontal component of the surface tension force reduces to null. Only the vertical component of the tension force is required in the global balance.

The force of the surface tension can be expressed as a function of the crystal perimeter and the surface tension of silicon melt. In our case, we may write that:

$$F_\gamma = L\gamma_{si} n \;\rightarrow\; F_{Y-\gamma} = L\gamma_{si}\; n \sin\theta \quad (2.8)$$

Where L is the length, γ_{si} is the surface tension , n is direction norm wettability angle and θ is the angle between the free surface of the melt and the top surface of the crystal at the three point junction.

The fact that there is no pull up and the top surface of the crystal is at the same level and parallel to the free surface of the melt, $\sin\theta$ reduces to zero and the vertical component of the surface tension force is null for symmetric growth. The resulting balance of forces acting on the crystal in our configuration at equilibrium can be written as:

$$F_{Mcry} + F_{buoy} = 0 \quad (2.9)$$

Were $\boldsymbol{F_{Cry}}$, $\boldsymbol{F_{buoy}}$, are respectively the weight of the crystal and its floatability

II.2.1.5. Interpretation of the apparent mass measured experimentally

The crystal in Kyropoulos process for silicon is floating on the surface of the melt. This outcome can be deduced from the force balance given by eq.2.9 The latter can be elaborated in a more readable form such as:

$$\frac{dM_{app}}{dt} = \frac{dM_s}{dt} - \rho_L \frac{dV_S}{dt} \quad \textbf{(2.10)}$$

In one particular instant in time, eq.2.10 will be:

$$M_s = \frac{\rho_S}{(\rho_S - \rho_L)} M_{app} + M_0 \quad \textbf{(2.11)}$$

Where M_s is the real mass of the crystal, M_{app} is the apparent mass of the crystal given by the balance during the full immersed state, M_0 is the initial mass

Eq.2.11 gives the masse of the growing crystal inside the melt in the present configuration as a function of the apparent mass read on the experimental balance. This value can be used in further form such as:

$$V_T = V_0 + V_S \left(1 - \frac{\rho_S}{\rho_L}\right) \quad \textbf{(2.12)}$$

Where V_T is the total volume of the melt+crystal completely immersed inside the melt, , V_0 is the initial melt volume, V_S is the crystal volume

Which leads to the following equation:

$$H_{melt} = \frac{1}{S_{melt}} V_0 + \left(1 - \frac{\rho_S}{\rho_L}\right) \left[\left(\frac{\rho_S}{(\rho_S - \rho_L)} M_{app}\right) + M_0\right] \quad \textbf{(2.13)}$$

Where H_{melt} is the height of the melt, S_{melt} is the surface of the inner base of the crucible, V_0 is the initial melt volume, M_0 the initial apparent weight, usually null if the balance is initialized at the start of the growth.

Eq.2.13 shows that it is possible to deduce the resulting height of the melt at any instant during the crystal growth by knowing the initial mass of the melt and the apparent mass of the immersed crystal, if the crystal is fully immersed inside the melt. Figure 2.17 shows the

evolution of the melt height and the crystal mass as a function of the apparent mass read experimentally on the balance.

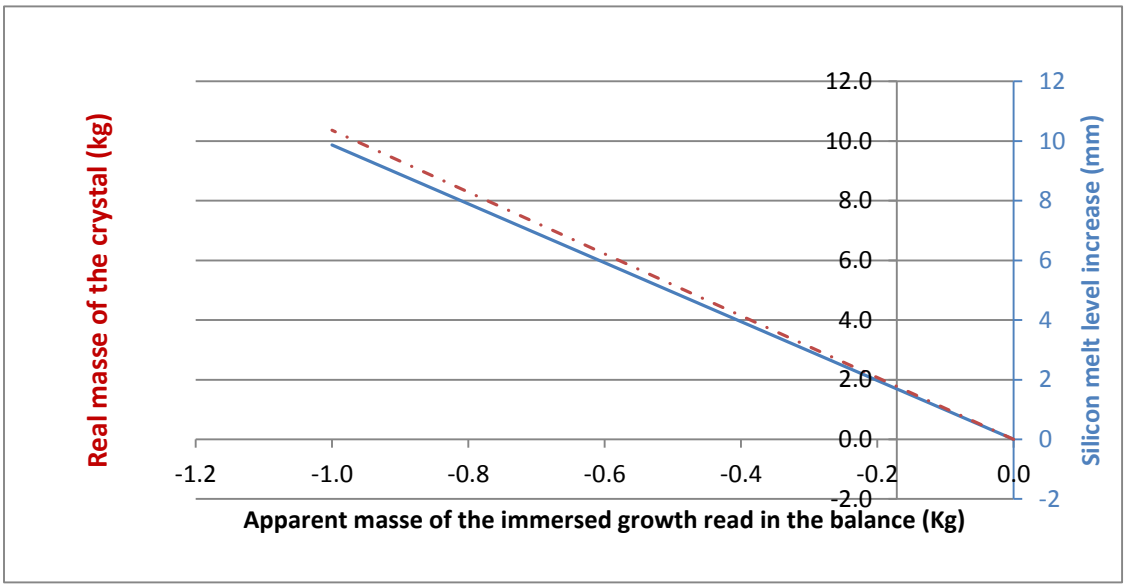

Figure 2.17. Growing crystal real and apparent mass and silicon melt level (no pull-up and fully immersed crystal)

The minus sign in the apparent mass results from the fact that floatability forces are higher than weight forces for silicon and therefore the resulting force is in the reversed direction of gravitation. Note that, for the present dimension of the crucible, the interface of silicon melt will rise 1 mm in height if we immerse a 1 Kg silicon crystal inside the melt. The assumption for the present numerical simulation that the free surface of the melt do not rise much during the growth of the crystal in the present Kyropoulos process without pull up is satisfied.

The following schematic representation in Figure 2.18 summarizes the evolution of apparent and real mass during a typical seeding procedure in the current process. This graph is for the case where to crystal is fully immersed in the melt without any pull up of the crystal. The graph is built under the assumption that the crystal is growing with no remelting of the crystal or the seed. Any possible residual existing forces due to surface tension and capillary are neglected and not considered in this graph:

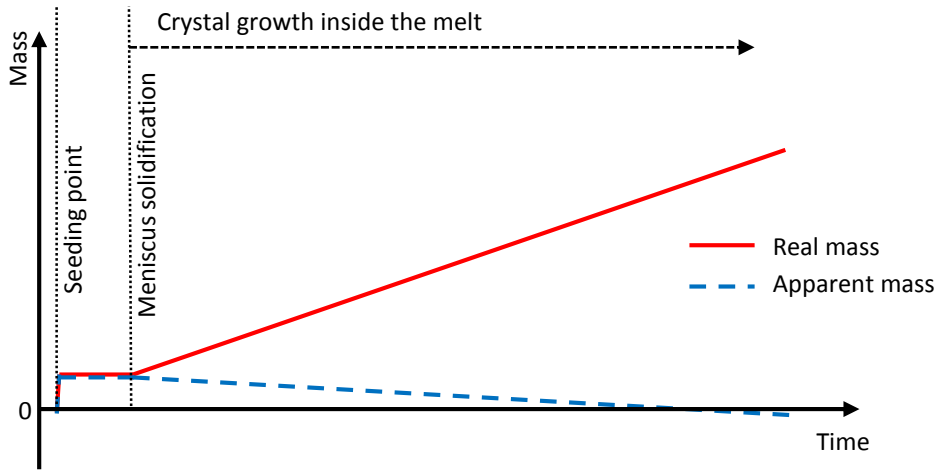

Figure 2.18. Schematic representation of real and apparent mass evolution in Kyropoulos for a fully immerged crystal with no pull-up.

Note that the apparent and real mass are can be supposed similar when the additional mass is above the free surface of the melt. This case in Figure 2.18 represents the total solidification time of the meniscus. However, the real mass is different than the apparent mass when the growth is below the melt surface due to floatability forces.

II.2.1.6. Verification of total immersion state of the growing crystal

The prior analysis was made based on the assumption that the crystal is totally immersed in the melt; but, how true is this assumption for the present experimental furnace? For a free floating silicon crystal, this assumption is not verified since about 1/10 of the floating crystal will immerge outside the melt. However, the growing silicon crystal in the present experimental configuration is not in the free floating state, two different experimental devices were used to hold the seed and therefore, two cases are to be discussed:

- the use of a rigid shaft as a seed holder
- The use of a suspended 2 kg load seed holder using a metallic chain.

In the case of a rigid shaft, the crystal is forced in position due to the rigid nature of the seeding graphite cane. Consequently, all the growth happens below the surface of the melt and therefore the assumption of a total immersed crystal is fully verified.

In the case of the suspended 2 kg seed holder, the graph in Figure 2.17 shows that the 2 kgf applied by the seed holder load are still higher than the maximum floatability force applied by a 10 kg crystal which is about 1.2 kgf of reversed floatability force. Since the used initial charge of silicon in this investigation is below 10 kg, the crystal will never grow as large to develop enough floatability to immerge from the melt. The assumption of a totally immersed crystal, when no pull up is applied, is also verified for the second configuration.

One should keep in mind that this configuration may present an unstable crystal position in the center. In fact, the gravity is the main force that maintains the crystal stable in central position. The added load should be calculated according to the maximum expected size of the crystal in order to keep the mass higher than floatability forces.

II.2.2. Model elaboration and simulation tool

The present simulation work was performed using the commercial package ANSYS FLUENT based on finite volume method. FLUENT is well-known for modeling fluid dynamics problems coupled with heat transfer. It also includes a native module to simulate solidification. The code offers the possibility to implement customized user defined functions to cover complex geometries and processes.

Fluent software includes several solving algorithms and discretization technics presented to the user choice in order to cover a wide range of flow regimes and heat transfer modes. A parametric study of the melt flow in our configuration is presented in attempt to predict the nature of the flow (turbulent or laminar) as well as the leading properties for momentum and heat diffusion in the melt in order to choose the adequate solving algorithms and meshing techniques for fluid mechanics.

II.2.2.1. Fluid dynamics in the melt and Nature of the flow in the present configuration

The resulting melt flow in the present investigated Kyropoulos process is mainly an interaction between natural convection from buoyancy flow, Marangoni effect from surface tension and viscous forces from the crystal rotation. In addition to the former volumetric

forces, consequent alteration of the melt flow results directly from the square shape of the crucible. A simplified approach can be applied to estimate an order of magnitude of these different forces using inputs from the current investigated process, more details about these values can be found in a later chapter.

The velocity and the effective viscosity were estimated using a preliminary simulation in order to evaluate the order of magnitude of the different acting forces. Dimensional numbers are also calculated using the characteristic parameters of the process to understand the nature and the behavior of the flow in the melt. This first approach will serve as a guide line to determine the most influencing parameters in our process. The major acting forces and characteristic numbers are summarized in table 2.1:

Table 2. 2.1. Summary of calculated characteristic forces and dimensional numbers for the melt in the present investigated Kyropoulos process for silicon

Buoyancy forces	$\rho.\alpha.g.\Delta T = 2533 * 9.82 * 10$	$17.5\ N/m^3$
Viscous forces from crystal rotation	$\eta_{tur}\frac{U}{L^2} = \eta_{eff}\frac{0.05 \times 0.25}{0.1^2}$	$0.024\ N/m^3$
Marangoni forces	$\gamma\frac{\Delta T}{L^2} = \frac{-2.8 \times 10^{-4} \times 10}{0.1^2}$	$0.25 N/m^3$
Pe	$\frac{U_{ref}\ L}{\alpha} = \sqrt{\mathrm{Gr}}\ Pr$	≈ 300
Gr	$\frac{g\beta\Delta T L^3}{\nu^2}$	$\approx 5.10^8$
Pr	$\frac{C_p\eta}{\lambda}$	≈ 0.0134
Ra	$Pr.Gr$	$\approx 7.10^6$
Re	$\frac{UL}{\nu}$	≈ 12000

The buoyancy force, resulting from density change due to thermal gradient is, presumably, the major driving force in the melt flow with a value equal to 17.5 N/m^3 in the current investigated configuration. The Marangoni effect resulting from the range of thermal gradient in our configuration (1-2 K/cm) is two orders of magnitude lower than the buoyancy force and very localized on the free surface of the melt. It is worth noticing this preliminary approach takes into account forces averaged on the whole system. Though Marangoni effect

is low at the global scale of the process, due to small temperature gradient, its contribution can be locally higher. The viscous force induced by the crystal rotation was estimated for a case related to the current investigation with a circular crystal of 100 mm in diameter turning at an angular velocity of 15 rpm. The resulting viscous force is three orders of magnitude lower than the buoyancy force with only 0.024 N/m^3 force intensity. Considering the prior results, the global melt flow in the studied configuration is dominated by buoyancy force resulting from the thermal gradient in the melt as expected. Both Marangoni and viscous forces are localized and very small compared to Buoyancy force which makes their effect practically insignificant on the global melt in the present Kyropoulos configuration for silicon. It is to be mentioned that investigation on local small scales can be subject to much higher effect of localized volumetric forces, which is out of the scope of this study.

According to prior results, the driving flow in the Kyropoulos process results mainly from the buoyancy forces. The top zone is at lower temperature which makes the melt in a highly instable state giving rise to natural convection due to density variation if a certain critical value of inertial forces is reached. Bejan reported that the passage from conductive to convective heat transfer took place, in a comparable heating configuration, at a critical Rayleigh of 1027 [14]. The Rayleigh number in the current configuration (table 2.1), exceeds this value by three orders of magnitude which is consistent with strong buoyancy convection.

The silicon melt in the present configuration is a low Prandtl number flow exhibiting some particular characteristics. The low value of Prandtl number is a typical case in liquid metals and semiconductors with relatively high thermal conductivity. Such conclusion should be addressed with caution in the case of fluid with high Grashoff number. Numerical results, presented in chapter 3, show that convection will reshape consequently the temperature distribution in the melt.

The calculated Grashof number 5.10^8 confirms that the inertial forces are indeed higher compared to the viscous damping in the melt. This fact is a consequence of the low viscosity of silicon. The calculated value is equally a good indicator that the inertial forces may play a consequent role in heat transfer in the block melt. This can be clearly shown by comparing

conduction and convection using the Peclet number for heat transport. In spite of the low value of the Pr number, the high Gr number raises the Pe number, significantly describing an enhanced convective heat transport.

Several works presented the Rayleigh number as an indicator to qualify the extend effect of thermal and momentum properties of the flow in order to predict the nature of the melt. It was reported that the transition phase to turbulent flow through time dependent state occurs at lower Ra number for low Prandtl number fluid. Such transition is expected at the order of magnitude of Rayleigh number$\approx \mathbf{10}^6$ which is close to the value 7.10^6 obtained for our configuration (table 2.1).

The melt in our configuration is more likely to be dominated by laminar flow becoming time dependent in transition to turbulent. Some localized areas in the melt may be turbulent. Comparable case was reported by A.Popescu & D.Vizman where the silicon melt was defined at the limit of the transition from laminar to turbulent flow and the global melt was dominated by laminar flow [1].

Although, the melt was qualified to be mainly laminar on the global scale in our configuration, satisfactory convergence using the laminar flow model could not be obtained. This lack of convergence was attributed to the nature of the flow that exhibits a tendency for laminar to turbulent transition in some parts of the melt.

To calculate the fluid velocity $\vec{v}$ and its pressure p, the following equations of mass and momentum conservation were resolved.

$$\boldsymbol{\nabla}.\vec{\mathbf{v}} = \mathbf{0} \qquad \textbf{(2.14)}$$

$$\boldsymbol{\nabla}.(\boldsymbol{\rho}\,\vec{\mathbf{v}}\vec{\mathbf{v}}) = -\boldsymbol{\nabla}\mathbf{p} + \boldsymbol{\nabla}.\overrightarrow{\overrightarrow{\mathbf{T}}} + \boldsymbol{\beta}(\mathbf{T}-\mathbf{T_0})\boldsymbol{\rho}\vec{\mathbf{g}} \qquad \textbf{(2.15)}$$

Where, $\vec{f} = \beta(T - T_0)\rho\vec{g}$ is the body forces density, due to buoyancy, and $\overrightarrow{\overrightarrow{T}}$ is the stress tensor containing viscous and turbulent friction term as presented in Fluent documentation[2].

Although the change of density in the melt was considered to calculate buoyancy forces using Boussinesq approximation for incompressible Newtonian fluid, the actual volume change due to density variation in the melt was neglected as well as the volume variation due to the phase change during solidification.

The simulation was solved in Fluent ANSYS as a 3D double precision case. The second order upwind discretization was used for convection and the SIMPLEC algorithm was used for pressure–velocity coupling. (PRESTO) scheme was chosen as the Pressure Staggering Option for pressure interpolation.

Both k-epsilon and k-Omega turbulent models provided satisfactory converged solutions for the melt convection. Notice that the two models, k-epsilon and k-omega provided comparable results. This similarity in solution is partially due to the low fraction of turbulent flow in the total scale of the melt.

II.2.2.2. Simulation of solidification in Fluent Ansys

The solidification in the silicon melt was accounted for using the liquid fraction model of Fluent, based on enthalpy porous method [2].

The simulation of solidification takes place in the predefined melt volume where the solid liquid interface progresses inside the volume. There was no physical pull up of the crystal in the numerical model. Crystal rotation inside the melt was included using the native numerical pull velocity in Fluent solidification module. These numerical considerations, including no pull-up of the crystal and crystal rotation, are fully in compliance with the experimental working conditions.

The simulation of the solidification process was achieved in several steps obtained as follow:

1. At first, convergence of stationary calculation of energy equation was obtained.
2. Secondly, convergence of stationary calculation is obtained by adding fluid dynamics.
3. In a third stage, a transient calculation, of more than 10 minutes of process real time, is performed to obtain the final solution with a melt at dipping conditions before activating the solidification module.

The phase change in Fluent solidification module is expressed by mean of liquid/solid fraction (f_L) value calculated in each cell according to the temperature field and latent heat. Although there is a solid/liquid interface moving in the melt, the mesh do not change during solidification. The solid/liquid interface is not delineated by the mesh nodes. The interface is reconstructed by mean of interpolated contours of liquid fraction inside the cells undergoing phase change. Because of the existence of these partially solidified cells in the liquid fraction model, the liquid fraction solidification model may present some challenging concerns about the residual flow velocity in these cells as well as the full convergence of latent heat calculation as well. Good understanding of the model principles is required to comprehend and resolve these resulting issues.

II.2.2.3. Resolving the issue of the absence of solidification convergence criteria

The native solidification module in fluent do not have a dedicated convergence criteria for the calculation of latent heat which may lead to erroneous results. It is required to check if the resolution of the latent heat equation has fully converged in each time step calculation. The Fluent solidification module used in our investigation is intended for phase change taking place in a temperature range between a solidus and a liquidus values. However, the melt in our case is assumed to be a pure substance and therefore should complete the phase change transformation at constant temperature. In order to fit the model for the case of a pure substance, a small temperature difference was assigned between solidus and liquidus values to imitate the case of phase change at constant temperature. The specified temperature difference between the solidus and the liquidus in fluent can be as low as $\Delta T = 0.001\ K$.

The liquid fraction value for each cell in the melt domain, subject to phase change, is defined as:

$$f_L = \begin{cases} 0, & T < T_{solidus} \\ 1, & T > T_{liquidus} \\ \dfrac{T - T_{solidus}}{T_{liquidus} - T_{solidus}}, & T_{solidus} < T < T_{liquidus} \end{cases} \quad \textbf{(2.16)}$$

The lever rule defines the liquid fraction between the solidus and liquidus temperature giving a linear continuous variation of liquid fraction f_L values between 0 and 1. The latent heat content for each cell is now expressed in term of this liquid fraction such as:

$$\Delta H = f_L L \quad \textbf{(2.17)}$$

The energy equation becomes:

$$\frac{\partial}{\partial t}(\rho H) + \nabla . (\rho \vec{v} H) = \nabla . (k \nabla T) + S \quad \textbf{(2.18)}$$

Where H *is enthalphy*, $\boldsymbol{\rho}$ *is density* , $\vec{\boldsymbol{v}}$ *is fluid velocity* , S *is a source term*

The resolution of equation 2.18 for temperature is an iteration process between the energy equation (2.12) and the liquid fraction equation (2.10) since the two variables are dependent on each other. The iterative process is achieved in parallel with the ongoing calculation. As far as the current investigation shows, this subroutine of iteration do not have a proper convergence criteria. The latent heat equation is assumed to converge when all other residuals reach convergence. The present assumption may be true for a certain number of cases; but, the obtained results in this work show that this is not always verified.

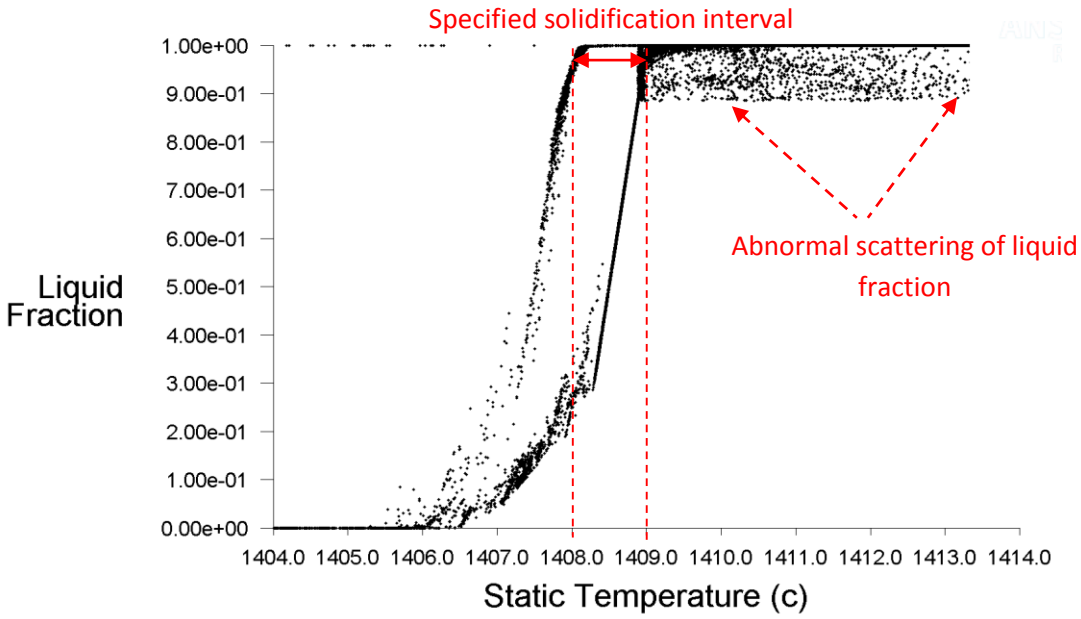

Figure 2. 19. Erroneous scattering of liquid fraction values as function of temperature due to bad convergence.

Figure 2. 19 shows the plotted liquid fraction as function of temperature in a chosen time step. The graph is a collection of points representing the liquid fraction in each cell of the melt domain as a function of temperature in the corresponding cell. The graph is resulting from transient calculation of a solidification case. This result was obtained for a fully converged time step according to Fluent convergence criteria of energy and momentum (including velocity and turbulence).

The chosen solidus and liquidus temperatures for this case are respectively 1408 -1409 °C. Several points are clearly out of range and keep oscillating during the iterations which is typical for iterative resolution. If a large number of iterations are calculated, all points should end up close to the prescribed straight line relating liquidus and solidus temperatures. However, this requires a minimum number of iterations that can be much larger than the number required for the convergence of all other residuals. The required minimum number of iterations is hard to predict since it changes from one step to the other. In this particular simulation case, 150 iterations were required in some time steps to reach correct representation of liquid fraction as a function of temperature. For comparison purposes, the

required number of iteration in this calculation to reach full convergence for all Fluent residuals was about 20 to 30 iterations in each time step.

Such deviation is not present in all solidification cases; but, we can see clearly in Figure 2. 19 how bad is the convergence of latent heat calculation in our case. It is not clear what amplifies this erroneous effect in the present configuration; however, the imposed rotation of the crystal is suspected to aggravate this effect.

In the context of this work, a simple convergence criteria is proposed to insure proper full resolution of the iterative subroutine between latent heat and temperature calculation. The sub routine was implemented in Fluent by mean of a user defined function as a solidification convergence criteria. The applied criteria was based on two major verification:

- On one side, the criteria verified that the liquid fraction value do not change above a certain minimum residual between iterations.
- On a second side, the criteria verified that the liquid fraction, as a function of temperature, has a limited deviation from the linear variation of liquid fraction between the liquidus and the solidus prescribed by the lever rule.

The graph resulted from calculation of a solidification case exactly similar to the case used to obtain the erroneous results presented earlier in Figure 2. 19 with the same solidus and liquidus range (1408 -1409 °C) and with the same simulation parameters.

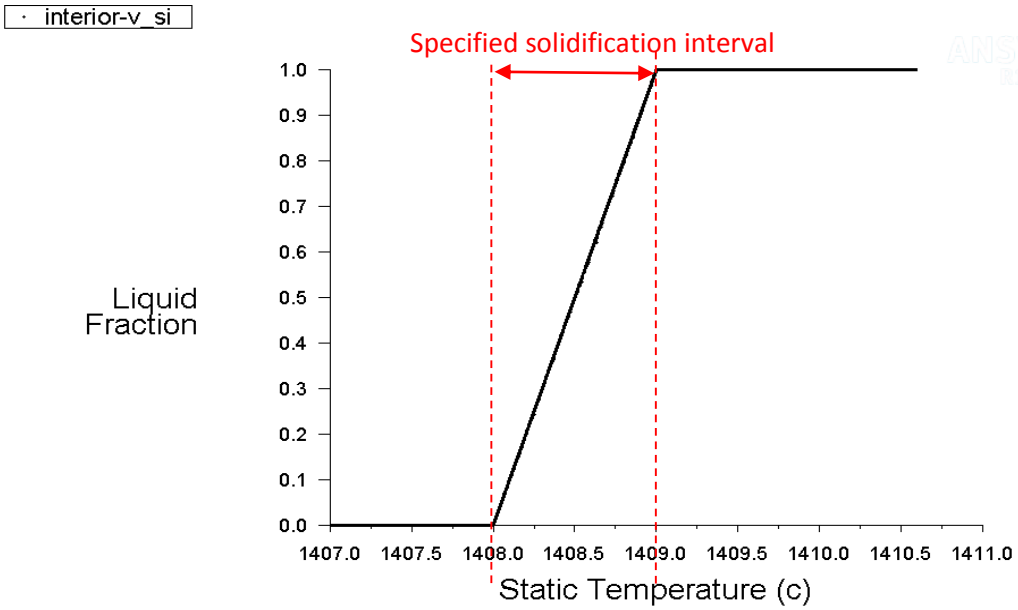

Figure 2. 20. Fraction values as function of temperature for a correctly converged solidification calculation using our convergence test routine

Figure 2. 20 shows liquid fraction variation as a function of temperature in a well converged case obtained after the implementation of our subroutine for solidification convergence criteria. Note that the liquid fraction variation as function of temperature obeys fully to the lever rule in the range between the solidus and the liquidus. In addition, the graph shows clearly the fully liquid phase at higher temperature and the fully solid phase at lower temperature as it should be.

The implemented routine resolved the issue related to the bad convergence of latent heat resulting from insufficient number of iterations without over doing the calculation cost. Following this implementation, solidification calculation were more stable and closer to the physical phenomena observed in the experimental results.

II.2.2.4. Resolving of the unnatural displacement of partially solidified melt

The solidification module in Fluent, based on liquid fraction model, presented another challenging issue where the partially solidified cells can develop an important traveling velocity if not well configured. To account for solidification, the model treats the cells subject to solidification as a porous medium where porosity is equal to liquid fraction. A momentum

sink, given as a function of the liquid fraction, is used in the momentum equation to extinguish velocity when the liquid fraction equals 0. The momentum sink is given in the form:

$$S = \frac{(1 - f_L)^2}{(f_L^3 + \epsilon)} A_{mush} (\vec{v} - \vec{v_p}) \quad (2.19)[2]$$

Note that the sink is actually a continuous function of liquid fraction which means it varies continuously between a minimum and a maximum. Similar sink is used to damp turbulence if the turbulence model is activated.

A question arises about what happens to the velocity if the momentum sink is not strong enough to immobilize the partially solidified cells. In fact, using the default parameter of the solidification model f Fluent provided unrealistic results were consequent volume of partially solidified melt was in motion with the melt flow.

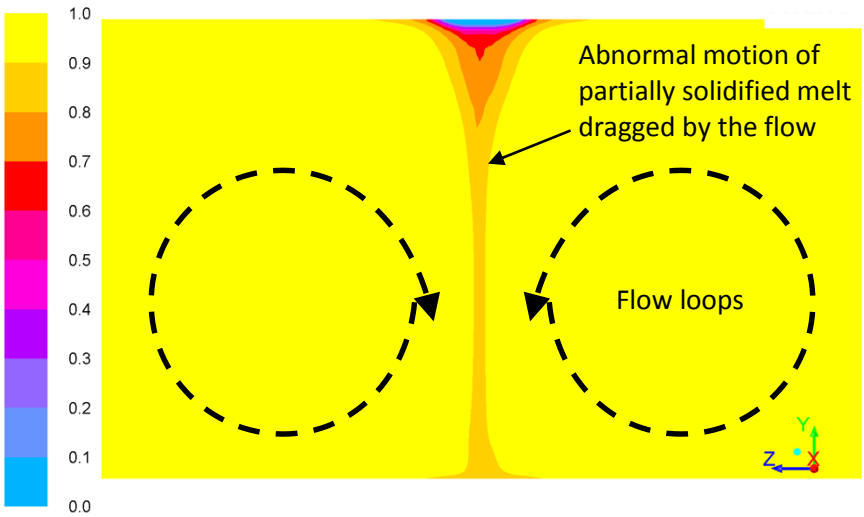

Figure 2.21. unrealistic motion of partially solidified melt into the deep silicon melt

The first calculation of solidification using default setting showed, that the liquid solid interface is not clearly delineated. The solid liquid interface was a band of 5 to 10 cells thick where the liquid fraction varies from 0 to 1. The partially solidified melt do not stay contained

in in the vicinity of the liquid/solid interface but gets carried away with the flow into the deep melt (Figure 2.21). Two major issues results from this numerical deficiency.

1. There is an unnatural energy transfer as latent heat in the melt.
2. The partially solidified melt in motion is slowing down the flow in the deep melt by its breaking momentum sink giving erroneous velocity field.

Fluent recommend the use of the mushy zone parameter to enhance the damping, while warning at the same time that higher values of mushy parameters may cause the solution to oscillate. This paradox needs another physical value in order to estimate the optimal mushy zone parameter. Equation2.19 is mostly numerical however its physical significance can be made clear if compared to the damping force in a fluid expressed in the form:

$$\boldsymbol{f_{damp} = \rho \frac{\partial \vec{v}}{\partial t}} \quad \textbf{(2.20)}$$

By equating equation 2.20 and the momentum sink in eq 2.19 we may write

$$\boldsymbol{\rho \frac{\partial\,(\vec{v} - \overrightarrow{v_p})}{\partial t} = \frac{(1 - f_L)^2}{({f_L}^3 + \epsilon)} A_{mush}\,(\vec{v} - \overrightarrow{v_p})} \quad \textbf{(2.21)}$$

A characteristic time can be deduced in order to qualify the required duration for the full damping to take place such as:

$$\boldsymbol{\tau = \frac{\rho}{\frac{(1 - f_L)^2}{({f_L}^3 + \epsilon)} A_{mush}}} \quad \textbf{(2.22)}$$

If we plot this characteristic time as a function of liquid fraction for different values of A_{mush} parameter, we obtain a base on which we can quantify the risk of diffusion of partially solidified melt according to the working parameters for each case. This will also help to choose the A_{mush} parameter without over doing it.

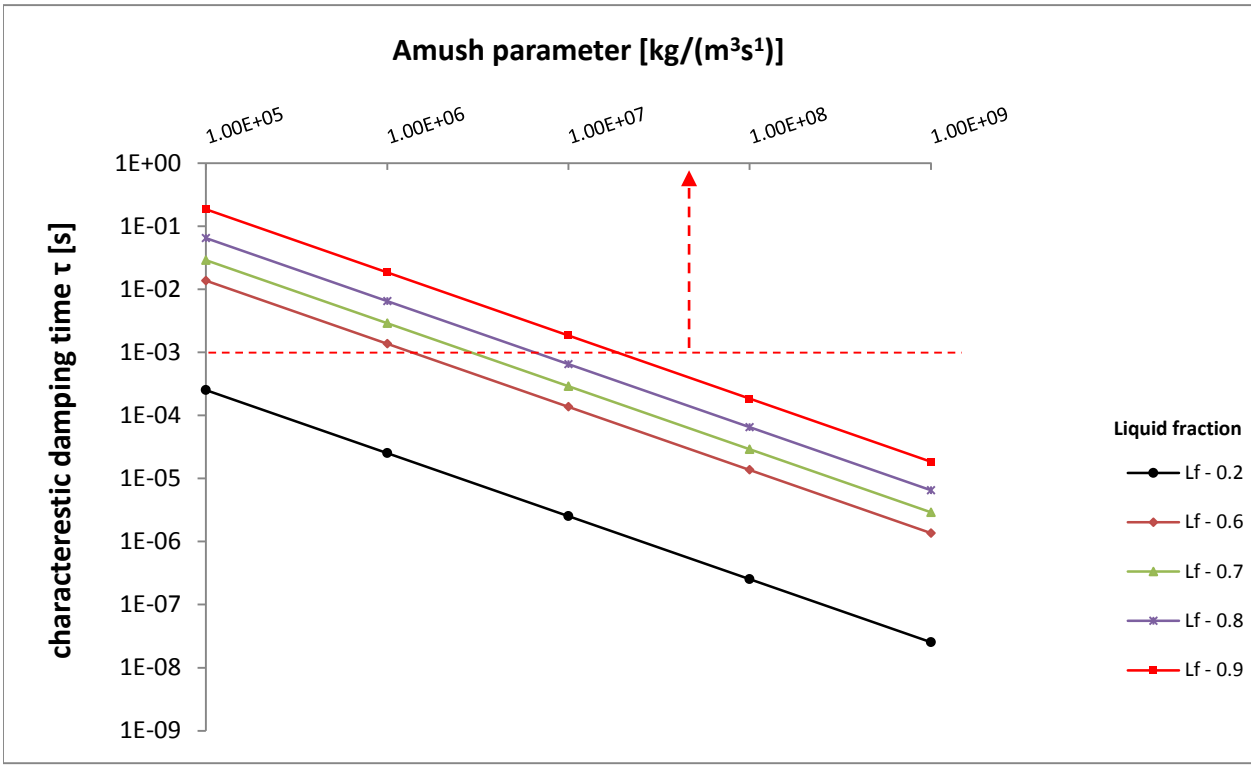

Figure 2.22. Variation of the damping time as a function of A_{mushy} parameter for different value of liquid fraction

Note that, for the default value of A_{mush} (lower than 10^6), cells with liquid fraction between 0.8 and 0.9 will travel for 0.02 s. if we project that on the average velocity of the melt in our configuration to get an order of magnitude of the traveling distance of the volume transported by a velocity of 10 mm/s, the partially solidified volume will travel 12 mm in 60 seconds supposing that it doesn't melt before; this risk is highly probable since we are working in a low thermal gradient melt delaying full remelting of the partially solidified volume.

The defined characteristic time provides information about the extent of motion due to melt flow for the partially solidified cells; a second criteria is needed to qualify the tolerable values of this characteristic time for a certain growth condition. We define a second condition stating that:

There will be no subsequent displacement of the partially solidified cells if the solidification interface is fast enough to engulf the full cell before it moves away from the solid liquid interface.

This assumption is quite robust, if verified, since fully solidified cells are not affected by the flow velocity. However, the approach requires a first approximated calculation to determine the order of magnitude of the interface velocity. If the solidification interface is not fast enough to engulf the volume before it diffuses into the melt, higher values of A_{mush} should be considered or smaller cell size.

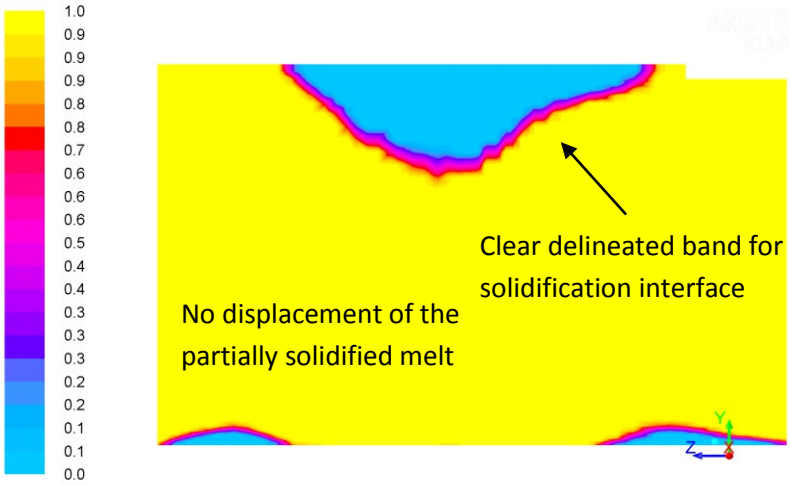

Figure 2.23. Clear mushy zone band on the vicinity of the solid/liquid interface with no displacement of the partially solidified melt.

By applying this analysis for our numerical case, the characteristic braking time τ was compared to the expected solidification front velocity to determine the required value A_{mush} for a given cell size. For a mesh with a cell size in the range of 2 to 4 mm and a solidification front speed in the range of 0.2 to 2 µm/s, the required characteristic damping time is in the order of 10^{-3} s. According to the projection of this value as a damping characteristic time in the graph of Figure 2.22, a value of A_{mush} between 10^7 and 10^8 will brake efficiently any cell with a liquid fraction less than or equal to 0.9. We observed that such value gave good

convergence for our case with no noticeable displacement of partially solidified cells and no solution oscillation.

Values of A_{mush} between 10^7 and 10^8 were found adequate for all the configurations in our investigation. We did not experience any extensive solution fluctuation at this point. The interface was defined by a clear band of more or less constant thickness and the partially solidified melt did not diffuse away from the liquid/solid interface as shown in Figure 2.23.

II.2.3. Calibration of thermal properties using experimental data

Calibration of thermal properties using experimental measurements is a common practice to adjust thermal properties used in the numerical simulation. Note that the thermal properties of interest in the present investigation are thermal conductivity and emissivity.

The calibration process for this investigation was based on the experimental readings of temperature in two thermocouples placed inside the top and the bottom heaters. These thermocouples are labeled as 1 and 3 in

Figure 2.7. As mentioned in the paragraph related to the same figure, these two particular thermocouples were chosen because they are well confined in an isothermal cavity inside the heater and therefore giving a punctual temperature of the heater.

II.2.3.1. Determination of the dominating thermal properties

The current simulation domain includes at least eight different materials increasing significantly the degree of freedom of the calibration process. A first screening of the heat transfer in the furnace shows that three main parts are controlling the heat losses from the furnace.

The calibration process can be approximated using only the dominating thermal properties in order to reduce the degree of freedom of the regulation process. A comparison of the effect of the major thermal properties of interest on the measured temperatures is then required.

A first screening of the heat fluxes exchange in the furnace presented in Figure 2.28 shows that the heat passing through the insulation casing, the soft felt insulation between the

bottom resistor and the bottom heat exchanger as well as the heat passing through the top cold heat sink represent 90 % of the total injected power. These three parts transmit most of the heat to the exterior.

The insulation casing has the highest integral heat loss while the bottom heat exchanger and the upper cold tube have the highest density of heat flux exchange. It is predictable then that the thermal conductivity of the insulation casing, surrounding the core of the furnace, and the thermal conductivity of the soft insulation felt, placed between the bottom resistor and the cold heat exchanger, have an important effect on the global and local distribution of temperature in the furnace.

Note that the cold heat sink in the upper part, used also as a radiation shield, receives almost all the heat by radiation and therefore is mostly dependent on emissivity values. Uncertainties and changes on values of emissivity of a well maintained copper surface are

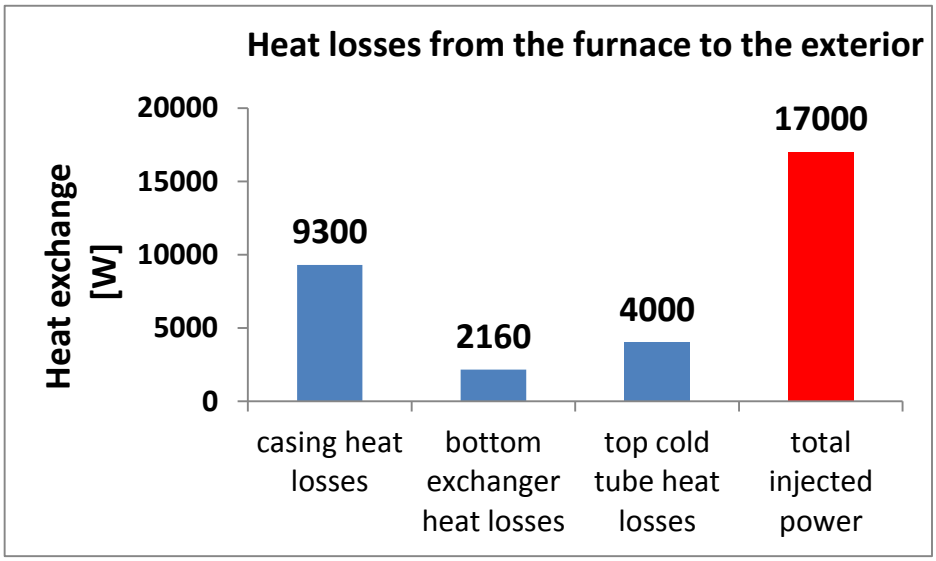

Figure 2.24. Major heat losses from the furnace estimated experimentally using the water cooling circuit compared to the total injected power.

less probable than those usually related to thermal conductivity and thus this thermal property is not of interest in the calibration process. Figure 2.25 shows the variation of the temperature in the top and lower heater elements according to the variation of the thermal

conductivity of the insulation casing. This numerical result was obtained by the variation of the insulation casing thermal conductivity.

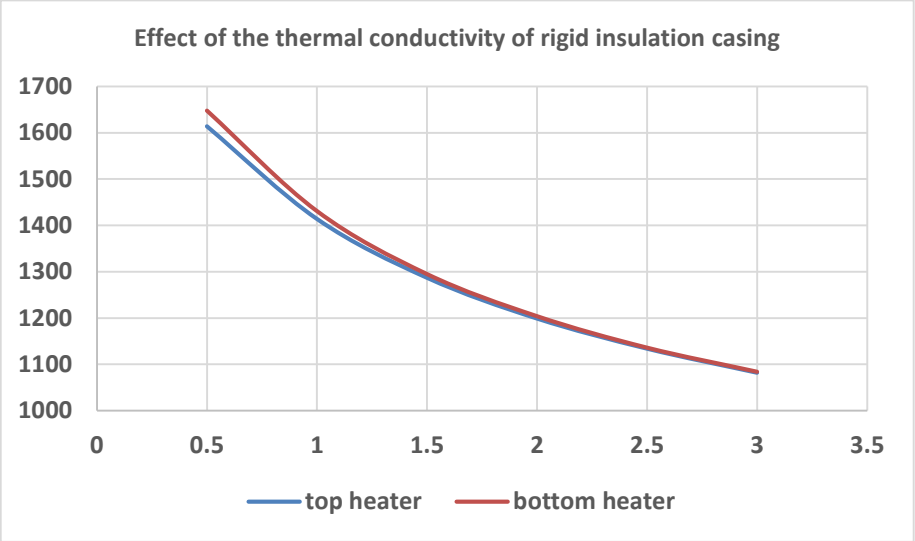

Figure 2.25. Temperature variation according to the change of the insulation casing thermal conductivity, the x axis is a factor of multiplication of the reference thermal conductivity.

Note that the increase of the thermal conductivity of the insulation casing by double will decrease the temperature, in both measurement points, by 200°K. The effect on the temperature in the two locations is similar qualitatively and quantitatively, which shows that the thermal conductivity of the insulation casing has a homogenous effect on the whole furnace. It is also an indication of the good thermal confinement provided by the present insulation casing.

Accordingly, the thermal conductivity of the insulation casing is the first dominating thermal property in the furnace. Notice that the calibration of the insulation casing is a challenging task since the material is susceptible to aging which leads to an important change of its thermal conductivity between working cycles.

The temperature variation in the top and bottom heaters according to the change of the soft felt insulation thermal conductivity, placed between the bottom heater and the bottom heat exchanger, is presented in Figure 2.26.

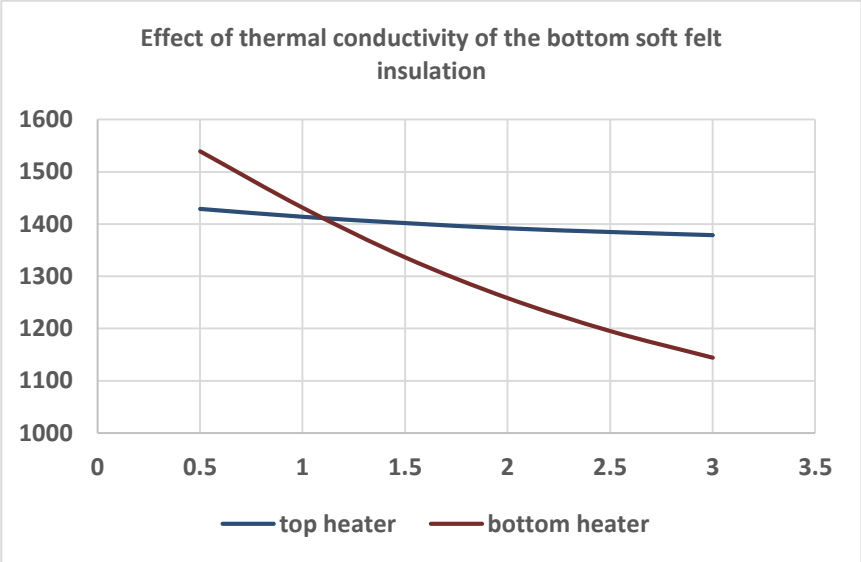

Figure 2.26. Temperature variation according to the change of the felt insulation thermal conductivity, the x axis is a factor of multiplication of the reference thermal conductivity.

The effect of the felt insulating power is localized on the bottom resistor while it has relatively less effect on the top resistor. The localized effect explains the high heat flux density loss passing through the soft felt insulation. The thermal conductivity of the soft felt insulation placed below the bottom resistor is the second major thermal property in the furnace.

A calibration of the numerical model can be done using the thermal conductivities of rigid insulation casing and the soft insulation felt under the bottom resistor. The temperature of the top heater will be used to adjust the thermal conductivity of the insulation casing while the temperature of the lower resistor will be used to calibrate the thermal conductivity of the soft felt insulation placed below the bottom resistor.

In addition to the effect of the discussed thermal conductivities; the temperature distribution in the furnace is function of the chosen properties and parameter on the boundary of the simulation domain. The exterior surface of the insulation casing is large which may lead to important integral heat flux and the specified convective heat transfer

coefficient, emissivity and the exterior convective steam temperature effects must be assessed as well.

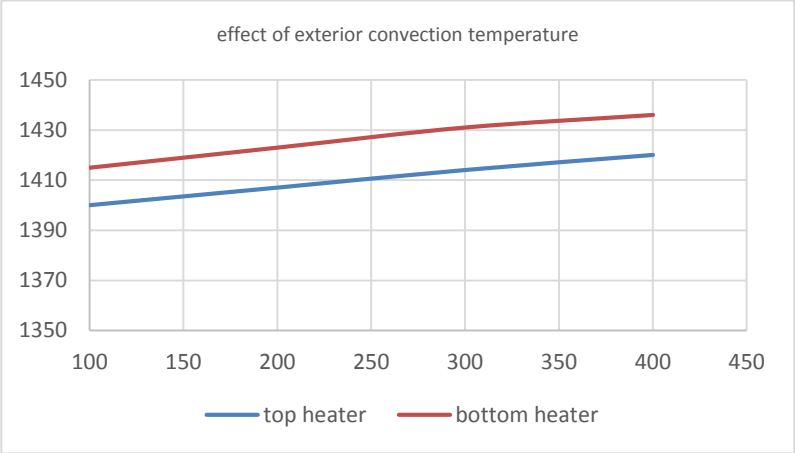

Figure 2.27. Temperature variation temperature according to the change of the applied steam temperature in the convection boundary.

Figure 2.27 shows the variation of the temperature in the top and bottom heaters according to the change of the exterior argon steam temperature. The chosen argon steam temperature in our simulation was 300°C. The influence of the variation of this temperature is quite low compared to the effect of the prior discussed thermal conductivities in the present configuration. A difference of 100°C in the temperature of the convective argon steam will induce about 10° difference in the measured temperature in the top and bottom heaters. Notice that the effect of this convective steam temperature on the furnace is homogenous, which is expected since it is dependent on the exterior wall of the insulation casing that have a homogenous effect on the furnace as described in Figure 2.27. The present work considered the convective heat transfer as equally distributed on the exterior wall of the simulation domain with no further investigation of inhomogeneous distribution of convective heat transfer on the exterior wall.

Following the prior listings, the used thermal properties in the numerical model were calibrated according to measurement of temperatures in the top and lower heater and the

approximated experimental measurements of heat flux losses from the insulation casing, the bottom heat exchanger and the top cold tube heat sink.

II.2.3.2. Validation of the thermal calibration

The thermal calibration process was done using two cases with different sets of power. The chosen two sets of power, presented in table 2, were chosen in order to be in the usual range of working temperatures between 900°C and 1430°C. The used values of temperatures in the calibration process are the temperatures of the top and bottom heaters.

The presented calibration values were obtained for a configuration with the top cold heat sink. The experimental measurement were taken during a crystal growth experiment.

Following the analysis presented in the prior paragraph, the temperature of the top heater was adjusted using the thermal conductivity of the rigid graphite insulation casing. As a consequence, the temperature of the lower heater changed as shown in Figure 2.25. The temperature of the bottom heater was then readjusted using the localized effect of the thermal conductivity of the soft insulation, as shown by graph in Figure 2.26, placed between the bottom heater and the bottom cold heat exchanger.

The adjusted value of thermal conductivity of rigid graphite insulation was 2.3 times the value given by the constructor. The adjusted value of thermal conductivity of soft insulation was 3 times the value given by the constructor.

Note that the resulting numerical values in the second calibration point have some differences compared to the measured values. The calculated temperature in the lower resistor has 7 to 10°C deviation while the calculated temperature in the top resistor had 19.2°C deviation from the measured temperature. The height deviation in the upper heater is suspected to be the result of non-contact between the different blocks around the top heater which is not accounted for in the numerical model. Regardless this deviation, the general tendency of temperature change was well reproduced by the numerical model which was sufficient to conduct the numerical analysis of the ongoing phenomena. No further refinement was required for the purpose of this investigation.

Table 2. 2 comparison of experimental measurements and numerical solution resulting from the calibration process.

	First calibration point		second calibration point	
	experimental	numerical	experimental	numerical
Power in the top heater	6500	6500	3300	3300
Power in the bottom heater	6920	6920	5700	5700
Power in the side heater	4071	4071	0	0
Temperature of top heater	1435	**1434.3**	925	**944.2**
Temperature of bottom heater	1468	**1468**	1000	**1007**

Note that the insulation is subject to aging during the run cycles which alters the thermal conductivity of the material. Heating effect, chemical reaction, vapor and fine partials deposit on the pores, are some of the probable phenomena that could be causing this variation. The recalibration process was performed again when required.

II.2.4. Influence of the three heaters on vertical and horizontal thermal gradients

II.2.4.1. Control of vertical and horizontal thermal gradients

According to the cubic geometry of the furnace and the disposition of the three heaters, the resulting thermal gradient for the present configuration can be approximated as the conjugate effect of a Horizontal thermal gradient and a vertical thermal gradient. A major interest rises at this point to understand the dependency of the vertical and horizontal thermal gradients on the heating power distribution in the furnace. Such understanding is required to control and predict the growth of the crystal.

Figure 2.28 shows the resulting vertical and horizontal thermal gradients in the melt as a function of power variation in the three heating elements.

The presented diagrams were obtained by adding a 1000W heating power distributed with different fractions between the three heating elements (top, bottom and side heaters). The

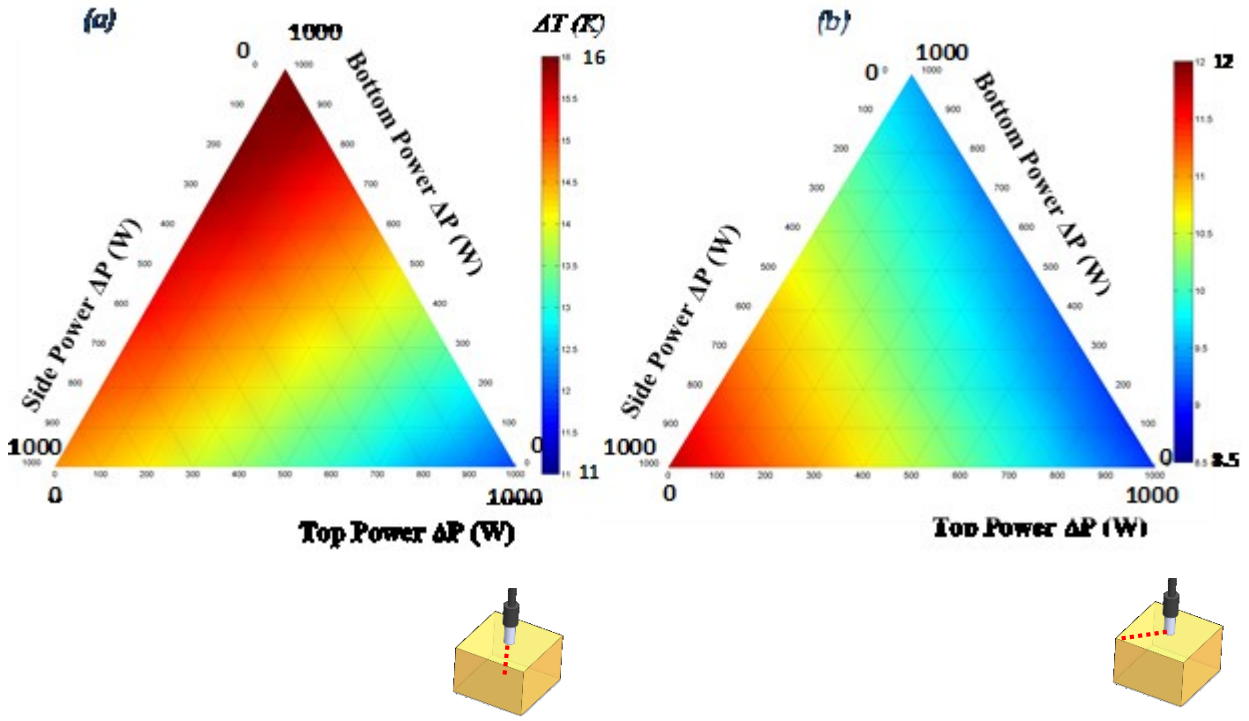

Figure 2.28. *(a) Vertical and (b) horizontal temperature differences in the silicon melt resulting from the increase of heating power by a total of 1000* W in the three heating elements. The starting point is a melt at dipping conditions. The ternary diagram shows ΔT according to different distributions of the additional 1000W between the three heating element of the furnace

calculation was a steady state resolution of energy equation without fluid mechanics. The initial state was a silicon charge were the contact spot with the seed is at 1414°C.

Figure 2.28.a shows that a maximum ΔT in the vertical direction can be obtained by adding 100 % of the 1000W in the lower resistor. On the other hand, the minimum vertical ΔT is obtained by injecting 100% of the 1000W in the top heater. The vertical thermal gradient can be controlled by the balance of power between the top and lower heaters.

Note that the increase of power in the side heater do not affect much the vertical temperature difference. The same vertical ΔT can be obtained, regardless the intensity of power in the side heater, if the fraction of power between the top and bottom heater is

preserved. This conclusion was only verified in the range of temperature close to seeding conditions.

The later statement correlates well with the conclusion described by Figure 2.25 where the insulation casing was found to affect the temperature variation in the top and bottom heater, more or less, with equal intensity.

Note that the lateral heater was added to act like an active insulation to diminish the side heat losses in conjunction with the insulation casing. As a consequence, the vertical ΔT obtained by the addition of 1000W in the side heater is close to the ΔT obtained by injecting 500W in the top heater and 500W in the bottom heater.

On the other hand, the maximum horizontal ΔT as shown in Figure 2.28 is obtained by putting 100% of the additional power in the lateral heater. Note how all the shades are, more or less, parallel to the base of the triangle facing the corner of 100% lateral power for all possible combinations of power distribution which means that horizontal ΔT on the surface of silicon is mainly controlled by the lateral heater regardless the distribution of power in the top and lower heater.

Providing that dipping conditions are maintained and the top center of the melt is at lower temperature compared to the edges, the change of vertical thermal gradient is mostly controlled by the top and bottom heaters while the change in the horizontal thermal gradient is mostly controlled by the power in the lateral heater. The increase of the vertical ΔT can be obtained by the increase of the power in the lower heater or the decrease of the power in the top heater. Note that it is possible to change the vertical ΔT, to some extent, while keeping the dipping zone at constant temperature by compensation of the power in the side heater since it affects homogenously the variation of top and bottom temperatures in the melt. It is possible to promote the vertical growth but at the expense to increase the horizontal thermal gradient.

II.2.4.2. Adjustment of the heating power to obtain dipping condition

The last paragraph showed that the current three heater configuration offers, to some extent, an independent control capability of the lateral and vertical temperature differences. The vertical ΔT is dependent on the power distribution in the top and bottom heater while the horizontal ΔT is dependent on the side heater. Based on this conclusion, an algorithm was proposed to find the right distribution of power in the three heating elements in order to obtain a melt at seeding state (Appendix 1).

The purpose of the algorithm is to find the set of power to obtain a melt where the seeding point is the cold spot close to the melting temperature and the edges are at higher temperature. To obtain a melt at seeding state in a configuration with three heating elements, three conditions can be proposed such as:

- The seeding point is slightly above the melting points (T_m + 2 K)
- The temperature difference along to the central vertical axis is 10K
- The temperature difference according to the diagonal line on the surface is 14K

This approach has the advantage to resolve the power distribution for a predefined vertical and horizontal ΔT. The algorithm requires the verification that the first spatial derivative of temperature is always positive from the center to the edges of the melt.

Note that the chosen ΔT are bounded by a specific spatial position which means that they do not guarantee that all the temperatures on the edges are above the melting point. An extra condition based on the minimum temperature on each wall to be above the melting point, can be added if required to adjust the power; however, the final resulting thermal gradients inside the melt will change as well.

The graph in Figure 2.29 shows the evolution of horizontal and vertical ΔT according to the adjustment of the heating power during the iterations of the regulation algorithm to obtain a melt at seeding state.

The algorithm calculation was started from the initial state described by the following heating powers:

Top power: 9340 W, bottom power: 2920 W, side power: 6672 W. and the resulting Seeding temperature was 1412.89 °C, with the following temperature differences ΔT_h = 16, ΔT_v = 9.

The specified variation of power in Figure 2.29 is taken according to these initial values of power. The seeding state calculated by the algorithm, in this case, is defined by the required temperature at the seeding spot, equal to 1414°C, and the vertical and horizontal thermal gradients equal to, respectively, 10k and 12K.

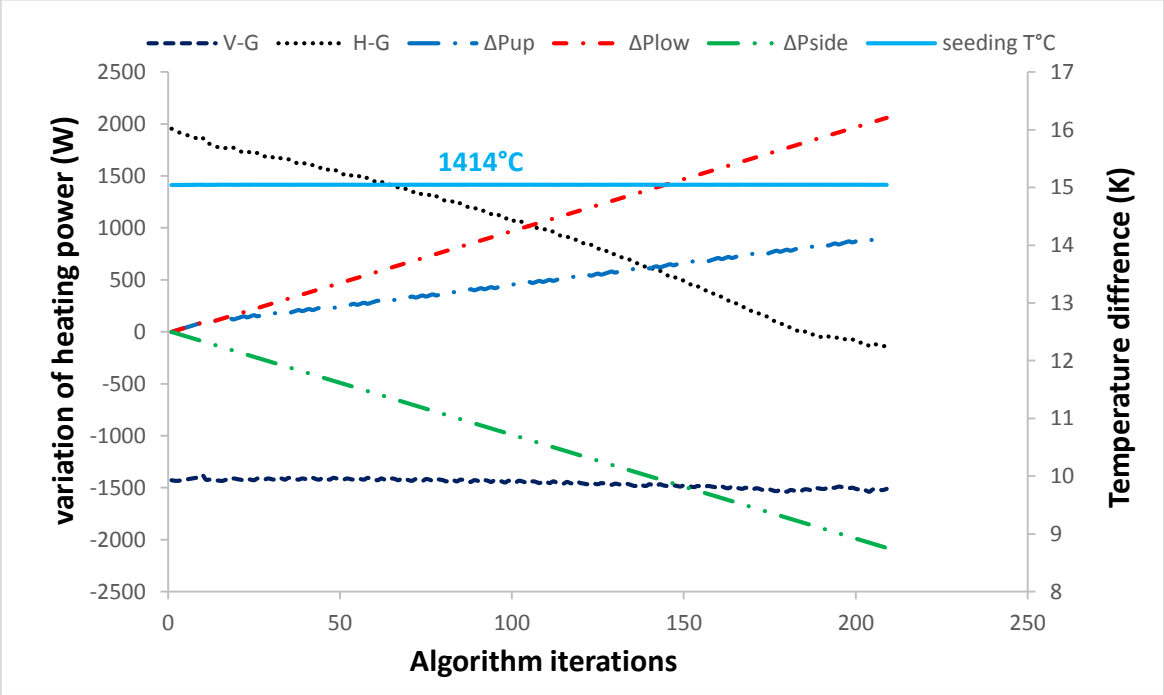

Figure 2.29. Finding the seeding state based on predefined conditions: T_{seed} =1414°C, ΔT_h = 12 ±1, ΔT_v = 10 ±1. (stationary calculation with melt flow in configuration with top cold heat sink)

The algorithm reaches a stable state around iteration 200. The algorithm converges back to the same stable solution regardless the initial starting power values. Note that T_{seed} = 1413.46°C and ΔT_v = 9.78 K, ΔT_h = 12.27 K are close to the desired values.

The algorithm is based on the analysis of the effect of power variation on vertical and horizontal thermal gradients presented in Figure 2.28. Its efficiency is dependent on cases where the working conditions are in a range of temperatures close to seeding state conditions.

Not all combination of vertical and horizontal thermal gradients are possible for the seeding state. The current results puts an interesting question on the limitation of the system especially the correlation between the vertical and horizontal growth. Further details will be discussed in the results chapter showing the maximum possible growth aspect ratio (vertical over horizontal) in the current configuration.

II.3. Conclusion of the second chapter:

A numerical model was constructed based on the geometry of the experimental furnace to sustain the development of the process. The 3D simulation domain included all major parts of the furnace core. The model did not use symmetry simplification since the melt flow and the crystal growth were found to be non-symmetric.

The calibration of the model using experimental data allowed satisfactory prediction of heat transfer by the numerical model. The numerical model included heat transfer, fluid dynamics in the melt and solidification.

Although the flow in our configuration is mainly laminar in transition to turbulent, a turbulent numerical model was required to obtain satisfactory convergence.

The growing crystal in the model was assumed to be totally immersed in the melt and the level of the free surface of the melt was assumed to be at fixed position during the full process. Analytical development was presented to validate both assumptions.

The modeling of solidification using the default native solidification liquid fraction model in Fluent suffered from the lack of a solidification convergence criteria in fluent software. Bad convergence of latent heat calculation and the displacement of the partially solidified melt were identified as the limiting problems. An implemented user defined subroutine as a

convergence criteria next to the determination of the proper operating A_{msuh} parameter enhanced the convergence and accuracy of the solidification simulation.

A first numerical investigation in a purely thermal diffusive regime showed that the vertical thermal gradient is mostly dependent on the distribution of power in the upper and bottom heater; while the horizontal thermal gradient is mostly dependent on the side heater.

An elaborated iterative algorithm based on three conditions related to the desired seeding state (temperature of the seeding point, vertical ΔT and horizontal ΔT) allowed the calculation of the required power distribution in the three heating elements. Furthermore, the proposed algorithm converged to a stable solution that is not necessarily in compliance with the desired conditions which indicates the limits of the present configuration. The later result shows that not all combination of vertical and horizontal thermal gradients are possible physical solutions for the seeding state. Nevertheless, the use of the iterative algorithm allowed the determination of the nearest possible solution.

The vertical temperature variation in the melt was mainly dependent on the distribution of power between the top and bottom heaters while the horizontal temperature variation was mainly dependent on the power in the side heater.

The numerical model was calibrated using experimental data. The full numerical model results will be presented in the next chapter including comparison between experimental and numerical results.

Chapter 3

III. Numerical results

The current chapter presents and discusses the results of the numerical model applied to the different developed configurations of the process. It describes each configuration by mean of calculated temperature distribution velocity profile and exchange of heat fluxes in order to:

1. *Identify the problems in each configuration.*
2. *Explain the required next step of the development.*
3. *Validate the proposed modification for development.*

The development of the current process of Kyropoulos for silicon included the testing of several configurations; each configuration was the outcome of fundamental and technical challenges that will be explained numerically.

The development of the process in this work can be summarized in three main configurations:

1. A starting configuration based on a reversed vertical gradient of directional solidification
2. Configuration with ceramic radiation shield to screen the seeding zone
3. Configuration with a top cooled heat sink to enhance heat extraction from the seed

Figure 3. 1 is a schematic representation of the main three tested configurations where Figure 3. 1.b shows the addition of the ceramic tube around the seeding shaft and Figure 3. 1.c shows the addition of a cold tube as a heat sink in the top area above the seeding zone.

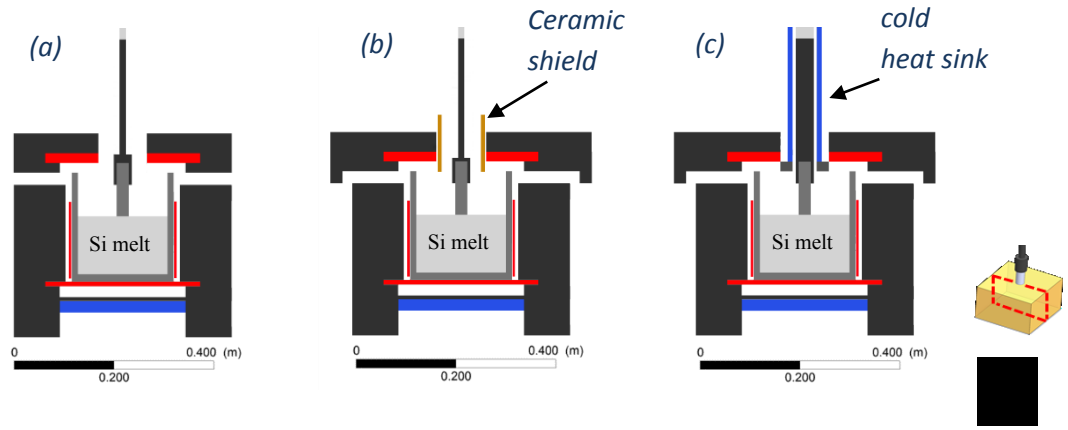

Figure 3. 1. Major resulting configurations during the development of the process.

III.1. Starting configuration

The starting configuration was designed based on a DS furnace using a square crucible with an inner horizontal cross section 185x185 mm. At first, the furnace was heated by a top and bottom heaters only. The distribution of power in the top and bottom heaters controlled the vertical thermal gradient intensity and direction to make the top part of the melt the cold zone.

A circular cut of 100mm diameter was done on the top part of the furnace (heating element and insulation) as a cold view, to augment locally radiative heat extraction from the central area around the seeding zone. The seeding graphite cane was expected to enhance local heat extraction from the seeding area by conduction. More details about this configuration are presented in chapter 2.

Numerical results showed that no growth from the seed was possible in the starting configuration. As shown in Figure 3. 2 the central area of the surface of the melt is the hot zone while the corners are at lower temperature. Any decrease of heating power in these conditions resulted in complete freeze of the surface.

The convection loops where in the reverse desired direction. Four loops formed in the melt, ascendant in the center and descendent in the corners. The ascendant flow loops in the center were bringing the hot melt from the bottom directly to the seeding zone.

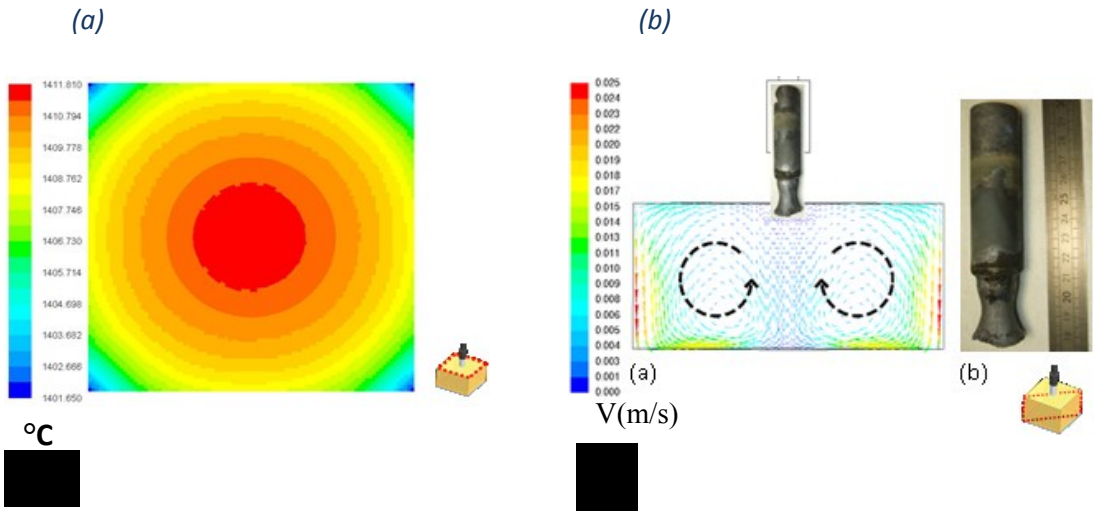

Figure 3. 2. Starting configuration, (a) temperature distribution on the surface of the melt, without flow (b) reversed flow loops with no possible growth from the seed.

Growth from the seed was not possible in this configuration. The starting configuration focused on the vertical thermal gradient without proper control of the horizontal one. As a consequence the following issues remained:

1. Although the top part of the furnace was adjusted to be generally at lower temperature compared to the bottom, there was no control over the horizontal thermal gradient.
2. The power distribution in the top and lower heaters do not effect much the horizontal thermal gradient.
3. The ascendant flow loops in the center of the melt are bringing heat to the seeding zone.
4. Heat extraction form the seed by conduction is low due to direct exposition of the seeding parts to the top heating element.

5. The radiative cooling coming from the top circular cut is not concentrated enough on the central area of the melt.

6. Due to the geometry of the furnace and the shadowing effect from the crucible walls, the central area of the melt surface receives more radiative heating from the top heater compared to the edges.

7. The silicon melt is losing most of the heat from the side walls complicating considerably the control of the horizontal thermal gradient.

The starting configuration is not flexible enough to control a proper growth from the seed. The horizontal gradient was not as required and neither was the melt flow direction. The central seeding zone was not the cold spot in the melt. In order to resolve these issues, modifications are required to:

- Reduce locally the heating of the central seeding zone in the melt
- Create a stable and continuous thermal gradient in the melt where the edges are at higher temperature and the center is at lower temperature. The melt flow should be decedent in the center and ascendant in the edges.

III.2. Configuration with ceramic radiation shield

III.2.1. General distribution of heat and melt velocity at seeding state

As presented earlier, Radiation heat transfer, especially on the top of the melt, participates greatly in the distribution and exchange of heat around the seeding zone. The seeding zone was receiving too much radiative heat from the top heating element and therefore keeping the seeding spot at higher temperature.

In order to cut the excessive radiative heating, a refractive ceramic tube, made of zirconia, was added on the top around the seeding elements as mentioned in the prior chapter (Figure2.3). Its role was to reduce the radiative heating of the seeding parts and the central surface of the melt. The 10 mm thick tube was 95mm in diameter gliding freely inside the top circular cut. The

used tube was 300 mm long which makes its bottom at about 100 mm above the surface of the melt. Although longer tube, with a bottom closer to the surface of the melt, would provide higher screening effect against radiation, the length of the tube was limited technically by the necessity to fill the crucible with silicon lumps op to the crucible top.

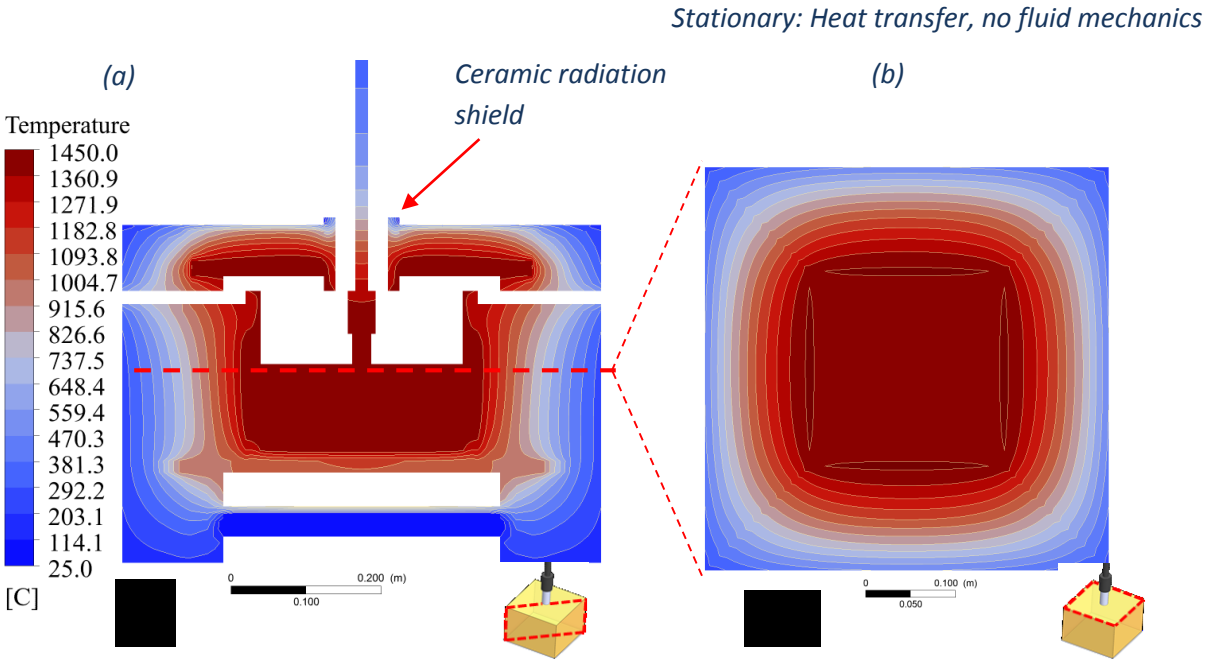

Figure 3. 3. Stationary heat transfer results showing temperature distribution for the whole furnace on (a) a vertical diagonal cross section and (b) a horizontal cross section at the level of the melt surface. (Heat power: Top 5300W, bottom 3500W, side 1500W)

Note that the bottom of the radiation shield is at the same level with the top of the crucible in order to allow the filling of the crucible with silicon lumps. The thermal confinement provided by the added radiation shield is noticeable by the increase of the temperature in the upper heater for comparable injected power. On a general scale of the furnace, most of the heat was lost from the side insulation casing

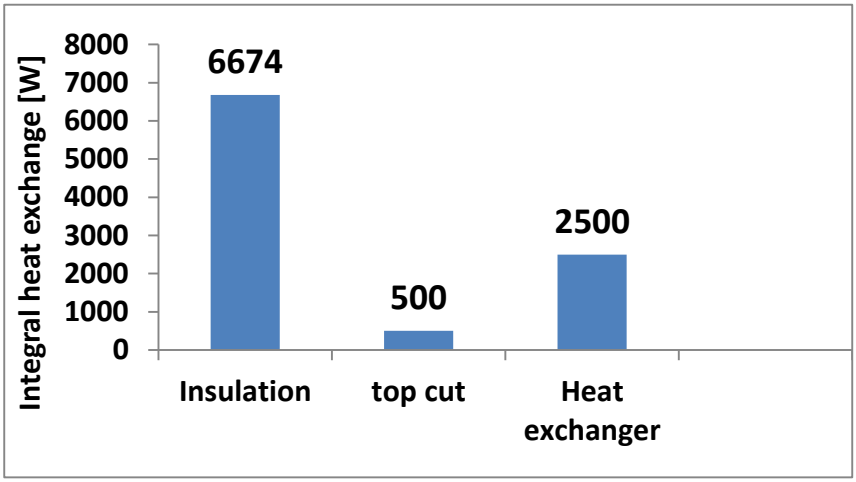

Figure 3. 4**.** Integral Heat loss from the furnace to the cold heat sinks and to the exterior. (Heat power: Top 2000W, bottom 4500W, side 3700W)

Figure 3. 4 shows that the insulation casing evacuates most of the heat in the furnace. The ceramic tube focuses heat dissipated from the top cut, around the seeding which results also in a lower heat dissipation from the top cut compared to the starting configuration. In conjunction with the radiation shield, the side heater was adjusted to reduce the heat losses from the side walls of the crucible.

Figure 3. 5, shows the integral heat flux exchange around the silicon melt. The heat balance in the close volume of silicon is not precisely null due to the transient nature of the calculation; the melt is not yet at thermal equilibrium state. Note that the heat out is slightly higher than the heat in since the silicon melt was cooled down to initiate the solidification process.

The incoming side heat from crucible walls is required to prevent any solidification from the crucible side walls. The heat extracted from the bottom decreases the temperature of the global melt while the heat extracted from the seed and the free surface stabilizes the cold spot at the center of seeding spot.

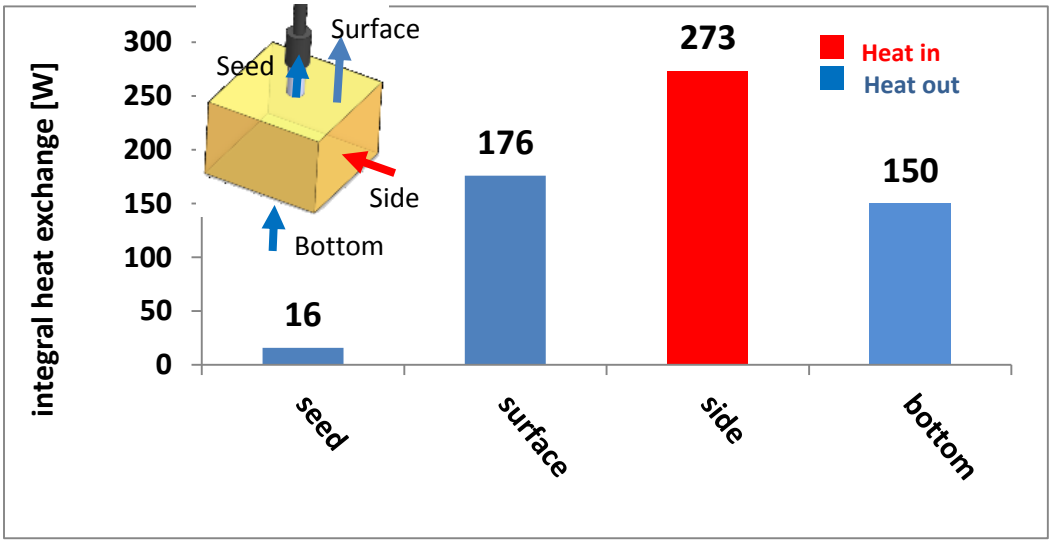

Figure 3. 5**.** Integral heat exchange from different surfaces limiting the silicon melt. (Heat power: Top 2000W, bottom 4500W, side 3700W)

Figure 3. 7.b shows the corresponding melt state. Note that the melt beneath the seed is the cold spot as required while the side edges are at higher temperature even in the simulation case without fluid dynamics (Figure 3. 7.a). Four flow loops can be observed in the melt (Figure 3. 6). The four loops are clearly shaped by the four corners of the square crucible. The flow loops are decedent in the center and ascendant in the corners which is in the desired flow direction. Note that the melt flow is a four symmetry case. This transient flow solution was tested to be stable after 10 min of real flow time.

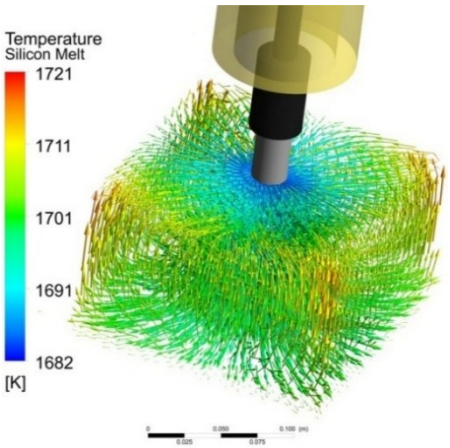

Figure 3. 6**.** Isometric view of the melt view of velocity vectors colored by temperature

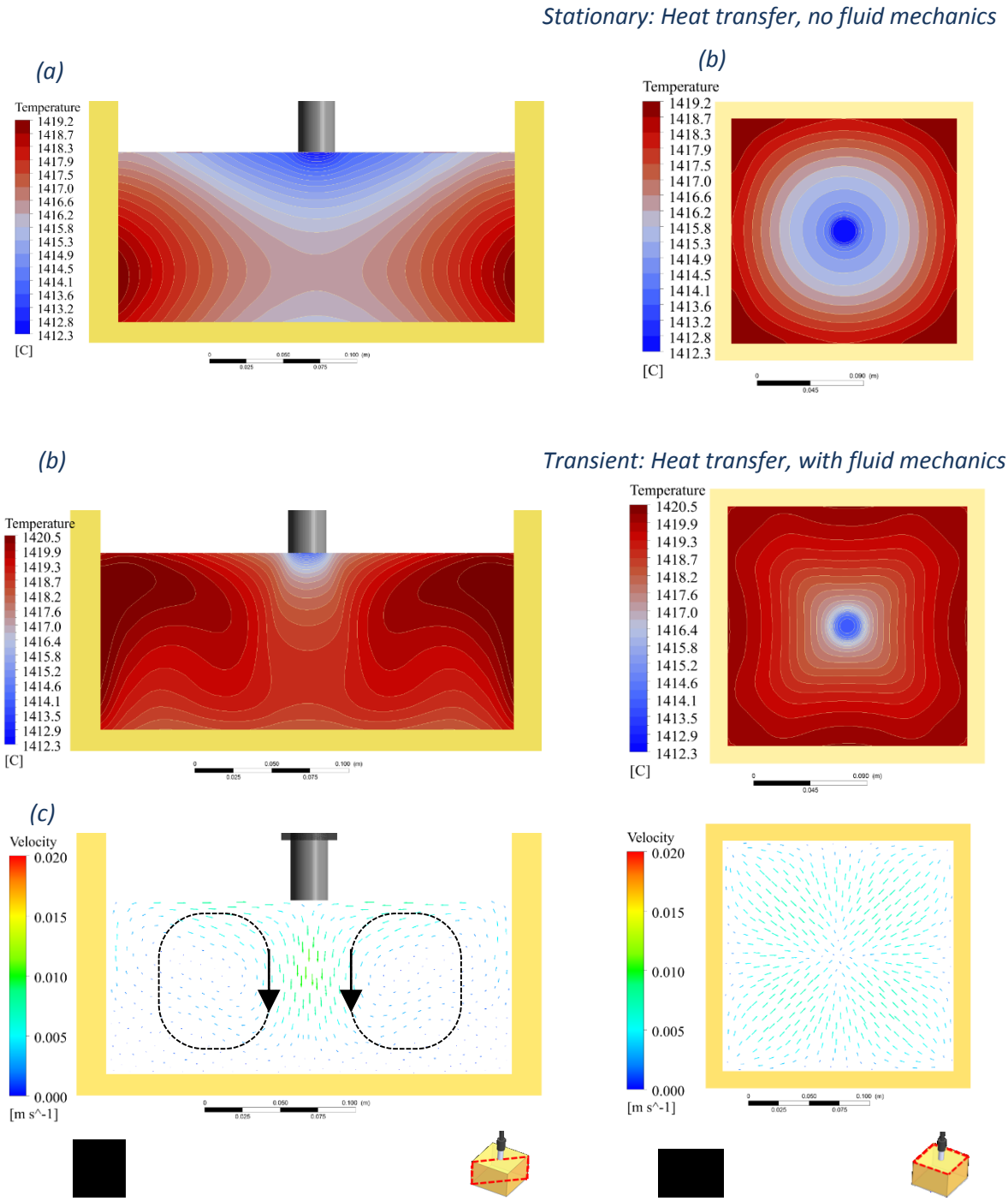

Figure 3. 7**.** Temperature distribution and velocity profile on a vertical diagonal cross section and on the surface of the silicon melt for a stationary and transient calculations. (Heat power: Top 5300W, bottom 3500W, side 3500W)

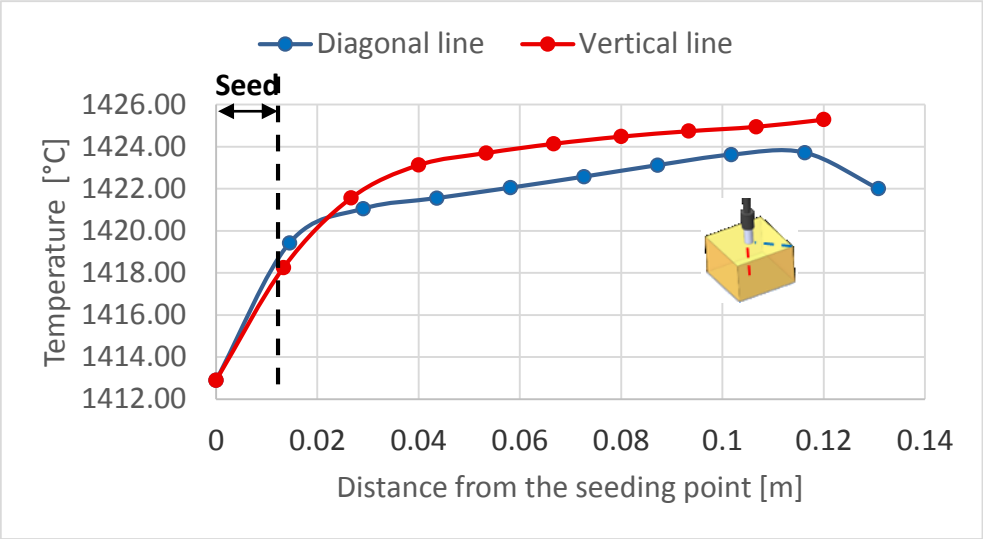

Figure 3. 8**.** Temperature distribution in a diagonal horizontal line and a central vertical line in the silicon melt for a stationary heat transfer with no fluid mechanics.

The thermal gradient is higher directly beneath the seed compared to the rest of the melt (Figure 3. 8). The higher thermal gradient in the vicinity of the seed, in both vertical and horizontal direction is, in part, due to a higher heat extraction density from the seed even though the integral heat extraction from the seed is quiet low. Note that this high thermal gradient beneath the seed is also enhanced by the consequent slowdown of the melt in the top center before it breaks downward into the deep melt. Because of the slow melt flow in the top center, the effect of the local cooling is more persistent since the slow melt do not homogenize efficiently the local temperature distribution.

The second derivative of the spatial variation of temperature do not vary much except in a local area between the seed and the deep melt. Such feature requires attention during the growth since it may rise the density of defects in this zone. Note that the melt has a small thermal gradient; which is coherent with the high conductivity of liquid silicon and the thermal homogenization by convection. Most of the temperature variation along the diagonal line at the surface is located beneath the seed with a thermal gradient equal to 4 K/cm, while the thermal gradient in the deep melt, far from the vicinity of the seed, is about 0.33 K/cm.

III.2.2. Solidification process

According to the later discussions, the central zone is at lower temperature and growth form the seed should be possible without contact with the crucible, provided that the configuration maintains the edges at higher temperature during solidification. Four main questions needs to be investigated in order to determine the potential of this configuration for the growth of silicon crystals inside the melt:

1. Demonstrate the possibility of crystal enlargement form the seed.
2. Investigate the maximum horizontal crystal enlargement.
3. Investigate the maximum vertical crystal enlargement.
4. Control the shape of the final ingot to obtain, hopefully, a square ingot using either:
    a. thermal diffusion from the crucible wall
    b. or, melt convection effect on the solid/liquid interface

The presented transient solution in Figure 3. 7 was used as an initial seeding state to start the growth process. The cooling procedure (Figure 3. 9) for the growth was divided into two parts. The first part of the growth was intended to demonstrate the possibility of crystal enlargement from the seed as well as the maximum horizontal growth controlled by thermal diffusion from the crucible, while the second part investigated the maximum vertical growth and the control of the ingot shape by convection.

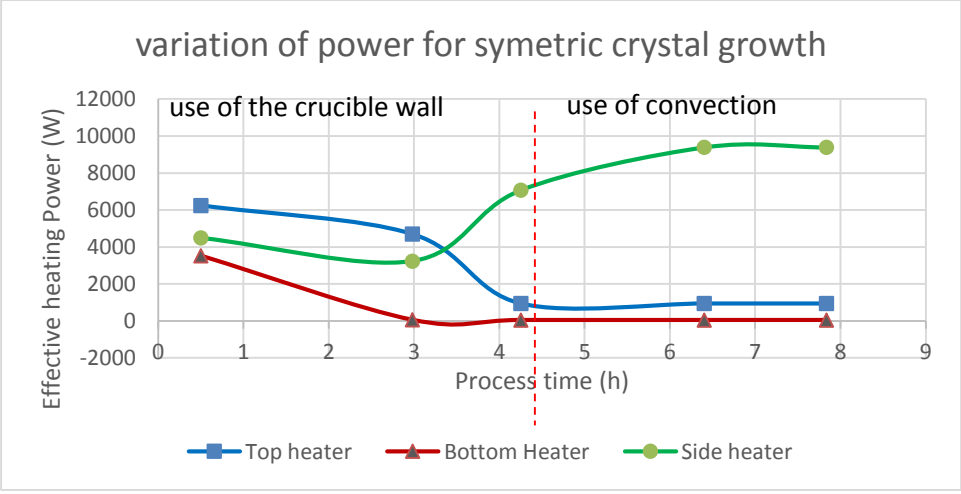

Figure 3. 9. Power variation used for the growth process

Figure 3. 9 describes the power decrease in the three heaters during the full growth process. The first stage of the growth is maintained by a main decrease of the lower heater until it reaches its minimum. The seed was rotated continuously at 15 rpm and stopped when the crystal reaches a diameter of 100 mm. when the lower power is decreased to its minimum, the upper power is decreased to maintain the growth in the vertical direction. The lateral heater is incremented continuously during the process whenever the growing crystal edge are too close to the crucible wall (10 mm distance).

The following results present the progression of the growth in the two steps process. Each step is described by mean of crystal shape at different time steps in order to see the progression of the solidification interface horizontally and vertically. In the first step, the crystal shape will mainly be controlled by thermal diffusion, while in the second step, the crystal shape will mainly be controlled by convection.

III.2.2.1. Control of the ingot shape using thermal diffusion from the crucible wall

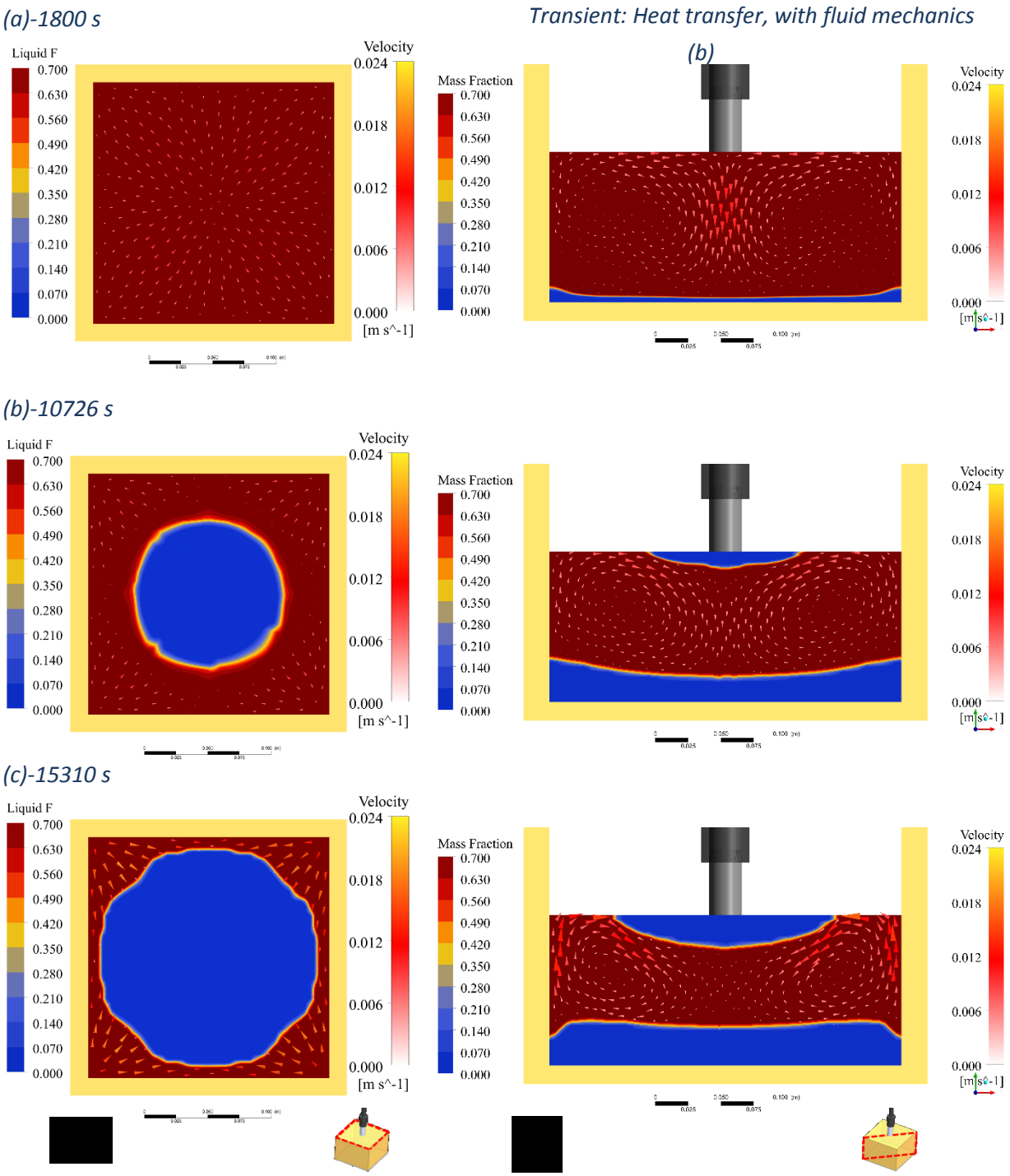

Figure 3. 10. Resulting crystal growth from the first stage of the growth described in Figure 3. 10. Shape of the crystal viewed in top and diagonal view next to convection at different time steps of the process

Figure 3. 10 presents the first step of the growth. The crystal grows from the seed and inside the melt. Note that the consequent decrease of power in the lower heater resulted in local solidification at the bottom of the crucible (Figure 3. 10.a). The same decrease of power initiated as well the growth from the seed. At this stage, the crystal is still rotating. Note that the shape of the crystal is circular at midrange of the growth (Figure 3. 10.b). This correlate to some extend with Figure 3. 7.b where the isothermal lines have the tendency to be circular at midrange of the horizontal distance. The homogenization provided by the rotation is also helping to keep the crystal in a circular shape. This position is also where the rotation have been stopped.

At about 50 mm of radius growth from the center, the rotation was stopped. The crystal continued to grow towards the crucible wall where the effect of the diffusive thermal layer of the crucible wall was higher. Note that the median four points at the middle of the four crucible sides are subject to lower melt flow compared to the stronger flow coming from the corners. The ingot continuous to grow towards the mid walls until it reaches a minimum distance of 10 mm between the crystal and the crucible. The later safe distance of 10 mm was maintained by controlled increase of the lateral heater.

Note how the edge of the crystal was strongly affected by the shape of the crucible wall as it comes closer (Figure 3. 14.c). The ingot shape is taking the shape of the square crucible without any solid contact. Because of the remaining convection in the corners, the square shape of the ingot could not be completed. The resulting hot melt flow in the corners was sustained by the increase of the lateral heater; this hot melt flow kept pushing the facing side of the crystal away from the corners. The final resulting ingot has a hexagonal shape rather than square.

The vertical growth is significantly lower than the horizontal growth. Note that, in both time steps presented in Figure 3. 10.b & c, the crystal has a flat bun shape with a growth aspect ratio horizontal / vertical close to 6.

Note, in Figure 3. 10.c, the localized remelting effect of the solidified silicon layer in the bottom of the crucible due to the increase of the lateral heater.

The curves in Figure 3. 11 & Figure 3. 12 displays the temperature and the liquid fraction along the horizontal and vertical direction in the melt and the crystal at different time steps starting from melted state. The variation of temperature inside the crystal has a low curvature in practically all time steps. Note that the vertical thermal gradient is much higher yet more constant. On the other hand, the horizontal thermal gradient have small perturbation mainly due to perturbation of radiation cooling on the top.

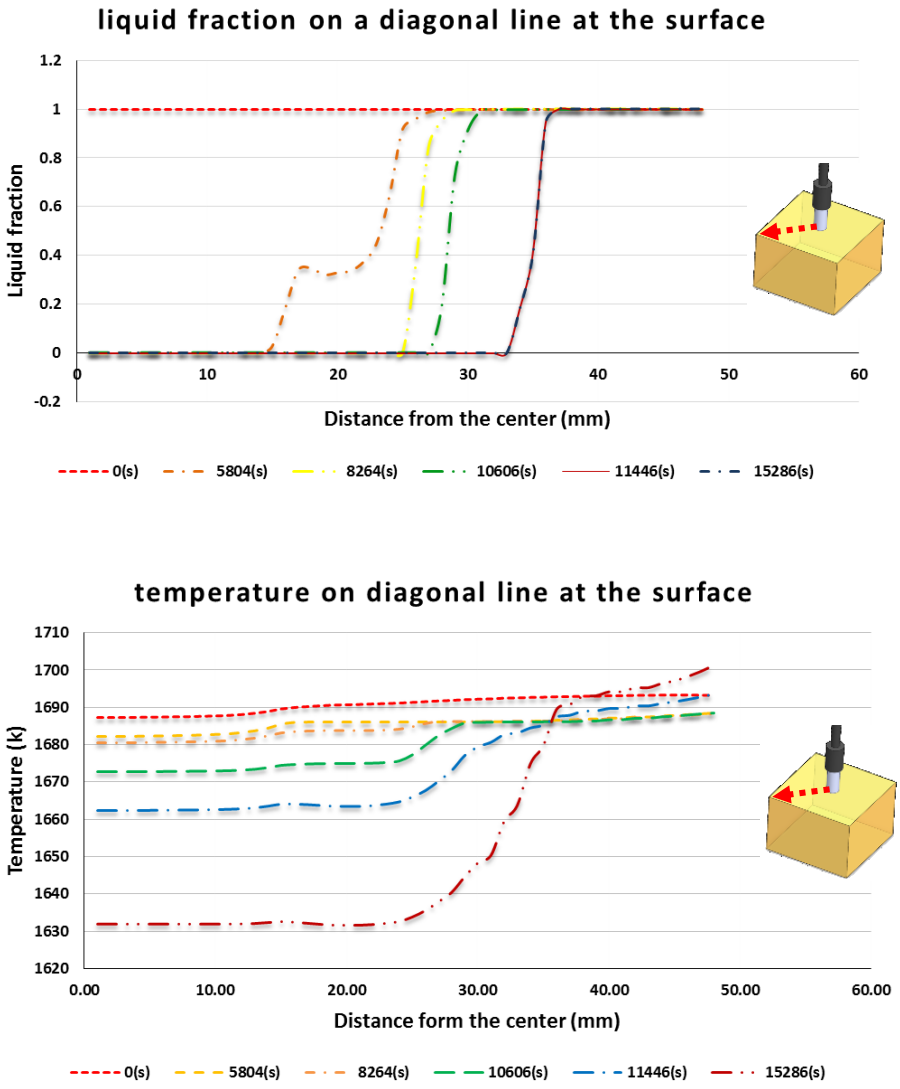

Figure 3. 11. Crystal growth evolution through time by mean of liquid fraction and temperature along a diagonal horizontal line on the surface of silicon.

The curvature of the thermal gradient gets higher next to the crystal edges. Lower thermal conductivity of solid silicon compared to liquid state promotes this effect. A melt at lower temperature decreases the curvature of the thermal gradient in the solidification interface zone.

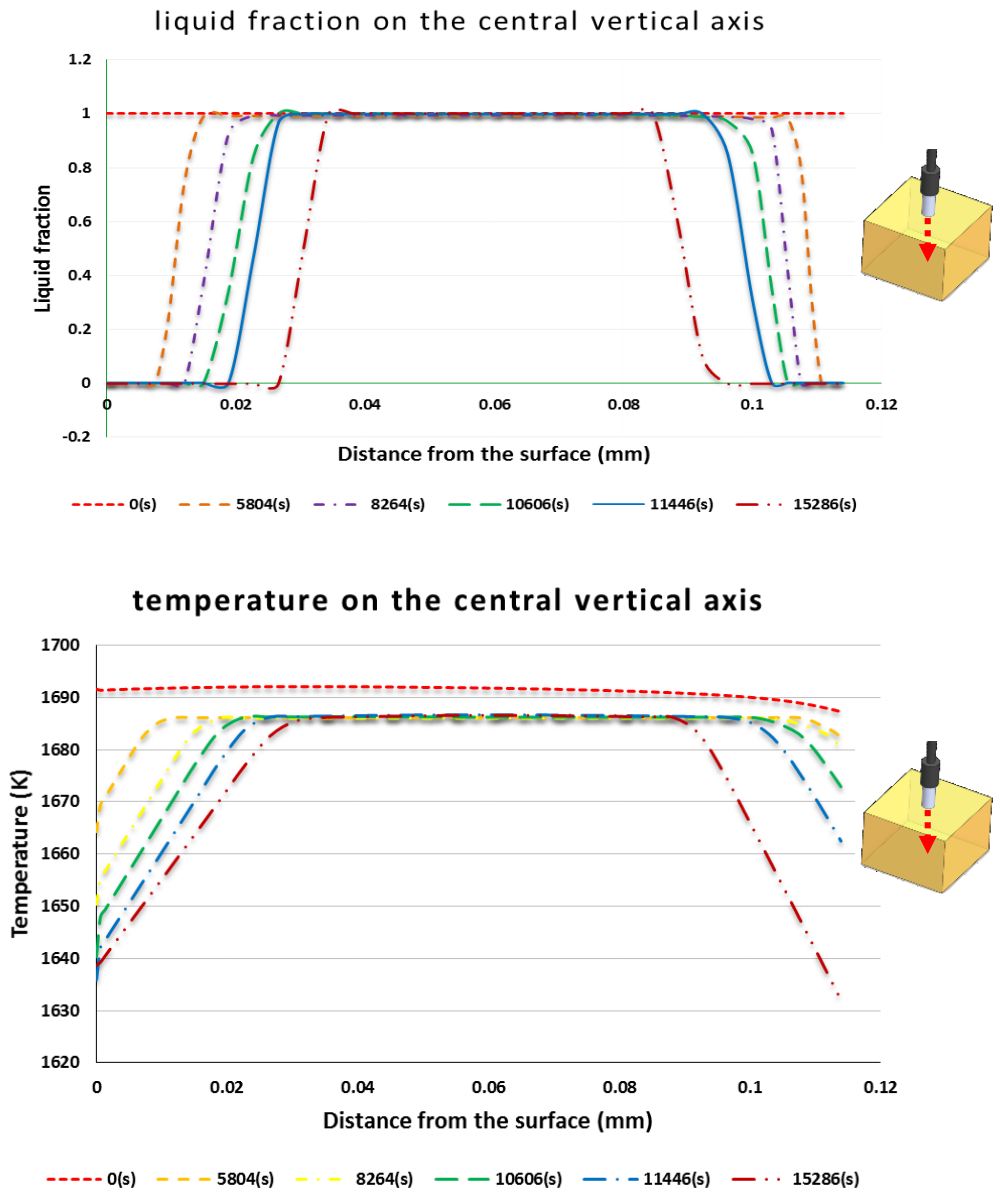

Figure 3. 12. Crystal growth evolution through time by mean of liquid fraction and temperature along a vertical central line in the silicon charge.

Figure 3. 13 shows clearly the increase of the horizontal flow intensity in the corners for advance time steps at the later stages of the process where the lateral heater is high. The velocity in the vertical direction follows a predictable evolution where the flow intensity decreases continuously with the decrease of the lower heater power due to the effect of the crystal. Such effect is beneficial, on a thermal point of view, since it cools down even more the central area promoting the vertical growth.

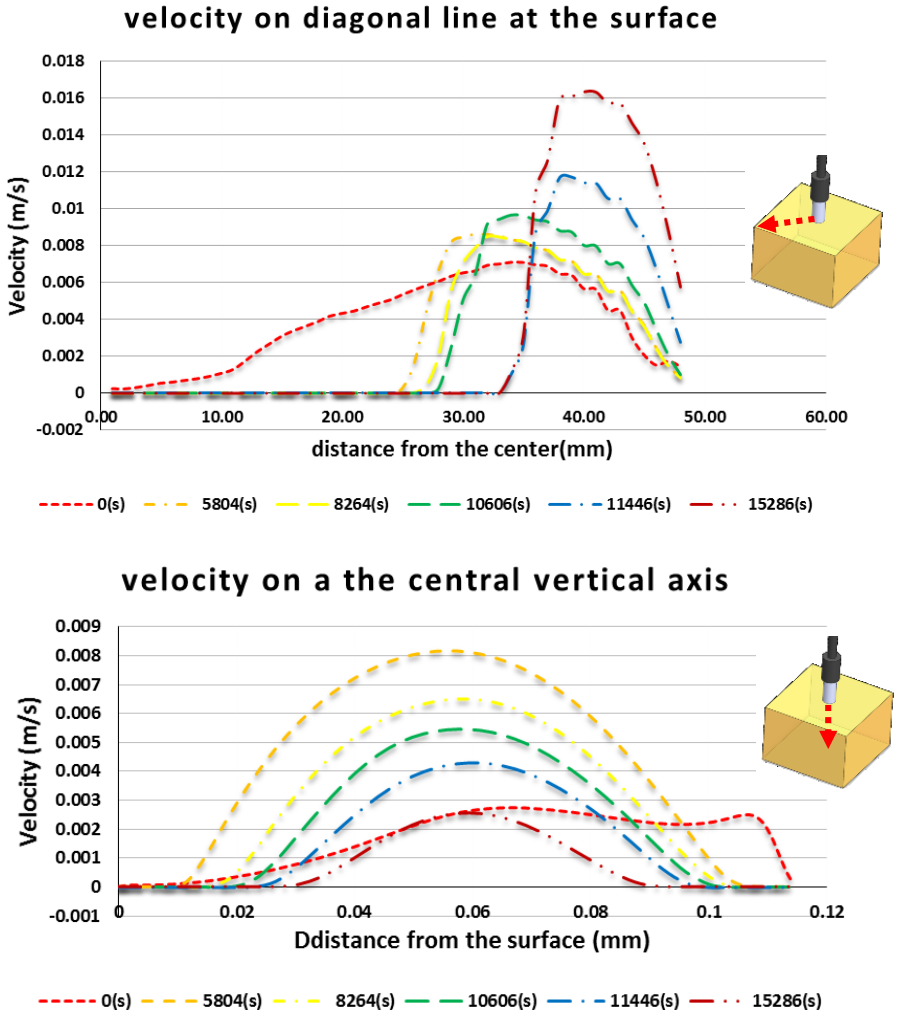

Figure 3. 13. Melt flow velocity evolution through time during solidification along a diagonal horizontal line and the vertical central axis.

For this part of the solidification process, the growth from the seed is consistent and unconfined. The obtained ingot is large covering most of the horizontal area of the crucible. The ingot has a flat shape aspect ratio with a growth aspect ratio vertical/horizontal equal to 3/10. The result shows that the ingot inherits the form of the crucible with thermal diffusion. It is possible to control the ingot shape using thermal diffusion from the crucible wall without solid contact.

The making of complete square shape in these conditions is not possible due to the concentrated heating in the corners. A non-uniform injection of power in the side heater is required to decrease locally the temperature of the corners.

III.2.2.2. Control of the ingot shape using thermal diffusion from the crucible wall

The second stage of the investigated growth starts where we left in the first stage using the prior grown large ingot. The following approach aims to investigate the possibility to obtain a square shape of the ingot using the melt flow convection. It is clear that the four corners of the crucible are a strong feature shaping deeply the flow pattern of the melt into four loops. In the last phase of the growth, the flow coming from the corners stopped the growth of the ingot from completing the desired full square shape which means that the flow is strongly reshaping the solidification interface.

Provided that the four flow loops are generated and guided by the four corners of the square crucible, it should be possible to project this on the shape of the final ingot. A square horizontal cross section can be obtained where each face of the ingot is facing one corner. The obtained square ingot is basically rotated 45° around the vertical axis compared to the crucible (Figure 3. 14.c).

Note that the continuous increase of the lateral heater empowers the convection loops coming from the corners which improves the square shape of the ingot. Note also that the largest possible square inside the ingot will generate less than 20% of cut loss.

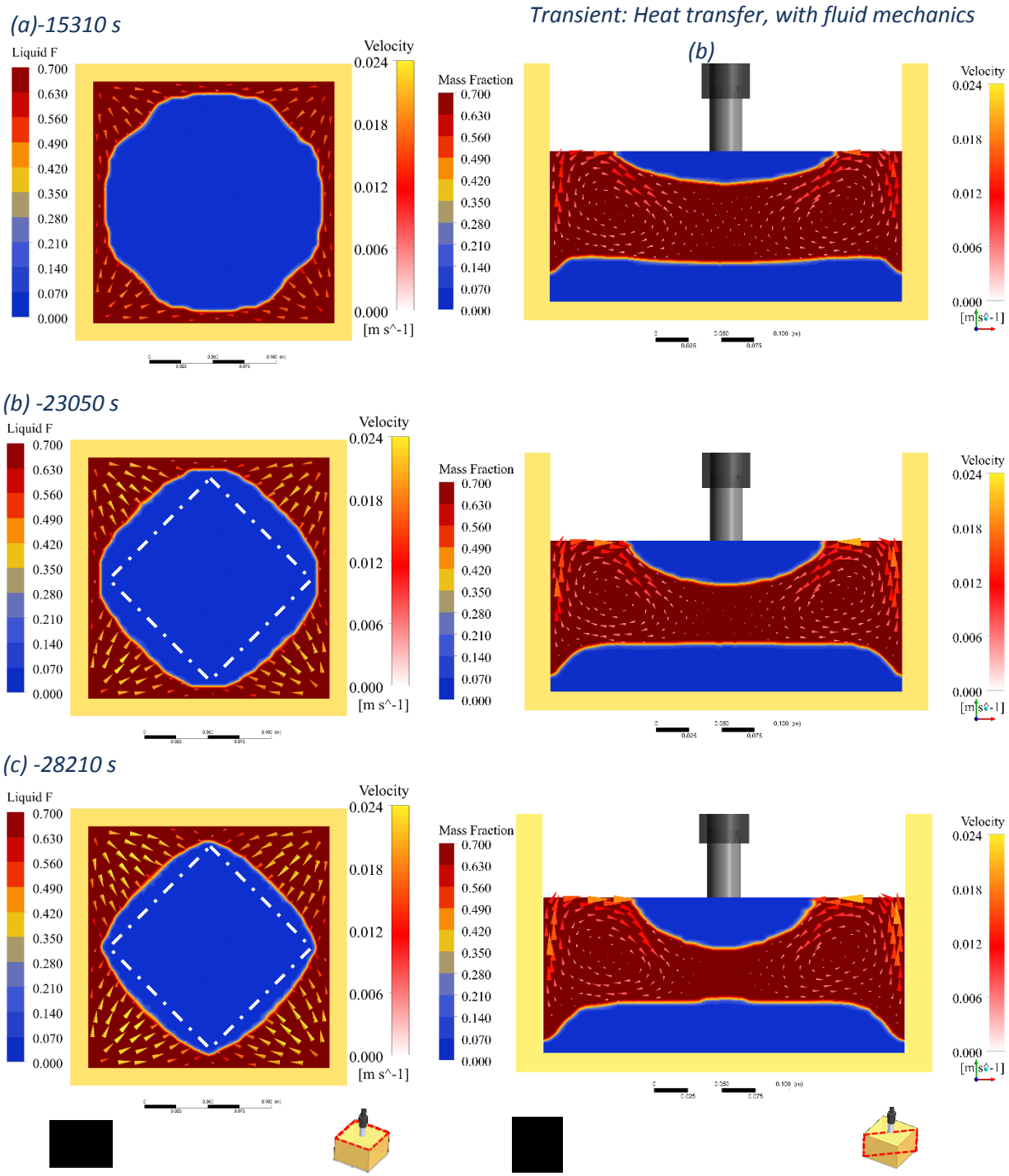

Figure 3. 14**.** Temperature distribution and velocity profile on a vertical diagonal cross section and on the surface of the silicon melt for a stationary and transient calculations. (Heat power: Top 5300W, bottom 3500W, side 1500W)

At the beginning of this stage of growth (Figure 3. 9) the lower heater was almost at its minimum value. The upper heater continued to be decreased to compensate the extraction of

heat coming from the rising lateral heater (Figure 3. 9). As a consequence, the melt flow in the corners was stronger retracting the four edges of the ingot. The final resulting shape of the ingot had a square horizontal shape rotated 45° around the vertical axis (Figure 3. 13.b).

The increase of the flow intensity to improve the square shape of the ingot reduces relatively the horizontal size of the ingot covering 60% of the crucible area, however, note that the vertical growth is higher due the increase of heat extraction from the top of the crystal giving a growth aspect ratio of vertical/horizontal equal to 3/5.

Similar to the last stage of the growth, the bottom side of the ingot is also a bun shape with more vertical growth in the center.

It is clear that the condition of noncontact with the crucible results in a bun shape growth, which is predictable since the heat is coming from the sides and extracted from the top surface.

.

III.3. Configuration with cold tube heat sink

In the later developed configuration with a ceramic radiation shield, successful crystal growth was possible. The horizontal growth was consequent covering up to 75% of the crucible at the surface without contact with the crucible walls. However, the vertical growth was comparably less.

The improvement of the vertical growth is mostly dependent on the heat extraction from the top of the crystal. The following development aims to improve heat extraction from the top surface of the crystal and from the seed.

The following section will present the numerical results of a reference case of study of the new configuration with cold heat sink. Further details on a construction point of view are presented in the last chapter in Figure 2.6. The present configuration is an advanced stage of the process development where crystal growth was proven to be possible numerically and experimentally. The cold copper tube was added around the seeding parts to enhance the heat

extraction from the seed (Figure 3. 15). The tube was also intended to cool the top surface of the melt around the seeding zone by radiation. The added tube provided a protective screen effect around the top part of the seed holder against the top heater. Figure 3. 15 shows the simulation domain as well as the main boundary conditions. The configuration includes two main cold heat sinks inside the simulation domain: the cold tube on the top and the heat exchanger in the bottom. There temperature was considered constant and close to ambient during the whole process.

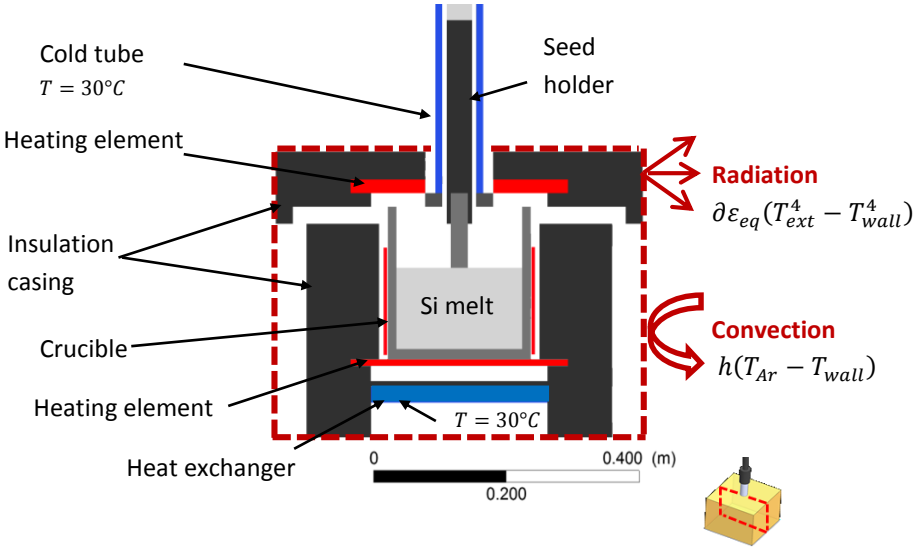

Figure 3. 15. Median cross section view, parallel to the crucible wall, of the simulation domain for the configuration with cold tube showing the major boundary conditions and the cold heat sinks

The exterior walls of the simulation domain had a mixed boundary condition of convection and radiation. More details about the applied boundary conditions at the exterior walls of the simulation domain can be found in chapter 2.

III.3.1. Simulation approach

A first part of the numerical investigation was based on the stationary resolution of the energy equation alone, to evaluate the heat transfer in the whole furnace including conduction and radiation in order to assess the total power distribution and the major heat fluxes in the furnace.

In a second part, transient calculation of fluid dynamics effect was added for a more precise temperature distribution in the silicon melt to reach a dipping state where the seeding point on the surface of the melt is two degrees above silicon melting point. The dipping state was obtained used the algorithm described in chapter 2 using the following three conditions:

1. The seeding point is about 2 K above the melting point
2. The vertical ΔT is 10K (according to the vertical central line)
3. The horizontal ΔT is 12K (according to a diagonal line on the melt surface)

The transient calculation simulated 10 min of real time process. The solution of temperature and velocity was stable.

III.3.1.1. Stationary calculation of heat transfer without fluid dynamics

The following results were obtained by the resolution of energy equation without fluid dynamics. The isothermal state was obtained using the algorithm described in chapter 2 based on the desired seeding point temperature close to 1414°C, as well as the vertical and the horizontal thermal gradients equal to 2K in the silicon charge. The resulting power distribution to obtain such a melt is:

- 10240W in the top heater
- 4980W in the bottom heater
- 4592W in the side heater

Figure 3. 16 shows temperature profile, for the configuration with a top cold heat sink, in a vertical cross section of the whole simulation domain. Next to the main heat sources (top, bottom and side), note the presence of two heat sinks (heat exchanger at the bottom beneath the resistor and the cold tube in the top. A felt insulation layer 15 mm thick was added on the bottom of the cold tube to decrease the strength of radiation cooling provided by the tube. Note that the insulation layer is under a high thermal gradient due to its low thermal conductivity.

Stationary: Heat transfer, no fluid mechanics

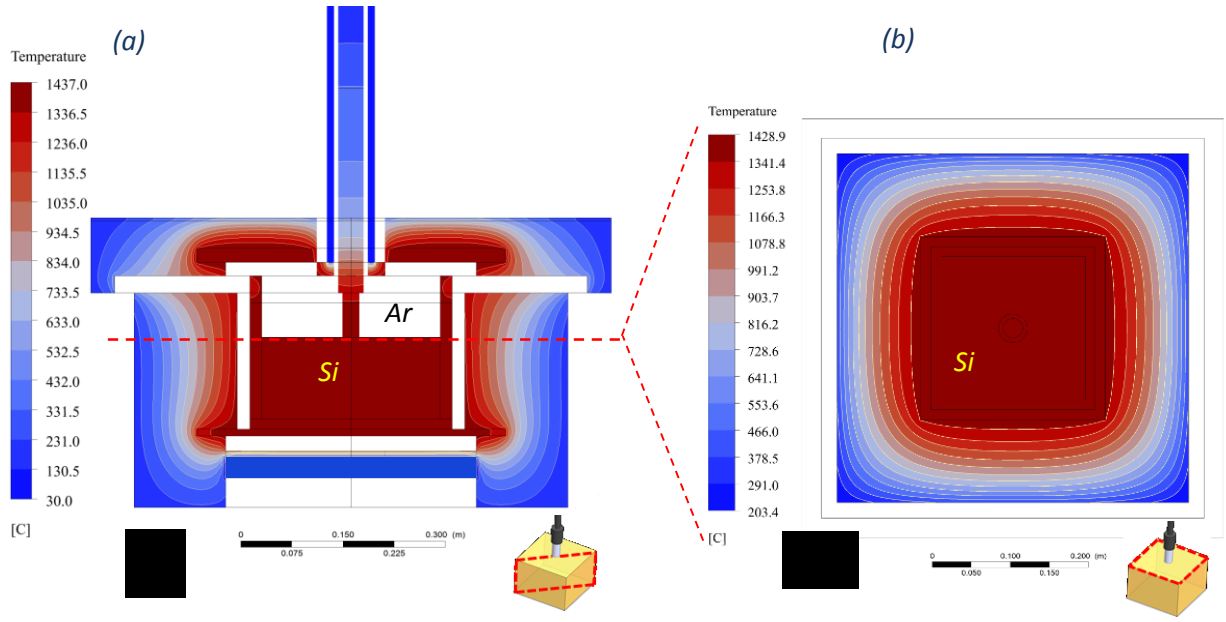

Figure 3. 16. Stationary heat transfer results showing temperature distribution for the whole furnace on (a) a vertical diagonal cross section and (b) a horizontal cross section at the level of the melt surface.(top power : 9.5kW , bottom Power : 3.3kW side Power :3.1kW)

The core of the furnace is well confined thermally thanks to the three heating elements placed around the crucible (Figure 3. 16).

The main heat exchanges to the exterior of the furnace are transmitted to the insulation casing exterior wall and the cold heat sinks. The comparison between the integral values of these heat fluxes, presented in Figure 3. 17, shows that most of the heat is evacuated through the casing wall as expected. Consequent heat loss of 9.4 kW, which is about 65% of the injected power, passes through the outer walls of the insulation casing. The rest of the heat is mainly extracted by the top and bottom cold heat sinks.

Note that the heat transferred to the outer wall of the insulation casing is controlled by conduction through the rigid insulation, while most of the heat flux transmitted to the top heat sink (cold protective tube) is controlled by radiation.

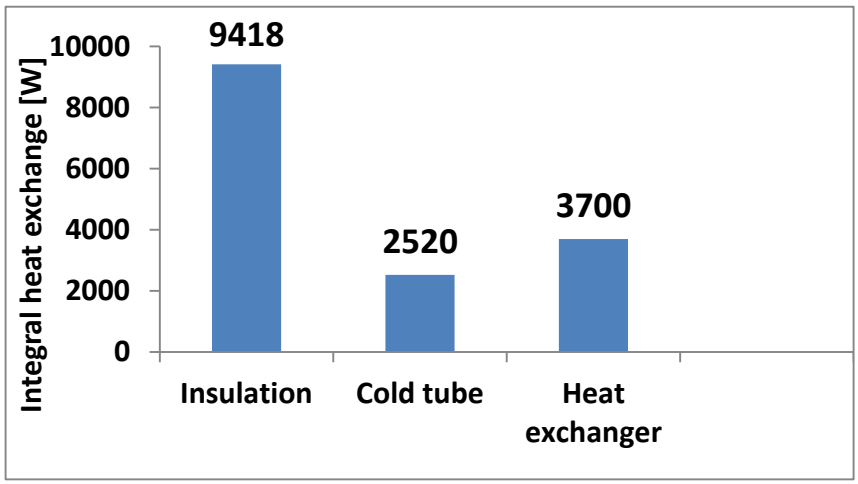

Figure 3. 17**.** Integral Heat loss from the furnace to the cold heat sinks and to the exterior

In fact, the cold tube is surrounded by argon with no solid contact with the other hot solid parts. Note that the heat exchange per surface in the insulation casing (1.46 m^2 area) is equal to 5765 W/ m^2 against 11600 W/ m^2 for the cold tube (0.18 m^2 area). Such high heat extraction density in the cold tube is needed for more localized heat extraction from the central top zone above the melt surface.

Figure 3. 18.a shows the resulting temperature distribution in the silicon charge without convection, since fluid mechanics was not included at this stage of the calculation. The center of the melt surface is the cold spot in the silicon charge. The center is the cold zone while the corners are the hot zone on the surface. Note that the isothermal lines are perfectly circular in the center; the effect of the crucible is only noticeable at closer distances from the wall. The diagonal view (Figure 3. 18.a) shows that, vertically, the top area is colder compared to the bottom where the bottom corners are the hot area in the melt. In a similar way, (Figure 3. 18.b) shows that, horizontally, the center is still the cold spot however, the isothermal lines in the center are no longer perfectly square due to convection loops. In the vertical section, the effect of convection is even more pronounced; the hot spots in the melt that used to be the bottom corners are now shifted to the top corners due to convection.

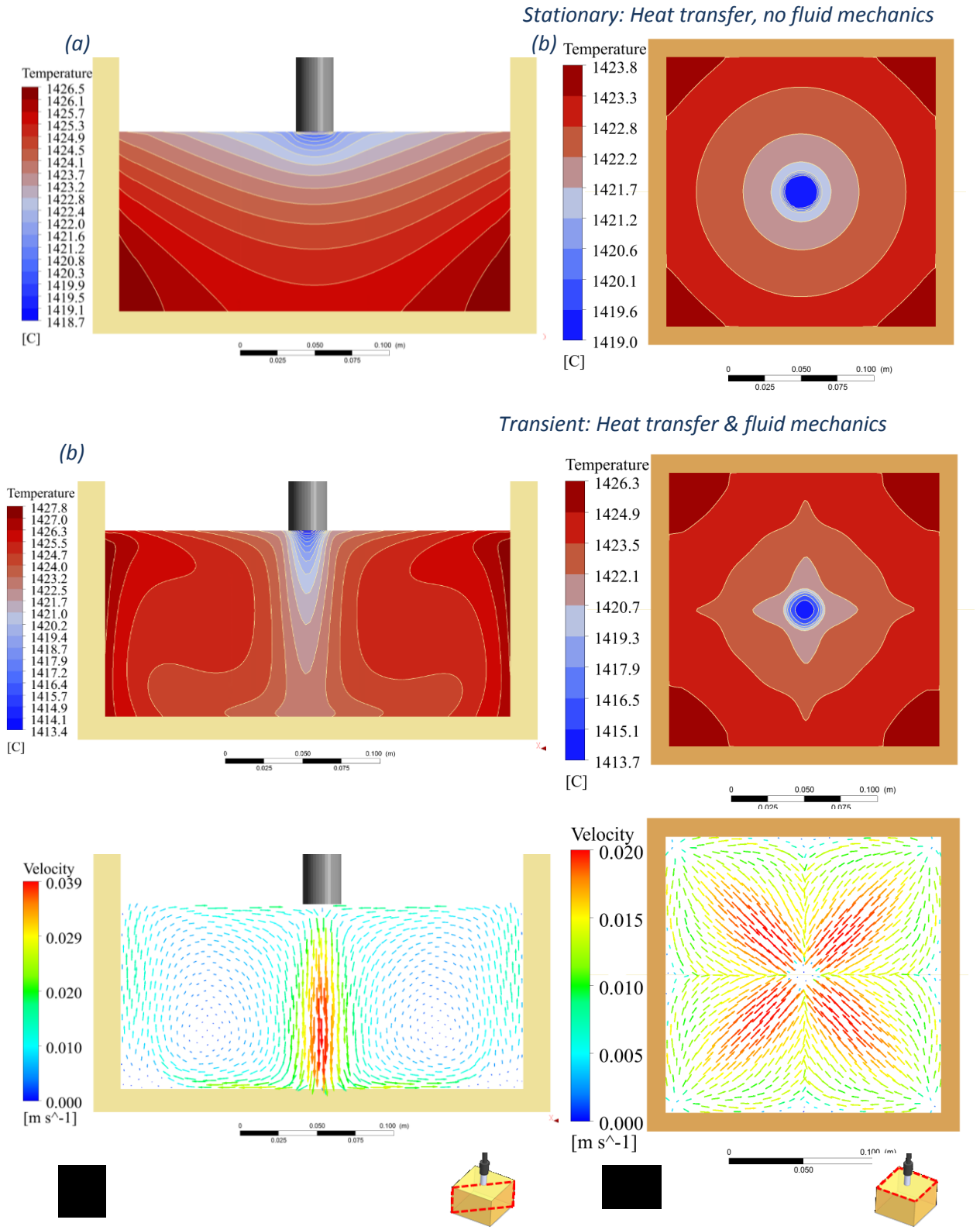

Figure 3. 18**.** Temperature distribution on a vertical diagonal cross section and on the surface of the silicon melt for a stationary heat transfer with no fluid mechanics. .(top power : 9.8kW , bottom Power : 4kW side Power :3.6kW)

The presence of the cold central zone at the dipping spot, illustrated in Figure 3. 18, provides one major condition for Kyropoulos method; however, this condition is necessary but not sufficient. Sufficient heat extraction density is required to maintain the growth from the seed. These considerations are closely related to the heat fluxes exchange between the different walls around of the silicon charge. Figure 3. 19 shows a representation of conduction heat flux in the silicon charge that highlights the thermal connection between the different walls of the silicon charge in a simulated case without fluid dynamics.

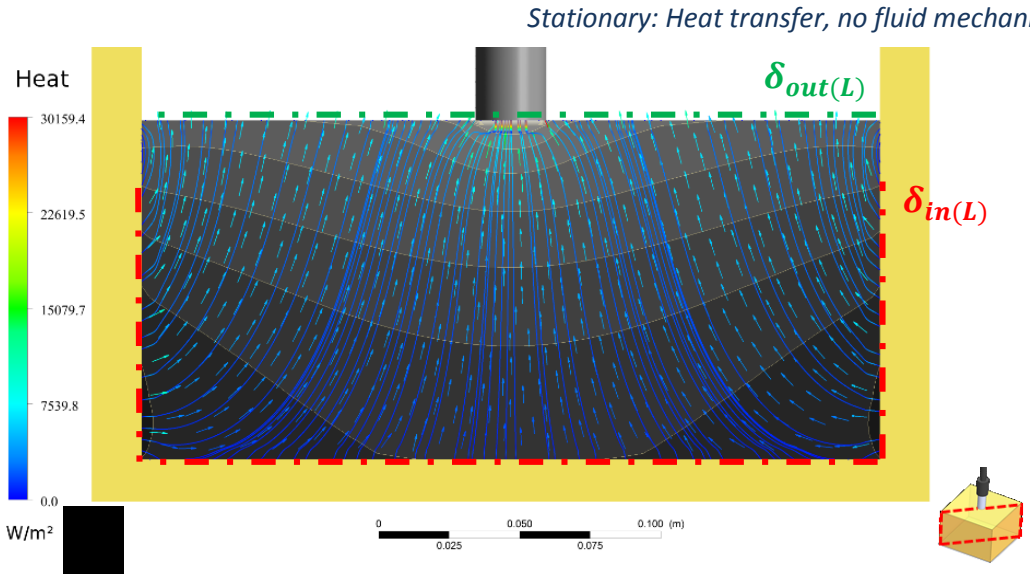

Figure 3. 19. Conduction heat flux in a vertical diagonal cross section of the silicon charge for a stationary heat transfer with no fluid mechanics (The gray shade background is temperature distribution and the stream lines and vectors represent the heat flux).

If we define a spatial contour $\delta_{in}(L)$, representing the walls with incoming flux and another contour $\delta_{out}(L)$ representing the walls with outgoing flux , we may define two function , $f_{\delta_{in}}(L)$ and $f_{\delta_{out}}(L)$,along these contours describing respectively the distribution of the heat flux exchange on the incoming and the outgoing walls. Following the principle of conservation of energy in a closed volume, and assuming that all the incoming flux from contour $\delta_{out}(L)$ is evacuated by the contour $\delta_{in}(L)$, we may say that for each flux value on contour $\delta_{in}(L)$ correspond the same flux value on contour $\delta_{out}(L)$ but at different linear density (W/m for the 2d case). Since,

by definition, the heat flux stream lines will never cross each other, the following equality is always satisfied for certain spatial coordinates to be determined, we may write:

$$\int_{L_{in1}}^{L_{in2}} f_{\delta_{in}}(L)\, dL = \int_{L_{out1}}^{L_{out2}} f_{\delta_{out}}(L)\, dL \qquad (1)$$

Where $\boldsymbol{L_{in1}, L_{in2}, L_{out1}, L_{out2}}$ are spatial position on the in and out contours, and the physical value of the hole integral is a linear flux density (W/m) for the 2D case.

L_{in1}, L_{out1} are reference positions taken at the origin for the measurement of the linear distance along each corresponding contour. For each position L_{in2} on the contour δin(L) we can calculate a position L_{out2} on the contour δout(L). Resolving eq.1 allows the determination of the spatial heat fluxes transfer links between the two contours $\delta_{in}, \delta_{out}$. The present outcome can be used as a guideline to know where to change the flux in one contour to obtain a certain desired change in the other contour.

Based on the prior analysis, the flux representation in Figure 3. 19 indicates that most of the heat flux coming from the side walls will be evacuated trough the top free surface of the silicon charge. Note that the integral heat flux evacuated from the seed is coming from the bottom of the melt. Note also that the growth from the seed may occur by a decrease of the bottom heater power while the side heater maintains the free surface from freezing.

The free surface of the melt is a leading cooling surface in the process which emphasizes the need for the top heater to control the general heat exchange around the silicon charge.

Figure 3. 20 shows that the thermal gradient is much higher beneath the seed compared to the rest of the melt. The spatial variation of temperature is quite linear which means that each zone has a constant thermal gradient except in the passage zone from the seed to the melt where the derivative of the thermal gradient is locally high.

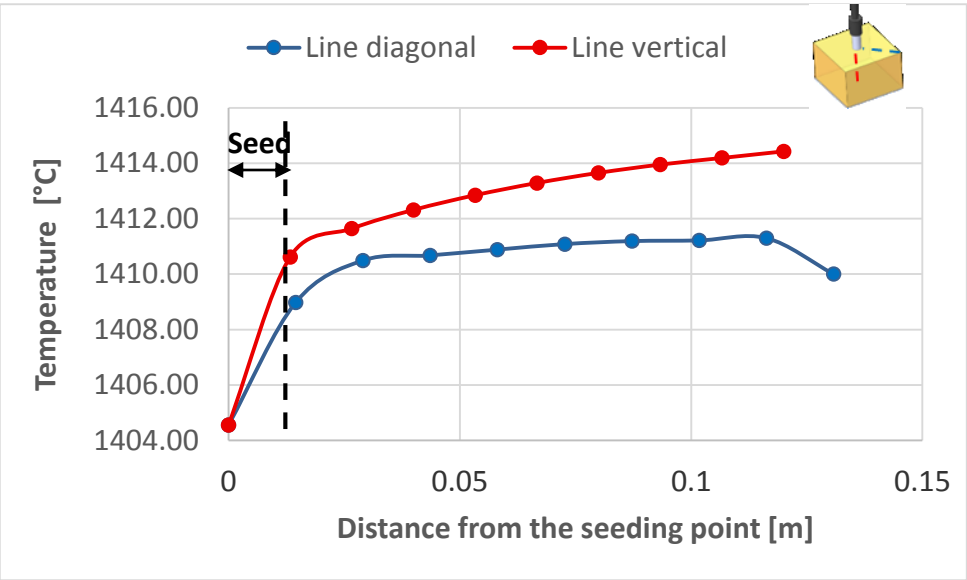

Figure 3. 20. Temperature distribution on a horizontal diagonal line and a vertical central line in the silicon melt for a stationary heat transfer with no fluid mechanics.

This observation could be a possible cause for high density of dislocation in the seeding zone. Note that, the present case, shows that low thermal gradients can be obtained in this configuration. The thermal gradients in the deep melt, away from the influence of the seed, are about 0.25 k/cm in the horizontal direction at the surface and about 0.1 k/cm in the vertical direction. The horizontal and vertical thermal gradient are in the range of 2 k/cm beneath and close to the seed, which can be explained by the higher localized heat density extracted by the seed.

The exchange of heat from the walls of the silicon charge presented in Figure 3. 21 shows that most of the heat, in this low thermal gradient configuration, is received from the side walls while most of the evacuated heat passes through the surface of the melt.

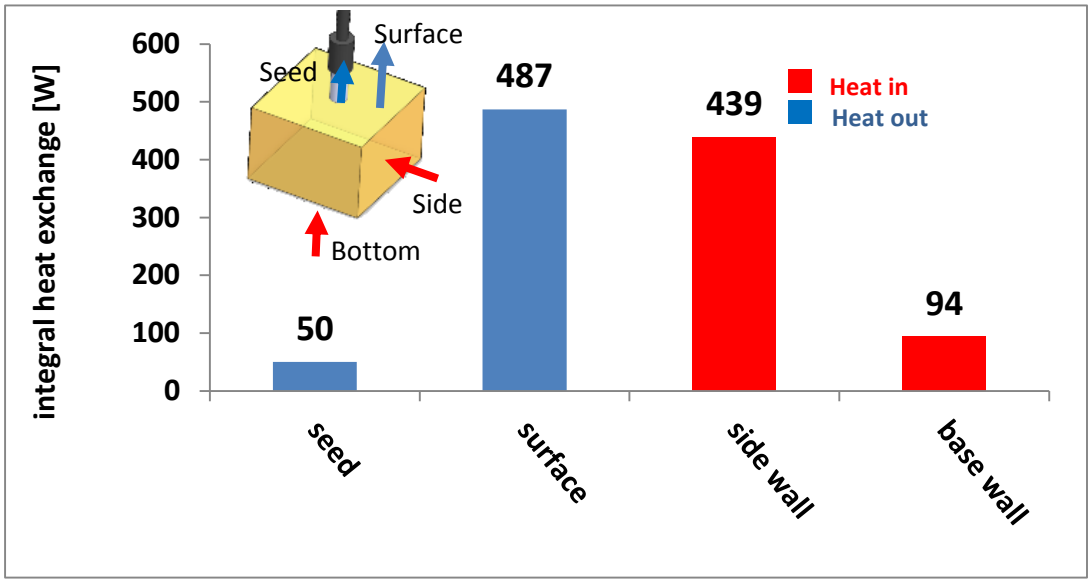

Figure 3. 21. Integral heat exchange from different surfaces limiting the silicon melt.

The free surface of the melt dominates the cooling of the silicon charge during the solidification in the present configuration. Note that the value of incoming heat from the side wall is close to the value of evacuated heat from the surface while the incoming heat form the base wall is closer to the value of heat extracted from the seed. This correlates well with the analysis based on Figure 3. 20 showing the spatial connection of heat exchange between the lateral wall and the free surface, and the connection between the base wall and the seeding zone on the other hand.

Both the bottom and the side walls receive heat to maintain the silicon temperature above the melting point next to the crucible walls. The seed is extracting heat and therefore should sustain crystal growth locally around the seeding zone.

As shown in the dimensional analysis of the flow in chapter 2, the Kyropoulos configuration is unstable with strong buoyant flow affecting the final resulting temperature distribution. Figure 3. 22 shows the resulting velocity profile in the melt at seeding state were the seeding point is at 1414°C, and the horizontal and vertical temperature differences are respectively 12 and 10K..

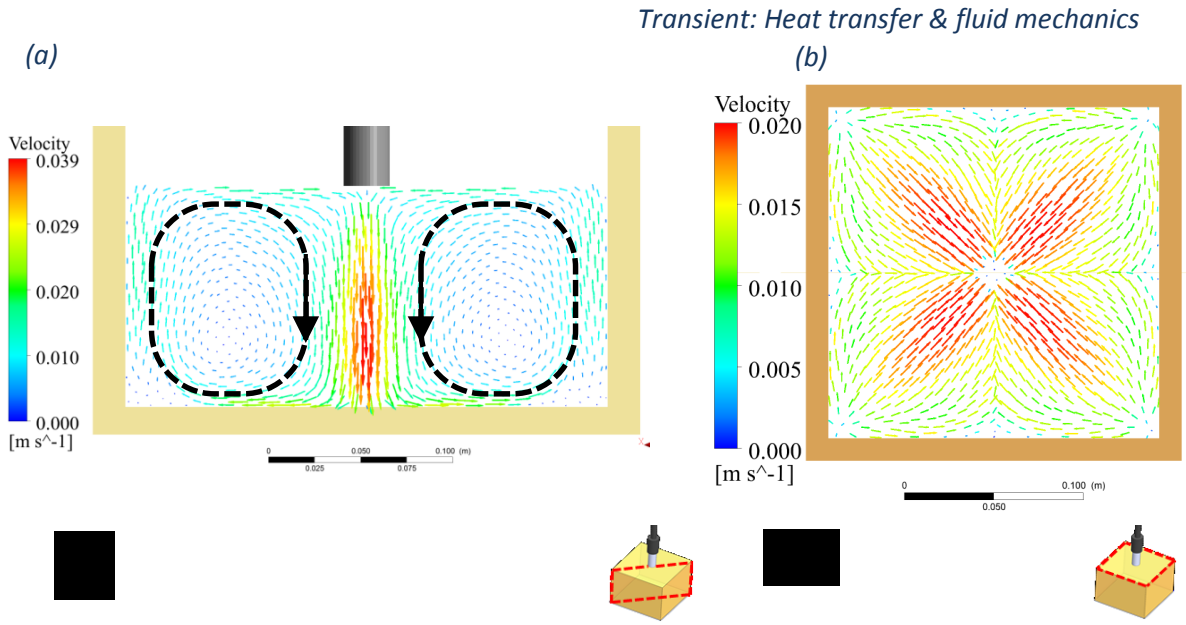

Figure 3. 22. Velocity profile on a vertical diagonal cross section and on the surface of the silicon melt.

According to (Figure 3. 22.b) showing the velocity profile on the surface of the melt, the flow is dominated by four loops flowing from the corners to the center. The flow loops are ascendant in the corners and descendent in the center. Note that, compared to the heat transfer by conduction presented in Figure 3. 18, the shape of the crucible have a much more pronounced influence on the flow of the melt rather than on conduction.

As a consequence of the flow, note how the temperature distribution is now changed. Figure 3. 23.b shows how the circular isothermal lines observed in the absence of fluid dynamics Figure 3. 18.b have now a square shape. The square isothermal lines are rotated 45° compared to the crucible. This shape of isothermal lines is due to the four flow loops coming from the corners. The shape of the crucible itself has limited diffusive thermal effect on the isothermal lines shape in the deep melt and its influence passes mainly through the flow of the melt. The thermal effect of the crucible will be stronger in the vicinity of the wall. The transmission of the square shape of the crucible to the crystal with thermal diffusion will happen at a later stage of the process where the edge of the growing crystal is close enough to the crucible wall. In fact, at a later stage the resulting Péclet number will favor heat transfer by conduction caused by the temperature

difference between the crystal edge and the crucible wall as well as the slowdown of the flow loops caused by the cooling from the crystal.

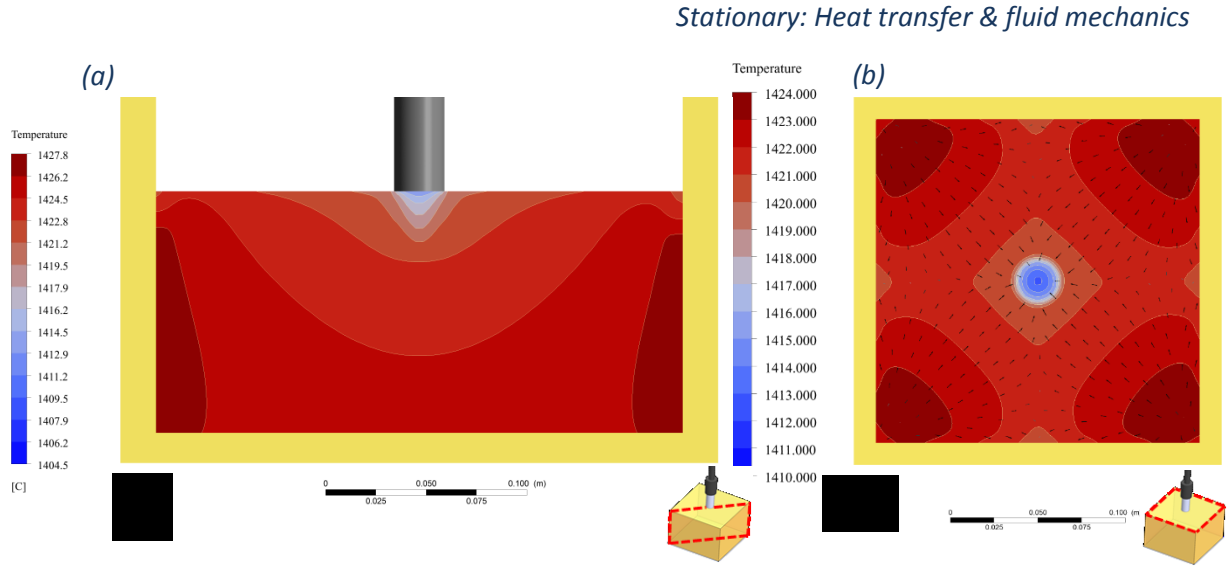

Figure 3. 23**.** Temperature distribution on a vertical diagonal cross section and on the surface of the silicon melt.

The flow loops are transporting the hot melt vertically from the bottom to the top, and horizontally from the corners to the center.

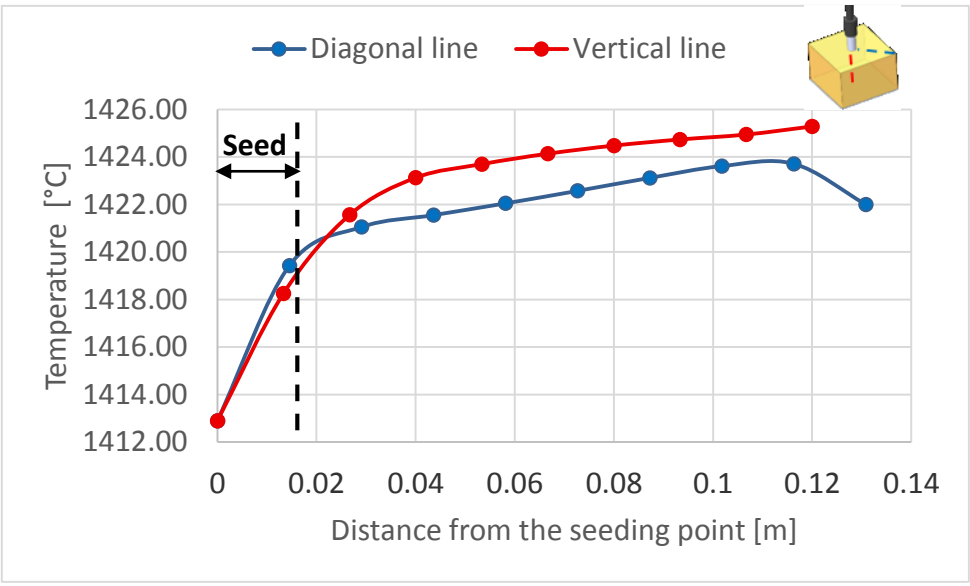

Figure 3. 24**.** Temperature distribution in a diagonal horizontal line and a central vertical line in the silicon melt for a stationary heat transfer with melt flow.

This homogenizing effect results in a constant high thermal gradient beneath the seed, and a constant lower thermal gradient in the deep melt. A transition zone of high variation of thermal gradient connects the two which marks the passage from the seed to the melt similar to the prior presented case without fluid dynamics. Unlike what we expected, the flow did not smooth and improve much the curvature of the thermal gradient next to the perimeter of the seed.

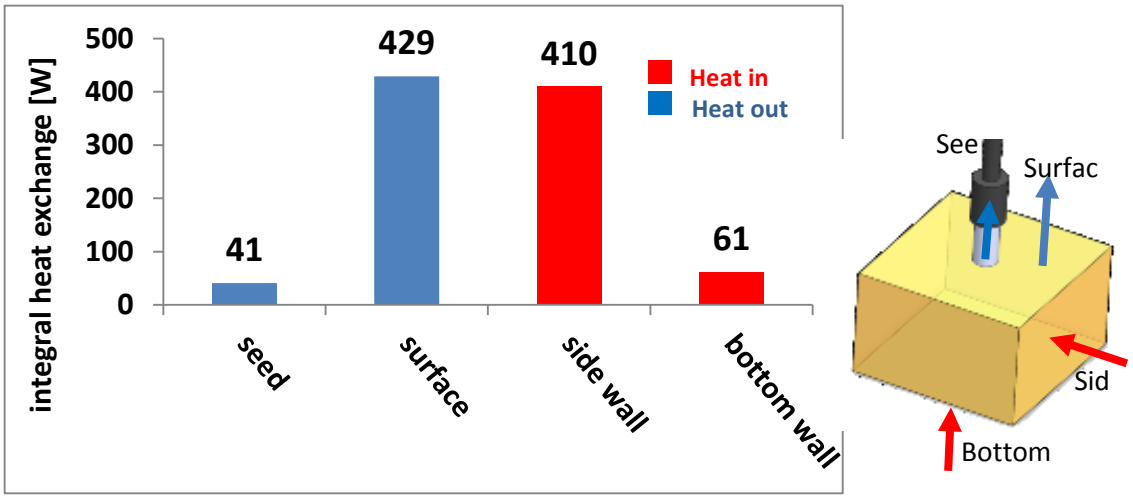

Figure 3. 25. Heat flux exchange from the boundary walls of the silicon charge.

Figure 3.11 shows that the seed have a heat flux extraction of about 41700 W/m^2 while heat extraction from the surface of the melt is about 11800 W/m^2. If such effect is found to be highly detrimental, the two heat extraction densities (from the seed and from the free surface) can be made closer to decrease this second derivative of spatial temperature variation between the seed and the crystal. In all cases, note that most of the heat is received from the side walls which will be mainly evacuated from the top surface Figure 3. 25. At this rate of heat extraction, cooling of the seed is mostly needed in the early stages of the growth. Large crystal will grow mostly due to their own radiating effect. Any further local cooling, if required should target the surface of the growing cystal.

III.4. Conclusion of the third chapter

The starting configuration presented several issues that became the leading points in the development of the process. These issues are summarized in the following points:

- The vertical and horizontal thermal gradients need to be controlled in order to make the top central seeding zone the cold spot
- The required flow should be ascendant in the center and decedent in the corners
- The heat extraction from the top must be sufficient to initiate the growth and the enlargement of the ingot
- Localized heat extraction techniques are required to target the central part of the melt.

The proposed configuration with a ceramic radiation shield allowed a better localized heat extraction from the central part of the melt. Melt flow loops were circulating in the desired direction. Successful growth from the seed was obtained. The installed thermal gradient was consistent during the decrease of power for the enlargement of the crystal.

The growth covered a large area of the crucible approaching closely the crucible walls. The edges of the ingot, close to the crucible walls, where strongly influenced by thermal diffusion from the crucible wall. The ingot inherited the shape of the crucible without any solid contact, for the parts close enough to the crucible. The obtained ingot by this approach was large horizontally covering most of the crucible area. The corners developed hot strong convection due the increase of power in the lateral heater which pushed away locally the growth of the crystal. As a consequence, the crystal did not grow into a full square shape. No set of power distribution in the current configuration was capable of addressing this problem. It became clear that such result can only be obtained by a non-uniform lateral heating in order to decrease the heating power locally in the corners.

The use of the melt convection showed that it is also possible to obtain a square ingot by altering the strength of the flow coming from the four corners of the crucible. A square ingot was obtained numerically. The ingot was rotated 45° according to the vertical axis compared to the crucible. Each side of the ingot was facing one corner of the crucible. The down side of this approach is the limited side of the ingot relative to the side of the crucible. The obtained ingot covered approximately 60% of the free surface of the melt.

The ingots had a bun shape inside the melt where the vertical growth is lower compared to the horizontal growth. The vertical growth was limited by the state of thermal equilibrium of the crystal depending very much on convection and heat extraction from the top of the growing ingot.

The new configuration with a cold tube heat sink in the top was proposed to enhance the heat extraction from the top. The configuration enhanced the seeding and growth conditions. Further perspectives are proposed to redirect the radiation cooling to target more locally the central zone.

As proposed in the literature, it is possible to enhance the vertical growth by a very slow pull up enough to bring the crystal out of its thermal equilibrium but fairly small to keep the solid liquid interface inside the melt. A growth can be achieved by an alternation of small pull up of the crystal and growth inside the melt.

Providing that the size of the ingot was only limited by the size of the crucible, the method can expect a consequent total mass growth rates even at very small pull up velocity if the proper scaling is done.

Chapter 4

IV. Real cases simulation and experimental work

The current chapter summarizes the impact of the numerical simulation on the development of the experimental Kyropoulos process.

Numerical analysis of experimental crystal growth results will be presented in order to relate the behaviour of the crystal growth to the corresponding physical phenomena. Causes of unexpected problems will be identified and explained in order to propose solutions. The proposed solutions are then validated numerically and experimentally.

This chapter investigates observed repetitive patterns of crystal growth using numerical analysis. The analysis aims to define the physical phenomena related to each growth pattern. Such comprehension will be used to determine the required adjustments of the operating parameter of influence (design features, heating power distribution and cooling procedure) in order to control the solidification process.

The chapter will also present the experimental investigation done in the scope of this thesis to validate the results of the numerical development the process.

The first part of the chapter presents the recurrent asymmetric growth in the process, noticed experimentally and numerically. Numerical analysis results are then used to explain the physical phenomena causing the asymmetric growth

The second part of the chapter proposes solutions to enhance the growth symmetry. Numerical results are presented to demonstrate the effect of the applied solutions. Experimental results are then presented to validate the approach.

IV.1. Growth symmetry loss in Kyropoulos process for silicon

IV.1.1. Experimental observation

The used furnace in this work had a four symmetric square shape, and therefore, the growth from the seed was expected to be symmetric as well. Figure3.2 in the prior chapter shows that the thermal effect of the crucible square shape decreases in the deep melt where the isothermal lines become more circular in the center which should be closer to an axisymmetric configuration in the center. Despite these expectations, important loss of crystal growth Symmetry was noticed in a parallel experimental results (L.Lhomond thesis) obtained in the same project.

The asymmetry was recurrent reproducing repetitive particular features in shape and orientation of the asymmetric growth. The seeding step was done without rotation. The rotation of the seed was then added when the crystal started to grow. The applied rotation speed was 3 rpm. Concerning the pull up of the crystal in the vertical direction, the growth was obtained by an alternation of pull up and fixe positions. The pull up speed was 1-2 mm/h

Table 4. 1. Experimental crystals presented in parallel thesis

configuration	Growth symmetry	weigh	microstructure	Pull up	rotation
Case 1	*Asymmetric growth*	*520 g*	*Polycrystalline*	*alternated*	*Inconsistent. 3 rpm*
Case 2	*Asymmetric growth*	*95 g*	*Polycrystalline*	*alternated*	*Inconsistent. 3 rpm*

The crystals presented in Table 4.1 were obtained using a 1 inch diameter monocrystalline silicon seed. The seeds had a <100> crystalline orientation in the growth direction. The obtained asymmetric crystals were polycrystalline.

Figure 4. 1 shows the two obtained crystals presented in Table 4. 1. The growth started from the seed without any contact with the crucible.

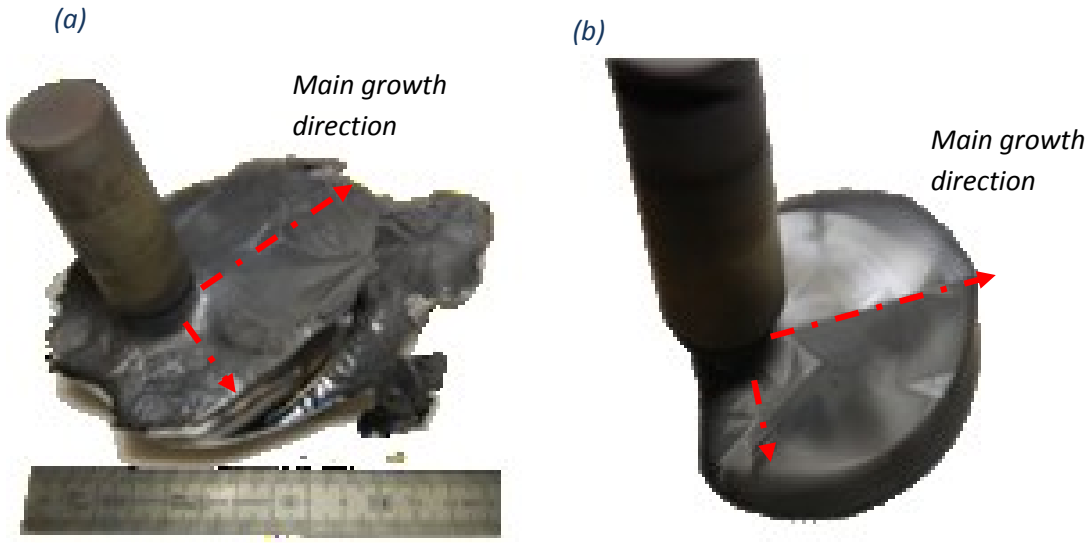

Figure 4. 1. Obtained experimental silicon crystals using Kyropoulos technique showing strong growth asymmetry with recurrent features. (a) Crystal case 1 and (b) crystal case 2.

Note that both crystals are strongly asymmetric and comparable in shape. Several distinguishing features can be observed in the obtained asymmetric crystals:

- The asymmetric growth is mainly oriented in one preferential direction.
- Note that the growth is strongly limited in the opposite direction of the growth.
- Some side growth can be noticed in both sides following the perpendicular direction to the main growth orientation.

The resulting meniscus at the seeding point where the seed contacts the melt, is marked in Figure 4. 1 by a slight step in the apparent mass signal. Note that for this experiment, the growth process was an alternation of pull up and fixe positions. Note that, generally the pull up of the crystal results in the increase of the apparent mass which is mainly related to the formation of the meniscus and therefore of real crystal mass, providing it solidifies. On the other hand, note that, in fixe positions, the apparent mass decreases slowly indicating growth inside the melt

beneath the free surface such as described in chapter 2 (Figure 2.14). Note that the first pull up did not involve consequent mass gain. It is suspected that at this stage the surface of the crystal was small and a parallel vertical growth inside the melt was compensating the apparent mass by floatability forces. The following pull up, at the same pull up speed, had a much clearer influence on the mass gain which indicates a larger meniscus and therefore a wider contact area between the crystal and the melt.

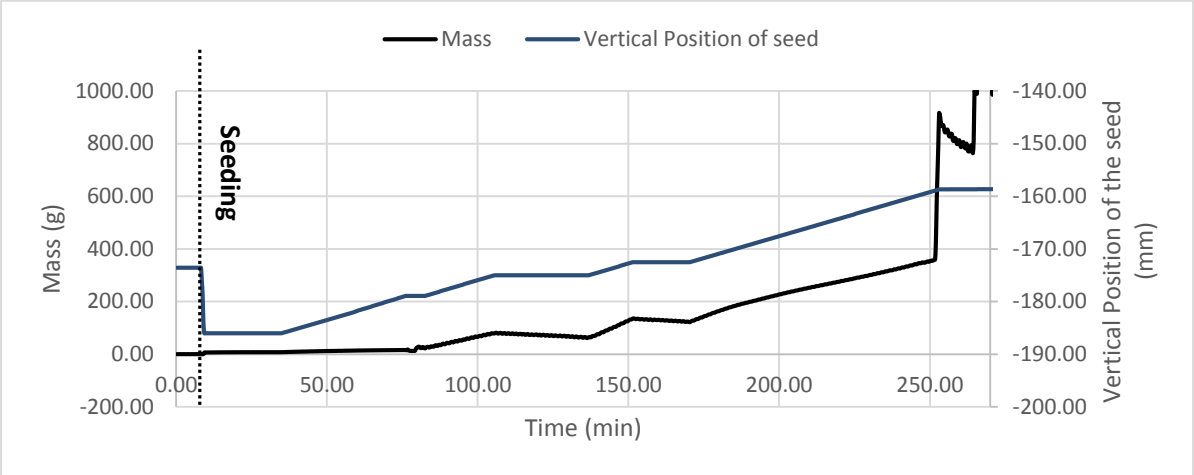

Figure 4. 2. Variation of vertical coordinate of the seed and the apparent mass of the crystal during the growth of asymmetric crystal case 1

The conditions of the growth were transient; Figure 4. 3 shows the evolution of power controlled by the operator during the growth. The top and bottom power variations were recorded automatically at an interval of 15 seconds while the side power was adjusted and recorded manually for each variation.

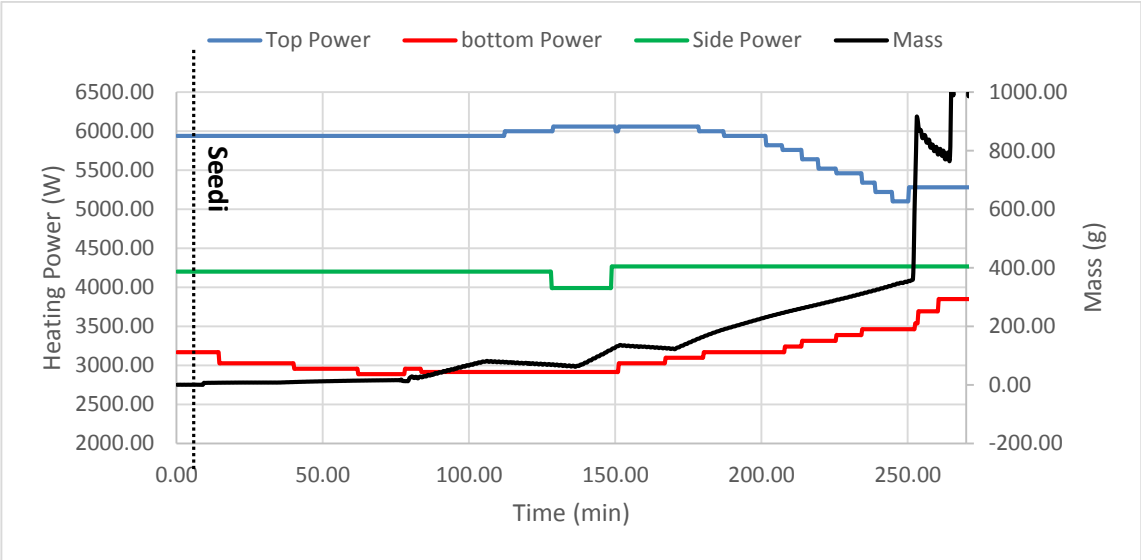

Figure 4. 3. Experimental power decrease for the growth of the asymmetric crystal case 1 in the top and bottom heater next to the signal of the apparent mass.

The side heater was adjusted according to a side thermocouple marked as thermocouple 5 in Figure2.7.

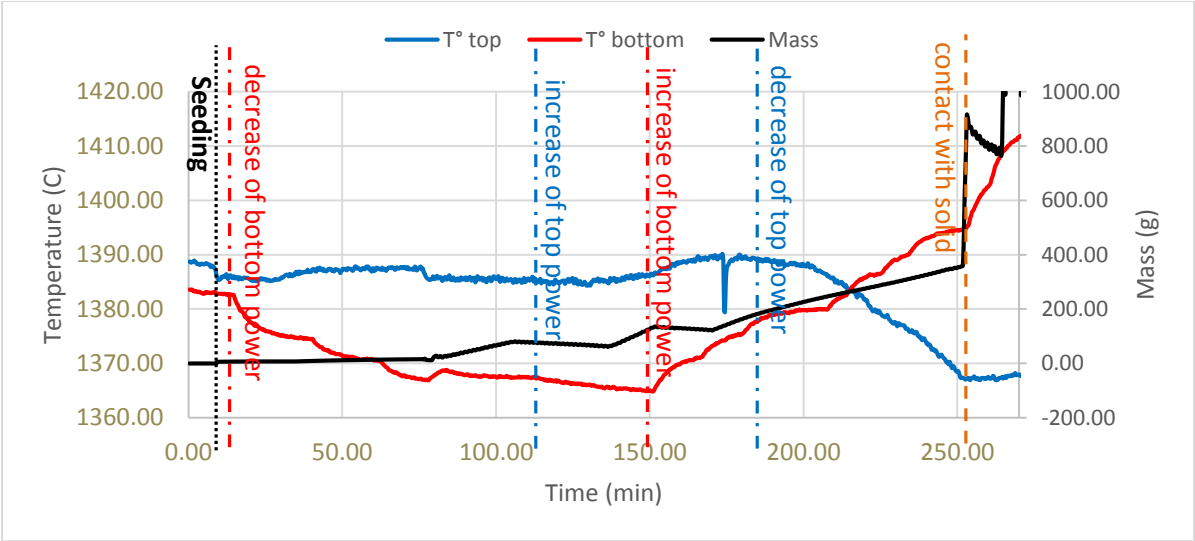

Figure 4. 4. Evolution of temperature in the top and bottom heaters during the growth of the experimental asymmetric crystal case 1, next to the signal of the apparent mass.

Table 4. 2 summarizes the different crystal growth experiments done in the scope of this thesis:

Table 4. 2. experimental crystals obtained in the scope of the current thesis					
configuration	growth	Size	microstructure	pull up	rotation
Case 3	*Symmetric growth*		*Polycrystalline*	*No pull up*	*15 rpm*
Case 4	*Symmetric growth*		*Monocrystalline*	*No pull up*	*15 rpm*
Case 5	*Symmetric growth*		*Monocrystalline*	*No pull up*	*15 rpm*

Top seeding processes to grow crystals from the melt can be particularly sensitive to loss of symmetry due to the unconfined nature of the growth. Prior chapter explained how more active heat extraction from the seed can reinforce symmetric growth of the crystal. However, concentrated heat extraction will increase the curvature of the thermal gradient rising the risk of defect generation and therefore is not desirable. Since this is a top seeding process, the natural approach to extract heat was by decreasing the temperature of the top heater. Using this approach, numerical results showed that the crystal growth is sensitive to asymmetric growth even if the 3D geometry in the numerical model did not have any asymmetry.

A parallel experimental thesis (L.Lhomond) working on Kyropoulos growth for silicon showed a comparable asymmetric growth as well. The asymmetric crystals had a distinctive repetitive pattern in shape and aspect. Most of the problems related to undesired asymmetry of crystal growth are usually related to an asymmetry in the furnace. However, the recurrent asymmetry in the numerical simulation as well suggested that the cause of this asymmetric growth may be physical and not related to the experimental furnace imperfections.

IV.1.1.1. Presentation of the different case of study for the asymmetric growth

Case 1 and case 2 presented in Table 4. 3 ((L.Lhomond-2016) are two examples of crystals with symmetry loss using Kyropoulos technique. A parallel numerical simulation (column 3 in Table 4. 3) is presented to explain the behaviour of symmetry loss. The fourth column in Table 4. 3, named “typical starting melt”, is a reference case were all the silicon is fully melted; this state is the preceding state before starting the cooling for the growth.

Table 4. 3. Numerical and experimental operating parameters in the case of asymmetric growth				
	Experimental Case 1	**Experimental Case 2**	**Numerical case**	**Typical starting melt**
Top power (W)	*13235*	*9000*	*11700*	*15840*
Bottom power (W)	*4500*	*4016*	*4680*	*5850*
Side power (W)	*3599*	*4260*	*3900*	*0*
Top heater T (°C)	*1370*	*1386*	*1390*	*1458*
Bottom heater T (°C)	*1444*	*1381*	*1447*	*1498*

Note that both experiments and the "Numerical case" listed in Table 4. 3 follow comparable approaches to control the growth. The temperature in the top heater is decreased to initiate the growth of the crystal. The numerical results presented in Figure 4. 5 displays the resulting temperature profile in the melt at dipping conditions. Note that the seeding spot is at lower temperature of 1411°C slightly below the melting point and the temperature variation is continuously increasing on the edges (Figure 4. 5.a). Note also that the bottom of the melt is at higher temperature compared to the top (Figure 4. 5.b). The melt has adequate seeding conditions for a central top seeding procedure.

IV.1.1.1. 1 Numerical investigation of the asymmetric growth

The numerical calculation included fluid dynamics, heat transfer (conduction, convection and radiation), and phase change. The growth was initiated by reducing the power in the top resistor as shown in Table 4. 3.The initial state before solidification is presented in Figure 4. 5.a showing that the flow and the temperature have a clear 4-fold symmetry. The maximum flow velocity was in the range of 2 cm/s. Figure 4. 5.b shows the resulting simulated crystal colored by temperature as well as the flow loops in the melt. The simulated crystal is strongly asymmetric even if the starting flow and temperature profile were symmetric.

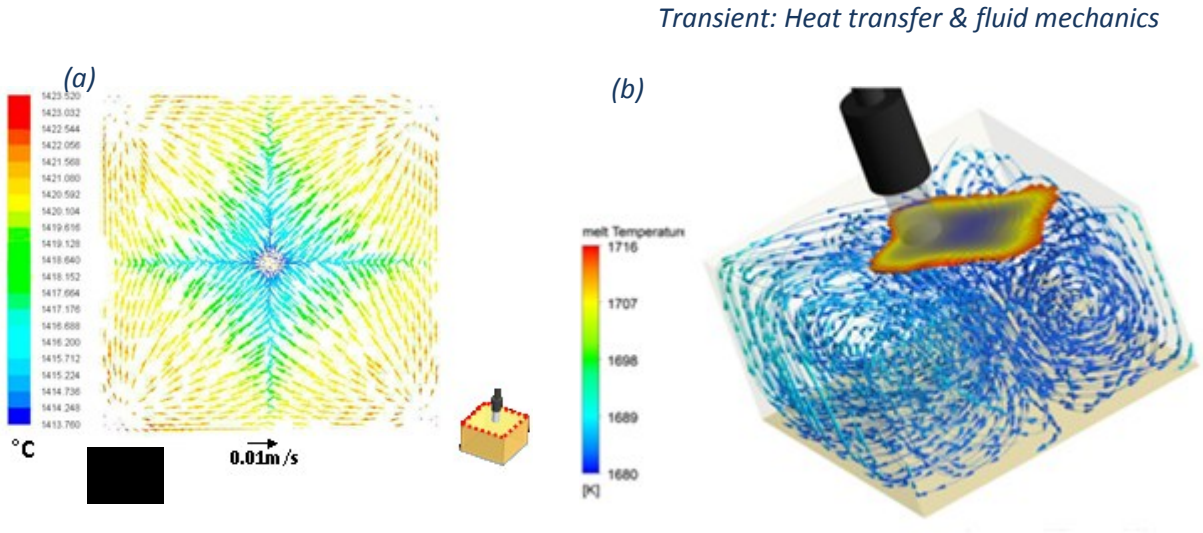

Figure 4. 5. (a) Velocity profile at the melt surface colored by temperature, showing stable four symmetry, used as initial state for the growth of asymmetric crystal (b) Isometric view of the melt with flow streams showing asymmetric crystal growth.

This asymmetric crystal growth is more than a problem related to the furnace asymmetry. The asymmetry is the outcome of a physical phenomenon.

Note that the cold spot shifts from the center of the seeding spot to the center of the crystal surface. The radiative cooling overcomes the conductive cooling from the seed. The cooling of the crystal by radiation increases with the increase of the radiating surface of the crystal and with the increase of emissivity. The higher emissivity of the solid phase (compared to the liquid phase) amplifies any irregularity to grow in one preferential direction .Any shape irregularity of the crystal, that has larger radiative surface, cools down faster due to radiation heat transfer; the larger it gets the faster it grows. This analysis explains the rapid growth of the crystal in an irregular shape; yet, it is not sufficient to explain the almost unidirectional growth. One question remains: what is restricting the growth in the other directions?

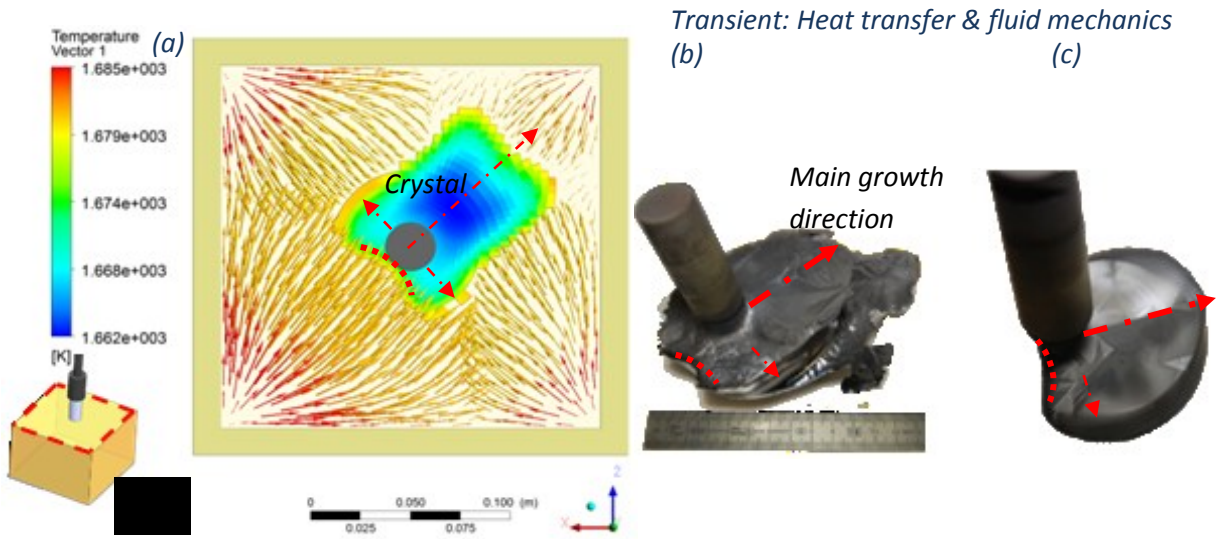

Figure 4. 6.(a) top view of the melt surface showing the melt flow and the growing crystal colored by temperature, (b) and (c) the obtained experimental asymmetric crystals in case 1 and case 2.

Both numerical and experimental crystals (a), (b) and (c) displayed in Figure 4. 6 , have an asymmetric growth mainly oriented to one direction. Most of the growth was in the asymmetry direction but some growth can also be noticed on the perpendicular sides to the asymmetry direction. Note also that the back side of the crystal in the reverse direction of the growth was clearly restricted from growing. In addition, the undeveloped back side of the crystal have a curved profile toward the seed strongly suggesting a hot melt flow effect. Note that the simulated crystal has the same geometric curvature in the back side at the reverse direction of the growth; the exact same feature is also observed in all the experimental crystals.

Figure 4. 6 shows the temperature profile and the melt flow beneath the asymmetric crystal. The flow loops on the side where the crystal is large become weaker due to the cooling provided by the crystal. The temperature profile shows that the back side of the crystal is facing a stronger melt flow loop at higher temperature. Note how the back crystal curvature is in fact in the direct trajectory of the hot stronger flow loop. This explains clearly the presence of the curved profile on the back of the asymmetric crystals (obtained numerically and experimentally).

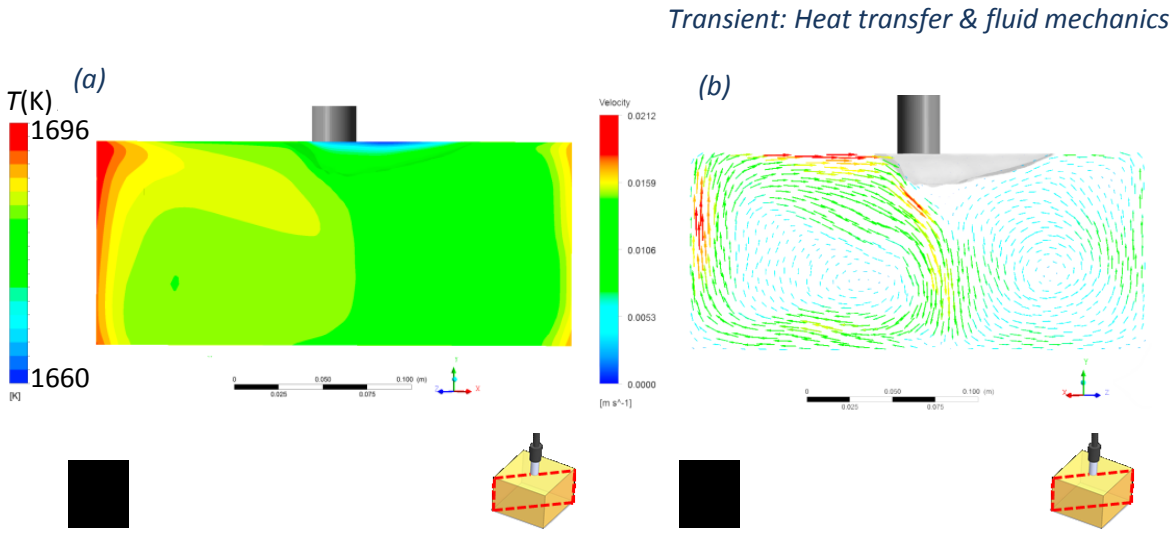

Figure 4. 7.Temperature distribution and velocity profile in the silicon melt beneath the asymmetric crystal in a vertical diagonal plane.

The asymmetry must be quite stable since the fluid flow dissymmetry reinforces the asymmetric growth for a long distance, covering almost the full possible length in the crucible. In fact, the two responsible physical phenomena, localized radiation cooling and the melt flow, are acting in the same direction. The emissivity effect and the fluid flow dissymmetry in the silicon melt are strongly coupled in the Kyropoulos configuration, one phenomenon empowers the other. The higher emissivity of the solid silicon increases the cooling down of the crystal which slows down locally the flow loops on the side of the crystal growth direction. On the one hand, the colder and slower melt flow loop nearest to the crystal increases the rate of growth of the crystal and therefore increases the solid radiating surface. On the other hand, the strong and hot flow loop in the reverse direction of the growth is blocking the growth of the crystal in the back side leaving a clear curved mark.

In the light of these results, we conclude that the asymmetric growth in Kyropoulos process for silicon is the result of a coupling between melt flow and radiation cooling due to the sudden increase of emissivity during solidification.

It is not clear which phenomenon happens first; but, in both cases the outcome will be the same due to this strong instantaneous coupling.

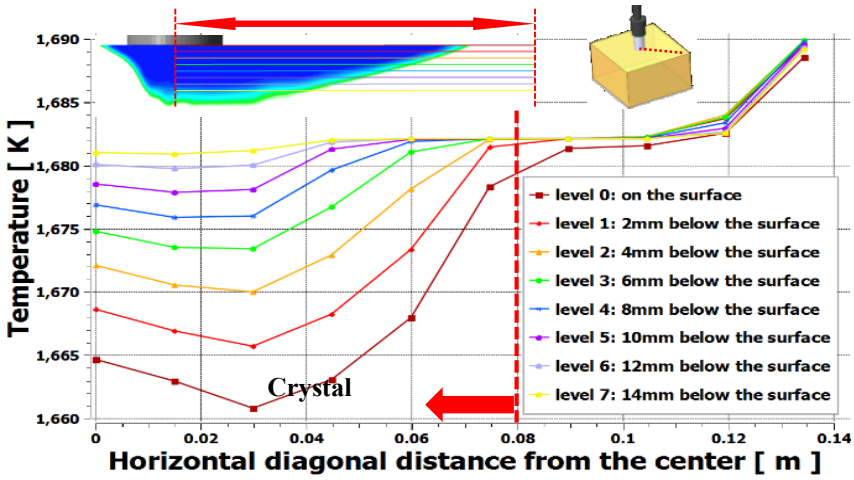

Figure 4. 8. Variation of temperature in the asymmetric crystal and the melt along diagonal line taken at different horizontal levels (2mm step)

The temperature profile in the crystal along the diagonal direction at different vertical positions is presented in Figure 4. 8. Note that the curvature of the temperature variation is higher close to the crystal surface and lower near the melt. The radiative cooling is not as homogeneous as suspected. The passage from the seed to the crystal is affecting locally the thermal gradient in the crystal.

IV.2. Growth analysis of the symmetric crystal growth of silicon

Based on the prior physical analysis of the asymmetric growth in Kyropoulos process for silicon; solutions can be proposed to enhance the growth symmetry. Furthermore, if these solutions should work, they will also validate the analysis about the cause of asymmetry as well. Two problematic points needs to be addressed:

- The sudden increase of radiation cooling due to phase change must be suppressed
- The effect of the melt flow on the crystal must be homogenized

These controls can be achieved using the following proposed modifications, to be applied during the growth of the crystal:

- The effect of sudden emissivity increase of the solid crystal by suppressing the radiative cooling. This cooling can be decreased if the outer radiating temperature (of the top heater) is adjusted to be close to the silicon melting point.
- The effect of the melt flow on the crystal can be homogenized using crystal rotation as proposed in the literature and mentioned in the first chapter.

These modifications are not intended to be applied for the whole process, because the first one decreases the heat extraction from the top and thus the growth rate, while the second one is impossible to keep during the full process if square ingots are desired. However, they are only necessary during the first part of the process (initial horizontal growth), after which it should be possible to stop the crystal rotation without the risk of symmetry loss, and then decrease the top heater temperature to increase radiative cooling when almost all the surface is occupied by solid silicon. The second phase should make the crystal grow downwards in the vertical direction with a symmetrical shape constrained by the crucible walls and side heaters.

Concerning the rotation, it is required to know what the optimal rotation speed fur the current process is.

To answer this question, it is helpful to start from the physical reason behind the rotation. In fact the rotation of the crystal is used will homogenize the interaction between the melt and the crystal.

As demonstrated in chapter 3, the convection in the present configuration is shaped in four equal main loops coming from the corners of the square crucible, where each two loops are facing each other and therefore conserving the symmetry in the diagonal plane according to the center.

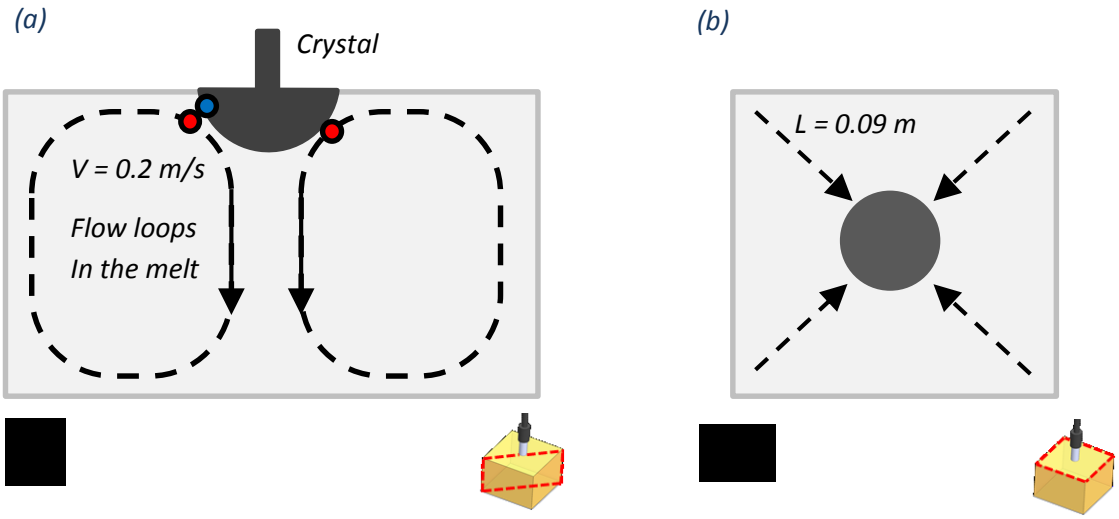

Figure 4. 9. Diagonal and top view of flow interaction with the crystal.

To obtain symmetric interaction between the crystal with 0.1m diameter and the melt, any point in the crystal at the solidification interface should be exposed equally to the pair of two facing loops. This condition can be satisfied if the time t_p , representing the time for a flow particle to go from the hot corner to the crystal , is equal to t_ω , the time required for the crystal to complete half rotation. Therefore, we may write:

$$t_p = t_\omega \quad \Rightarrow \quad \frac{L}{v_p} = \frac{\theta}{\omega} \quad \Rightarrow \quad \omega = \frac{\theta \ v_p}{L} \ = \ \frac{2\pi \ \times 0.04}{2 \ \times \ 0.09} \ = \ 1.395 \, rad/s$$

Where v_p is the velocity of the flow, and ω is the angular velocity of the crystal rotation.

According to this estimation of order of magnitude, a minimum crystal rotation of 13.3 rotations per minute is required to homogenize the interaction between the crystal and the melt flow loops in the present configuration.

IV.2.1.1. Presentation of the studied cases

While top seeding processes are based on heat extraction from the top, note that prior listed approach suggests to keep the temperature in the top heater at higher values close to the melting point of silicon at the first stage of the crystal growth. The following part will investigate the efficiency of these solutions and at the same time the validity of the analysis made in the prior section. Table 4. 4 summarizes the working condition for the numerical and experimental tests for the case of symmetric growth

Table 4. 4. Numerical and experimental operating parameter used for the investigation of symmetric crystal growth

	Exp Case 3	**Exp Case 4**	**Exp Case 5**	**Num case**
Top power (W)	*4681*	*6480*	*6450*	*5220*
Bottom power (W)	*6420*	*6240*	*5540*	*5411*
Side power (W)	*3822*	*1346*	*1646*	*4023*
Top heater T (°C)	*1404*	*1409*	*1411*	*1409*
Bottom heater T(°C)	*1416*	*1403*	*1398*	*1419*

Compared to the asymmetric cases, the temperature in the top heater for the symmetric cases was regulated close to the melting point of silicon in order to limit the radiative cooling. The growth is initiated by decrease of the power in the bottom heater

The growth of the crystal started from the center of the contact zone between the seed and the melt. The grown crystal is symmetric and the flow stayed symmetric as well even with the presence of the rotating crystal. The rotation of the crystal was stopped at mid-range of the horizontal median distance (50 mm from the center).

IV.2.1.2. Numerical investigation of the symmetric growth

Figure 4. 10 shows the numerical results for the simulation case using the parameters given in Table 4. 4. Crystal rotation (15 rpm around the vertical axis) was added starting from the beginning of the process. The temperature of the top heater was kept close to the melting point about 1 to 20 degrees lower. The cooling of the melt to grow the crystal was mainly sustained by the decrease of the bottom heater at the beginning of the process and then shifted to the decrease of the power in the upper heater.

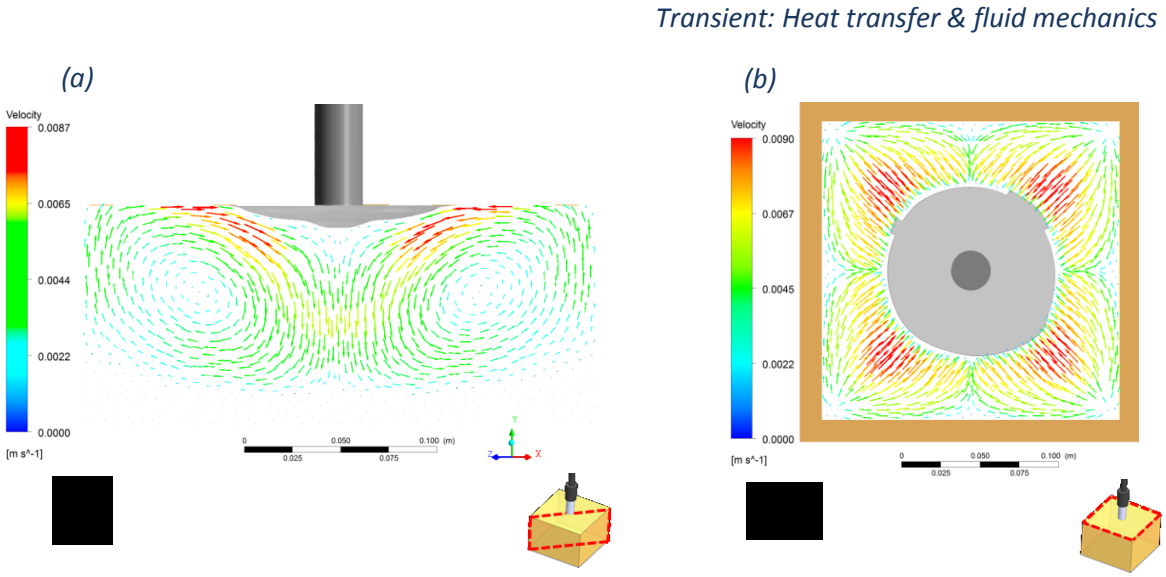

Figure 4. 10.Diagonal and top view of symmetric crystal growth and velocity profile in the silicon melt given by the numerical case.

At an advanced stage of the process, solidification of silicon started from the bottom of the crucible as well. This was due to the decrease of power in the bottom heater. The first stage of growth is achieved by lowering the heating power in the bottom resistor and therefore lowering the temperature of the global melt. The crystal starts to grow beyond the perimeter of the seed in a symmetric way. When the temperature of the bottom heater reached a low value at 1380 °C, the cooling was shifted to the upper heater as well. The crystal at this stage had a diameter of 40 mm. the growth was sustained by a parallel cooling of the top and lower heaters; the radial growth of the crystal accelerated under the effect of the top heater cooling. The power in the side heater was adjusted to stop any solidification from the walls of the crucible.

The success of the second stage of the growth depends highly on the success of the first stage. The formed symmetric crystal becomes less sensitive to symmetry loss as it grows allowing the decrease of the top heater power in the numerical investigation. Radiation cooling from the top surface of the growing crystal increases until it becomes the leading factor in heat extraction.

The resulting crystal from this numerical simulation was a circular bun shape crystal. The crystal is flat with a circular horizontal cross section and the horizontal to vertical shape aspect ratio was about 5/3. The flat aspect ratio of the crystal has been listed in several experimental investigation in the literature as a limiting problem for Kyropoulos process, however, more in-depth information about this particular aspect is discussed in further details in the precedent chapter.

IV.2.1.3. The resulting experimental symmetric crystals

Comparable experimental crystal growth was accomplished using similar conditions of crystal rotation and no pull up of the crystal to reproduce the same growth conditions in the numerical model presented previously. A silicon seed of <100> orientation was dipped into the melt at seeding condition. The heating power at dipping condition is presented in Table 4. 4 for experimental case 1. Further details about the cooling procedure is presented in Figure 4. 13 and Figure 4. 12.

Figure 4. 11 shows the obtained symmetric crystal. The crystal in the image is still connected to the seed. The resulting crystal was comparable in shape and in size to the obtained crystal in numerical simulation, however the growth time in the numerical model was a shorter, this was mainly due the lower temperature of the bottom heater in the model compared to the experiment. The crystal was a circular bun shape mass with a flat aspect ratio horizontal/ vertical equal to 20/3. The maximum diameter of the circular horizontal cross section was 100 mm. The crystal had to be extracted prematurely due to the formation of dendrite in the melt coming from the crucible wall. The crystal was not at equilibrium state as shown by the decreasing curve of the apparent mass signal indicating that the crystal is growing inside the melt. The aspect ratio

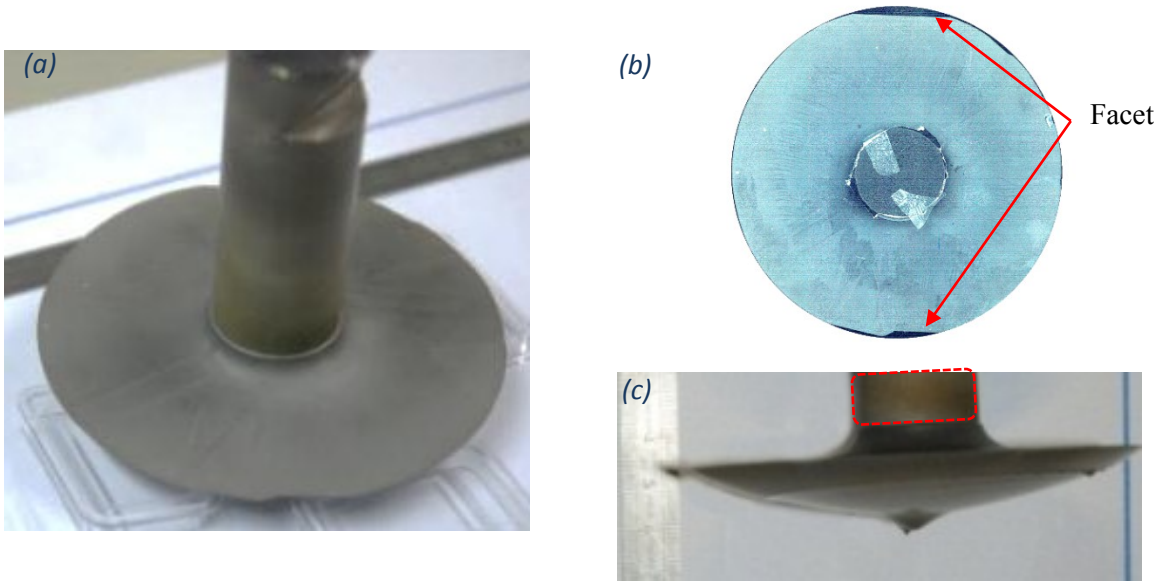

Figure 4. 11. (a) Obtained experimental symmetric silicon crystal case 1 (b) top side view of the crystal (c) side view of the crystal

was not representative of the equilibrium state since the horizontal growth advances faster than the vertical growth. More in-depth information about this particular aspect is discussed in further details in the precedent chapter.

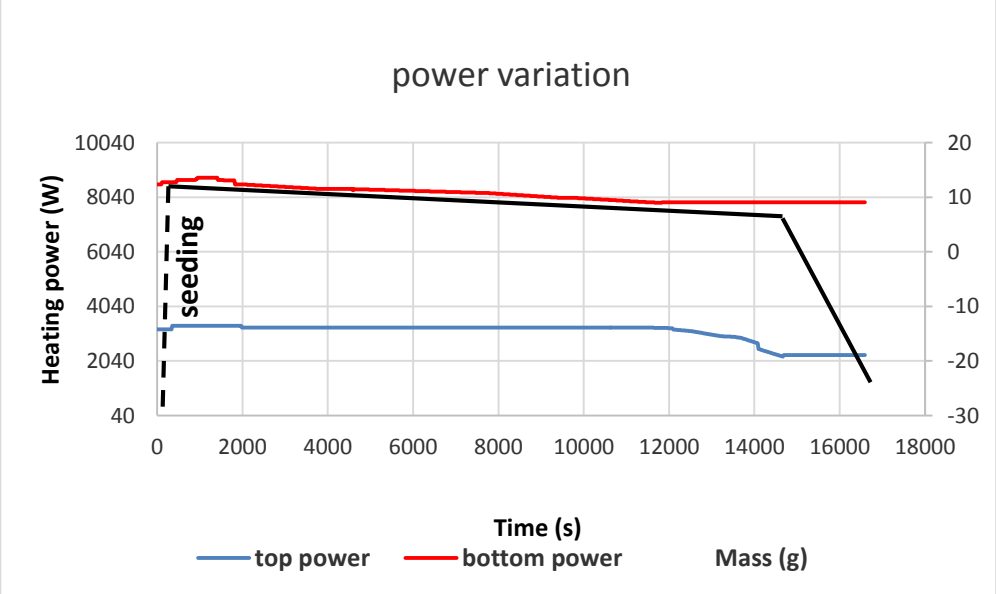

Figure 4. 12. Experimental power decrease for the growth of the symmetric crystal in the top and bottom heater next to the signal of the apparent mass of the crystal given by the high sensitivity balance.

Figure 4. 12 Gives the power in the top and the bottom heaters during the growth of the crystal. The included signal of the apparent mass given by the balance during the growth experiment shows clearly the first contact and forming of the meniscus, the stabilization, the first stage of the growth and finally the second stage of accelerated growth.

Notice that the first stage of the growth started by the decrease of the power in the lower heater. The power in the upper heater was stable to keep the temperature of the upper heater from falling down in order to avoid symmetry loss.

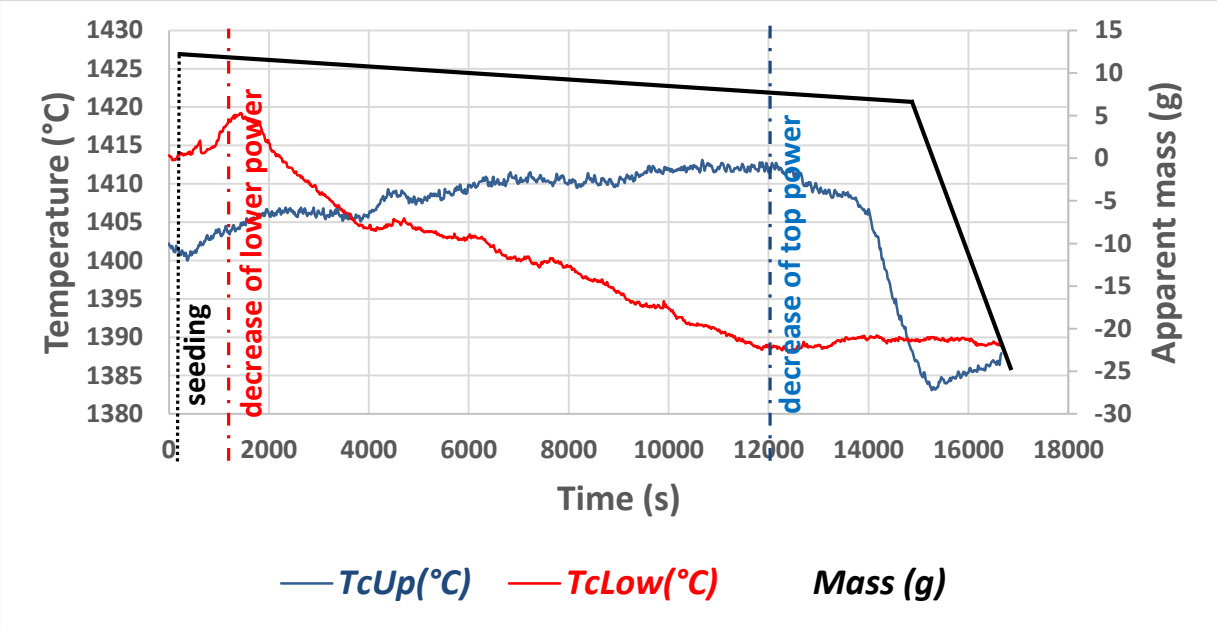

Figure 4. 13. Evolution of temperature in the top and bottom heaters during the growth of the experimental symmetric crystal case 1, next to the signal of the apparent mass of the crystal given by the high sensitivity balance.

Figure 4. 13 shows the variation of temperature in the top and bottom heaters. The link between this figure and the power figure can easily be made using the apparent mass curve appearing in both curves. The seeding contact is clearly defined by the sudden mass signal increases at the instant due to the forming of a meniscus.

A first stage of stabilization and growth was obtained by lowering the power in the bottom resistor by 800W at a rate of 340 W/h starting from and therefore lowering the temperature of the bottom heater from 1422°C to about 1390°C.

Knowing that there was no pull up during this experiment and once crystal mass is formed under the melt after the total solidification of the meniscus, the decrease of the apparent mass indicates that the crystal is growing inside the melt as described in chapter 2 Figure 2.18. The lateral resistor was continuously adjusted to maintain the temperature high on the side edges of the crucible to avoid crystallization from the crucible walls. The measured temperature on the exterior side walls of the crucible, at the same height with the melt surface, was 1405°C next to the corner and 1421°C next to the center of the crucible face. It was visually confirmed that the crystal started growing from the seed.

Note that the temperature of the top heater above the surface of the melt during the first phase of growth was close to the melting point minimizing the effect of radiative cooling of the melt surface in order to preserve symmetry as discussed in the prior section. A symmetric crystal started growing slowly from the seed to accumulate about 40g of real crystal mass at (13000s after seeding point). The growth was slow and the bottom heater reached a low temperature 25° below the melting point.

Although it was not possible to verify it experimentally, we suspect that solidification of silicon also started at the base of the crucible; such conclusion was observed by the numerical results showing solidification of silicon at the bottom of the crucible for similar conditions. At this stage, the temperature of the bottom resistor was kept stable and the power in the top resistor was decreased by 1000W at a rate of 750W/h starting from instant (12000s after seeding) to accelerate the growth of the crystal. 100 grams of silicon mass was solidified in about 30 minutes. The crystal was extracted after noticing agitation of the mass signal due to solid contact, probably with solidified dendrite from the crucible walls.

Estimation of growth rate can be obtained. Taking into account the bun shape of the crystal, the growth rate varies according to the growth direction. We may distinguish a maximum

and a minimum growth rates according to two major growth directions: vertical and horizontal. The vertical growth rate was the minimum value equal to 0.009 mm/s and the horizontal growth rate was the maximum value equal to 0.028 mm/s. The crystal was not monocrystalline but rather formed of large grains. Faceted growth can be observed in two facing parallel sides as seen in the top view of the crystal in Figure 4.1.b.

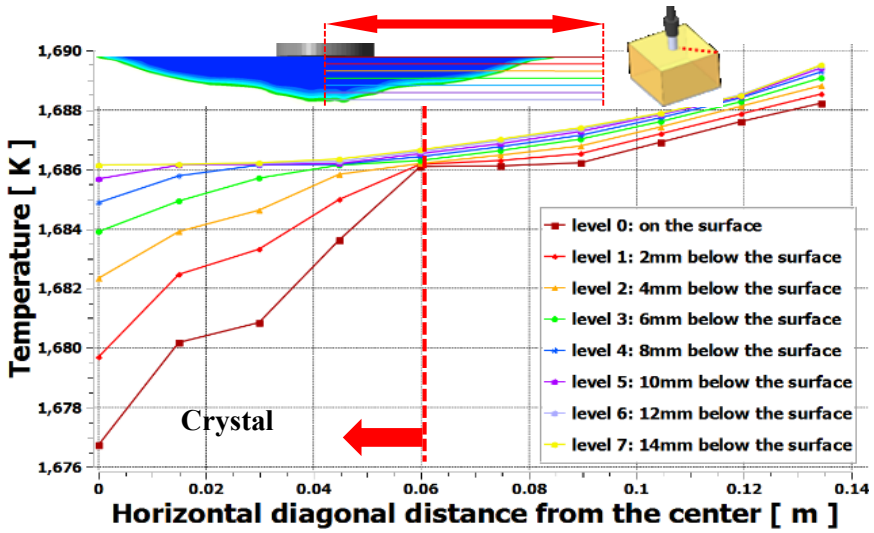

Figure 4. 14. Variation of temperature in the symmetric crystal and the melt along diagonal line taken at different horizontal levels from the free surface (2mm step)

Figure 4. 14 shows the temperature variation in the symmetric crystal. Compared to the asymmetric crystal profile (Figure 4. 8) the second derivative of temperature variation in the crystal is smaller. The extraction from the crystal is more homogeneous.

Further experiments succeeded to grow fully monocrystalline ingots. The same strategy of growth was applied by lowering the bottom heater to initiate a flat horizontal enlargement on the surface and then lowering the top heater to enhance the vertical growth. The obtained experimental crystal in case 4 is presented in Figure 4. 15. The growth parameters were similar to the numerical case with 15 rpm seed rotation and no pull up of the crystal. The crystal was extracted due to an emergency caused by a sudden technical shutdown of the power generator. The diameter of the crystal is 30 mm. The crystal is monocrystalline reproducing the original

orientation of the seed. The seed orientation was 100 in the vertical growth direction. Four facets of the <111> family, formed during the growth with crystal rotation.

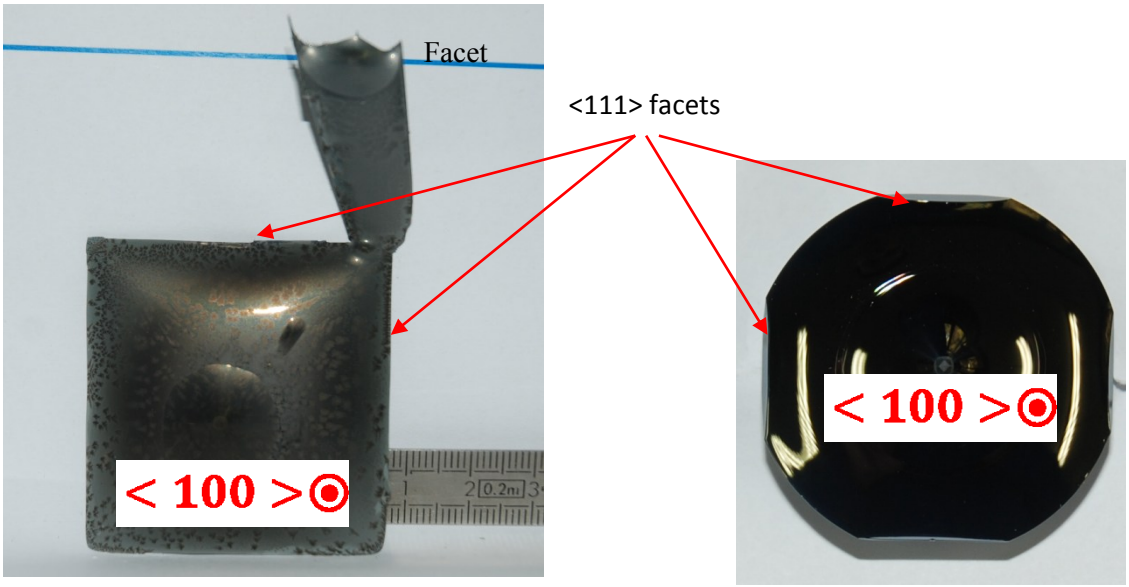

Figure 4. 15. Obtained symmetric silicon crystals in experimental cases 4 & 5. Monocrystalline showing facet growth where the horizontal cross section becomes a square shape

Figure 4. 16 shows the decrease of power during the cooling procedure. The dipping of the crystal can be clearly identified at the very beginning of the curve by the sudden increase of apparent mass due to the formation of the meniscus. Note that the cooling approach for crystal growth is similar to the one applied in the prior experimental case 3 as described by the numerical simulation of symmetric crystal growth. The approach is based on the proposed solution to resolve the asymmetry. Both numerical and experimental results show a systematic enhancement of the symmetry of the growth.

The cooling procedure starts by the decrease of the lower heater in the first stage of the growth. Note that the power in the upper heater is kept stable. In similar way with the prior described case 3, the decreasing apparent mass is an indication of growth inside the melt

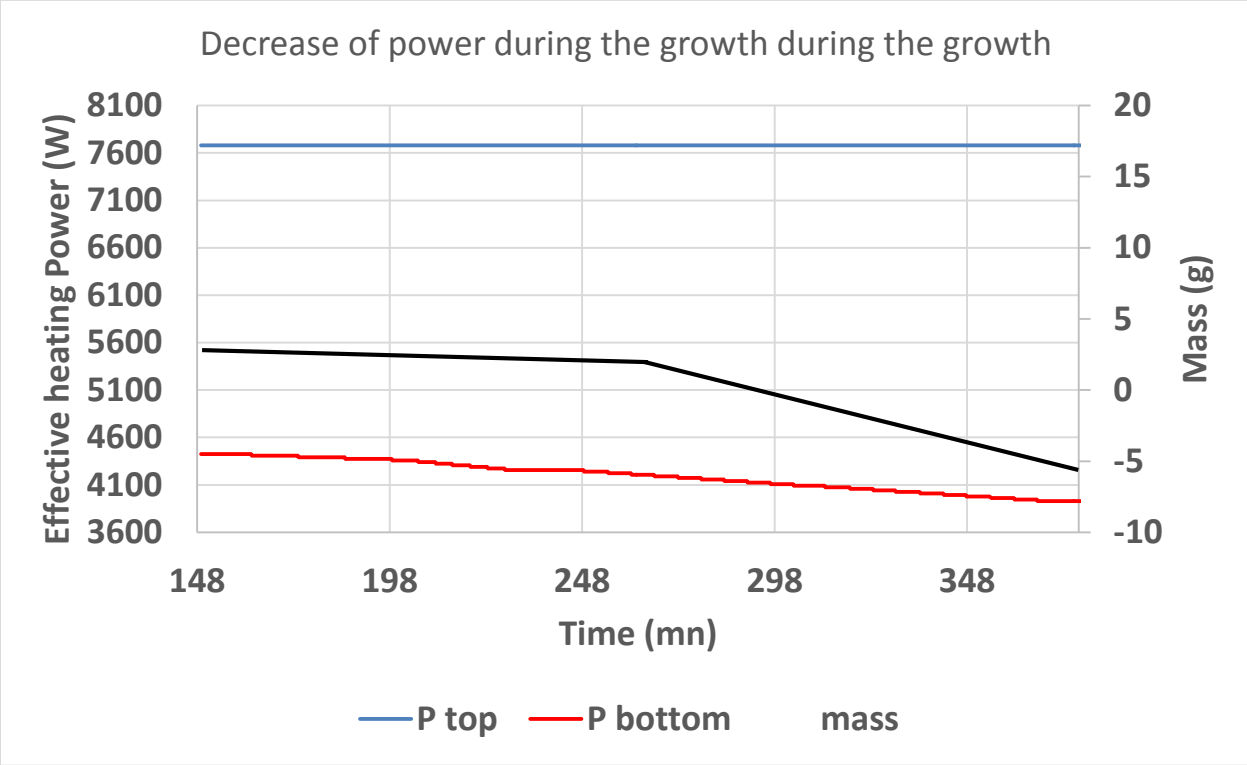

Figure 4. 16. Experimental power decrease for the growth of the symmetric crystal in the top and bottom heater next to the signal of the apparent mass of the crystal given by the high sensitivity balance. The side power is at 2387 W.

Figure 4. 17 shows the corresponding temperature of the upper and bottom heaters during the growth. Note that the temperature of the upper heater is kept close to the melting point of silicon. Note also that the temperature of the lower heater is decreasing and therefore cooling the general melt. Both crystals, were not at thermal equilibrium at the moment of extraction and therefore in a growing transient phase.

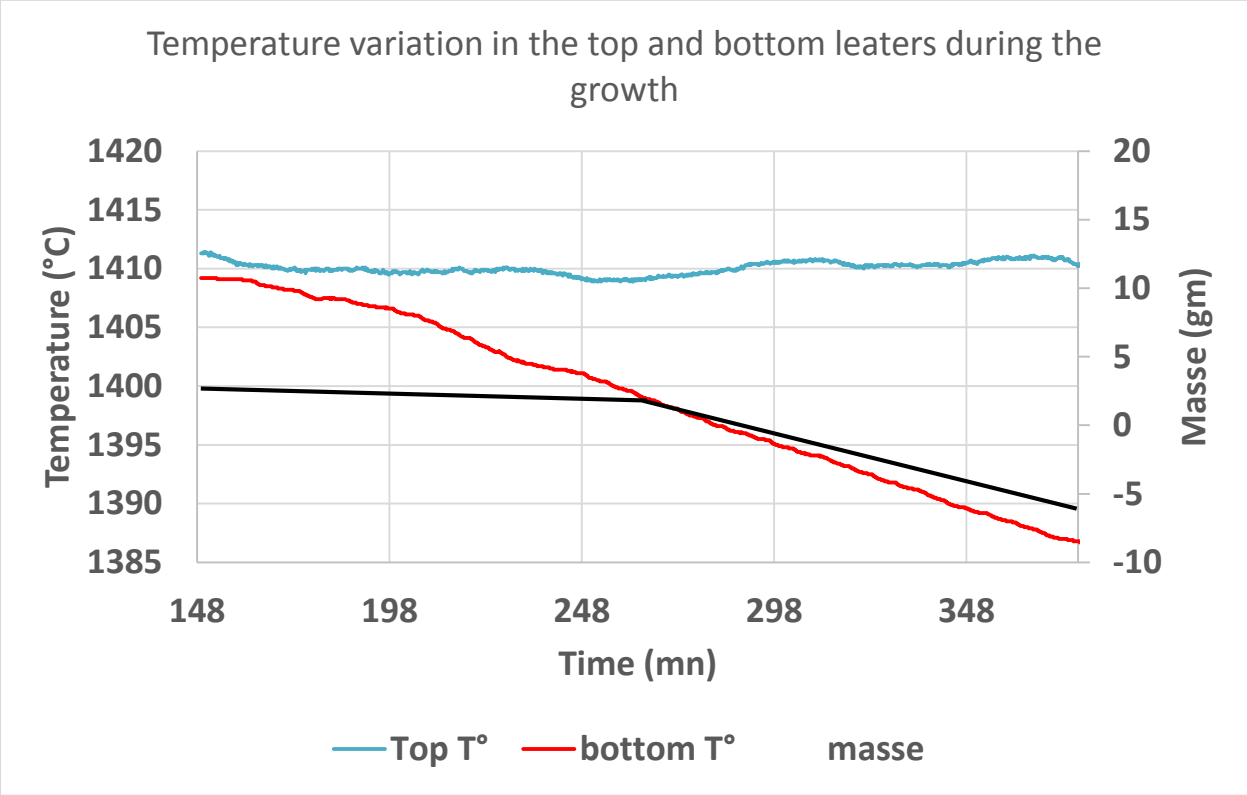

Figure 4. 17. Evolution of temperature in the top and bottom heaters during the growth of the experimental symmetric crystal case 1, next to the signal of the apparent mass of the crystal given by the high sensitivity balance.

In a comparable way, the decrease of power in the bottom heater initiates the first stage of the growth. The growth is on the surface and the enlargement of the crystal is mostly in the horizontal direction. Note that the top heater temperature is close to the melting point. if the growth is stable, and continuous, the top heater is then decreased to promote the growth in the vertical direction.

The developed Kyropoulos process is capable of stabilizing faceted growth. The growing monocrystalline ingots from a seed of <100> orientation in the vertical direction grow into a square. The square shape is mainly resulting from the kinetics of faceted growth.

IV.3. Conclusion of chapter four

The projection of the numerical analysis on experimental investigation explained important aspects of the crystal growth of silicon using Kyropoulos technique. The Kyropoulos process for silicon is sensitive to symmetry loss. The numerical analysis showed that this loss of symmetry, in the case of Kyropoulos for silicon, has physical causes. Numerical simulation showed that a coupled effect, between radiation cooling of the crystal and the decrease of the melt flow, is the leading cause for symmetry loss. The higher emissivity of the solid silicon compared to from phase accelerates the growth of any radiating part of the crystal on the top; the same crystal slowdown the nearest flow loop by local cooling of the melt which promotes the asymmetry to grow in the same direction. The two phenomena feed on each other which stabilizes the asymmetric growth.

Decrease of radiative cooling from the top by adjusting the top heater temperature and adding crystal rotation to homogenize the melt enhanced effectively the growth symmetry of the crystal. Symmetrical crystals were obtained successfully, numerically and experimentally using this approach. The approach of symmetric growth is consistent and repetitive which validates the proposed solution to preserve symmetry by reducing top radiation cooling and by adding rotation. These same results also validate implicitly the analysis of asymmetric growth causes proving that the strong coupling between radiation cooling on the top the melt and the altered melt flow due to the low temperature of the crystal has a validated physical foundation.

The approach of decreasing the radiation cooling from the top reinforces the basic principle of low thermal gradient in the melt, at least in the beginning of the seeding process. Monocrystalline silicon growth with facets was proven experimentally to be possible using the same conditions. The obtained crystals were perfectly square taking advantage of the faceted growth. The crystal were rather flat as described by the numerical model. An alternation of pull up and fixe growth is proposed to enhance the mass growth rate in the vertical direction for future investigations.

V. General conclusion & outlooks

The present work investigates the possibility to use Kyropoulos crystal growth method for the production of monocrystalline silicon ingots. This top seeding process is based on an unconfined growth environment where the top seeding area is the cold zone in the melt. The crystal grows inside the melt without contact from the crucible.

The method has the potential to produce high quality large silicon ingots with a flat aspect ratio. In addition, the process may control the final shape of the growth to make it square without solid contact with the crucible. Such advantages are expected to reduce the consequent material loss from the cutting of the cylindrical ingot into a square brick in order to obtain a square wafer for photovoltaic applications.

An experimental Kyropoulos configuration with a square crucible of G1 size and three heating elements (top, bottom and side) was investigated for the development of the process. A 3D numerical model of the full furnace was created and validated using experimental data. The numerical model included heat transfer, fluid dynamics in the melt, solidification and crystal rotation. The process was simulated using fluent ANSYS code.

A preliminary assessment of the melt flow showed that the melt is mainly driven by floatability forces while the contribution of Marangoni effect and crystal rotation stay localized and negligible on the scale of the total melt. Although the flow in this configuration is mainly laminar in transition to turbulent, a turbulent numerical model was required to obtain satisfactory convergence.

The modeling of solidification using the default native enthalpy porosity solidification module in Fluent suffered from the absence of a proper convergence criteria for latent heat calculations. In addition, the displacement of the partially solidified melt was also identified as a limiting problem for the solidification module in Fluent. An implemented user defined subroutine, as a convergence criteria, next to the determination of the proper operating A_{msuh} parameter enhanced the convergence and accuracy of solidification simulation. The obtained numerical model was validated with experimental data.

The development of the process was initiated from a starting configuration designed as a reverse directional solidification process. The starting configuration presented several issues where the flow was ascendant in the center and descending/moving downwards in the corners making the seeding area as the hot spot and prohibiting therefore the growth from the seed. Numerical investigation showed that the seeding zone is receiving consequent heat by radiation from the

top heater. The leading points in the development of the process were then summarized in the following:

- Localized heat extraction techniques are required to target the central part of the melt surface.
- The vertical and horizontal gradients need to be controlled in order to make the top central seeding zone the coldest spot
- The required flow should be ascendant in the center and descending in the corners
- The heat extraction from the top must be sufficient to initiate the growth and the enlargement of the ingot diameter
- Control of the growth by the weight since the growth will be in the opaque liquid

As a consequence, a second developed configuration was proposed with a ceramic radiation shield to protect the seeding parts from the heat in order to enhance localized heat extraction from the seeding zone. Growth from the seed was found to be possible as well as the enlargement of the ingot. The installed thermal gradient and the desired melt flow direction stayed consistent during the decrease of power for the enlargement of the crystal. The simulated growth was rather flat, where the horizontal growth is higher compared to the vertical growth.

A third developed configuration with the addition of a cold heat sink in the top was proposed to enhance the heat extraction from the seed. The configuration offered a localized heat extraction point to enhance dipping conditions where growth from the seed was possible.

All the simulated ingots had a flat bun shape inside the melt. The horizontal growth was faster compared to the vertical one. The vertical growth was limited by the state of thermal equilibrium in the crystal depending very much on heat extraction capacity from the top of the growing ingot. The maximum possible geometric aspect ratio vertical/horizontal for the obtained growth was equal to 1/3. The average growth rate was about 6-7 cm/h. an alternation of growth inside the melt and a slow pull up, as described by MENZIES AND J. SKINNER [24], can be proposed to promote the vertical growth. Providing that the horizontal growth of the ingot was only limited by the size of the crucible, the method can expect a consequent total mass growth rates even at very small pull up velocity if the proper scaling is done.

The Kyropoulos process for silicon was found to be sensitive to symmetry loss. Numerical simulation showed that a coupled effect, between radiation cooling of the crystal and the decrease of the melt flow, is the leading cause for symmetry loss. The higher emissivity of solid silicon during solidification rose the radiative cooling of the crystal which cooled down locally the nearest melt. Similarly, the slowing colder melt increased locally the rate of crystal growth. The

two phenomena fed on each other accelerating the growth of any appearing dissymmetry in one preferential direction.

Control of radiative cooling by adjusting the right heating parameters at the top heater, to be close to the melting temperature, and homogenization of the melt by crystal rotation allowed a consistent symmetric crystal growth. As a consequence, symmetric silicon crystals growth was simulated numerically and validated experimentally.

The numerical results show that the horizontal growth in Kyropoulos method can cover a large area of the crucible approaching closely the crucible walls. Two different approaches were proposed and investigated numerically for the thermal control of the ingot in order to obtain a square shape of the horizontal cross section:

- The use of conductive thermal diffusion from the crucible walls to reshape the final ingot
- The use of convection to reshape the final ingot into a square shape

For the first approach, the use of heat diffusion from the crucible wall was found effective to reshape the solid liquid interface for a Peclet number close to 1. Such condition was only verified at short distance from the crucible wall. The ingot inherited the shape of the crucible wall to become a square except in the corners. The corners had stronger convection loops restricting the growth of the ingot towards the corners. It became obvious that the accomplishment of a full square shape based on this approach requires non uniform heating of the side walls to decrease the effect of the corners. The approach had the advantage to allow a horizontal growth that fills most of the horizontal section of the crucible.

For the second approach, the use of convection loops coming from the corners of the crucible was found capable to reshape the ingot into a square shape. The resulting square shape was rotated 45° along the vertical axial line, compared to the crucible walls. The obtained ingot was smaller than the total surface of the melt covering about 65% of the surface area.

Both approaches require precise control of the heat exchange which needs to be consistent and reproductive between the different runs. Such task needs further investigation since it is a challenging engineering task for large scale furnaces where the main parts, especially the insulation, are subject to aging deterioration.

The experimental investigation showed a third possibility to obtain a square shape ingots. The developed experimental prototype for symmetric growth succeeded to grow monocrystalline silicon crystals with stabilized faceted growth in the <111> direction. The faceted monocrystalline crystals finished in a square shape. The square shape of the ingot was related to the kinetics of facetted crystal growth.

A true maturity of Kyropoulos process requires more in depth investigation. As mentioned by Bliss in 2014 [20], Understanding of convection and heat transport, especially radiation, using numerical simulation is required both for the development and the scaling phases. Such numerical investigation will also be beneficial for the design in order to enhance the control of the solidification interface shape and thermal stresses. In addition, it is important to investigate the dopant and impurities distribution in the process. Several aspects of the process are not yet fully understood such as the effect of the crucible and the crystal rotation. Similarly other additions such as magnetic field, to calm down the melt, is also an investigation of interest for further development of the process.

The present work studied the effects of melt flow, heat transfer and crystal rotation on crystal growth of silicon in Kyropoulos process. The obtained results show that Kyropoulos process can grow silicon ingots of flat aspect ratio with consequent horizontal growth, covering large area of the crucible. The process offers the possibility to control the shape of the ingot to obtain a square horizontal cross section. These advantages are well suited for photovoltaic applications.

The discussed effects of convection and radiation on growth symmetry and crystal enlargement requires to be properly projected on large scale industrial furnaces. Further development of the numerical investigation will benefit from including the effect of melt flow on both heat and mass transfer for proper understanding of the impurities distribution. Crystalline defects and dislocations are a major interest in Kyropoulos process and should be investigated as part of future development of a full numerical model for Kyropoulos process for silicon.

Since the applied interest for this work is numerical investigation of silicon production for photovoltaic application, future investigation should discuss more in details the points of interests in Kyropoulos and its impact on the photovoltaic wafer. The shape, the aspect ratio and the quality of the ingot, at larger scale are crucial points to be investigated numerically and validated experimentally to clarify the impact of the process on the quality of the obtained solar cells. Such understanding will be valuable for future orientation for the development of the numerical investigation.

References

[1] "International Energy Outlook 2016-World energy demand and economc outlook - Energy Information Administration." [Online]. Available: http://www.eia.gov/forecasts/ieo/world.cfm. [Accessed: 11-Sep-2016].

[2] "World Energy Outlook 2015: Presentation to Press." [Online]. Available: http://www.slideshare.net/internationalenergyagency/151110-weo2015-presentation.

[3] I. Energy Agency, "Key World Energy Statistics 2015."

[4] Philipp Beiter, "2014 Renewable Energy Data Book," 2014.

[5] A. de La Tour, M. Glachant, and Y. Ménière, "Predicting the costs of photovoltaic solar modules in 2020 using experience curve models," *Energy*, vol. 62, pp. 341–348, Dec. 2013.

[6] C. N. Kost Johannes Mayer Jessica Thomsen Niklas Hartmann Charlotte Senkpiel Simon Philipps Sebastian Nold Simon Lude Noha Saad Thomas Schlegl, D. Wi-Ing Christoph Kost, D. N. Phys oec Johannes Mayer, T. Schlegl, and E. R. Weber, "Levelized Cost of Electricity Renewable Energy Technologies."

[7] S. Pizzini, Ed., "Advanced Silicon Materials for Photovoltaic Applications," John Wiley & Sons, Ltd, 2012, pp. i–xvi.

[8] A. F. B. Braga, S. P. Moreira, P. R. Zampieri, J. M. G. Bacchin, and P. R. Mei, "New processes for the production of solar-grade polycrystalline silicon: A review," *Sol. Energy Mater. Sol. Cells*, vol. 92, no. 4, pp. 418–424, Apr. 2008.

[9] A. Jouini, D. Ponthenier, H. Lignier, N. Enjalbert, B. Marie, B. Drevet, E. Pihan, C. Cayron, T. Lafford, and D. Camel, "Improved multicrystalline silicon ingot crystal quality through seed growth for high efficiency solar cells," *Prog. Photovoltaics Res. Appl.*, vol. 20, no. 6, pp. 735–746, Sep. 2012.

[10] X. Gu, X. Yu, K. Guo, L. Chen, D. Wang, and D. Yang, "Seed-assisted cast quasi-single crystalline silicon for photovoltaic application: Towards high efficiency and low cost silicon solar cells," *Sol. Energy Mater. Sol. Cells*, vol. 101, pp. 95–101, 2012.

[11] I. Guerrero, V. Parra, T. Carballo, A. Black, M. Miranda, D. Cancillo, B. Moralejo, J. Jiménez, J.-F. Lelièvre, and C. del Cañizo, "About the origin of low wafer performance and crystal defect generation on seed-cast growth of industrial *mono-like* silicon ingots," *Prog. Photovoltaics Res. Appl.*, vol. 22, no. 8, pp. 923–932, Aug. 2014.

[12] K. Nakajima, R. Murai, K. Morishita, K. Kutsukake, and N. Usami, "Growth of multicrystalline Si ingots using noncontact crucible method for reduction of stress," *J. Cryst. Growth*, vol. 344, no. 1, pp. 6–11, Apr. 2012.

[13] T.-H. Tsai, "Silicon sawing waste treatment by electrophoresis and gravitational settling," *J. Hazard. Mater.*, vol. 189, no. 1, pp. 526–530, 2011.

[14] B. Gao, S. Nakano, H. Harada, Y. Miyamura, T. Sekiguchi, K. Kakimoto, B. Gao, S. Nakano, H. Harada, Y. Miyamura, T. Sekiguchi, and K. Kakimoto, "Single-Seed Casting Large-Size Monocrystalline Silicon for High-Efficiency and Low-Cost Solar Cells," *Engineering*, vol. 1, no. 3, pp. 378–383, Sep. 2015.

[15] "Photovoltaic – DSS^{TM} 850." [Online]. Available: http://www.gtat.com/products-and-services-photovoltaic-dss-850.htm.

[16] H. Lautenschlager, F. Lutz, C. Schetter, U. Schubert, and R. Schindler, "MC-silicon solar cells with <17% efficiency," in *Conference Record of the Twenty Sixth IEEE Photovoltaic Specialists Conference - 1997*, pp. 7–12.

[17] M. S. Akselrod and F. J. Bruni, "Modern trends in crystal growth and new applications of sapphire," *J. Cryst. Growth*, vol. 360, pp. 134–145, Dec. 2012.

[18] H. Zhang, X. Ma, B. Zhao, C. Wang, and F. Xu, "Nucleation and bulk growth control for high efficiency silicon ingot casting," *J. Cryst. Growth*, vol. 318, no. 1, pp. 283–287, 2011.

[19] P. S. Ravishankar, "Kyropolous crystal growth of silicon for solar cel.pdf," *Sol. Energy Mater.*, vol. 12, no. 5, pp. 361–369, Nov. 1985.

[20] David F. Bliss, "Evolution and application of the Kyropoulos crystal growth method - page 29 - 50 Years Progress in Crystal Growth | 978-0-444-51650-3 | Elsevier." 2014

[21] S. Kyropoulos, "Ein Verfahren zur Herstellung großer Kristalle," *Zeitschrift für Anorg. und Allg. Chemie*, vol. 154, no. 1, pp. 308–313, Jun. 1926.

[22] E. Schönherr, "Characterization of shape and heat flow in melt-grown crystals by an affective seed radius," *J. Cryst. Growth*, vol. 3–4, pp. 265–267, Jan. 1968.

[23] K. Korth, "Dispersionsmessungen an Kaliumbromid und Kaliumjodid im Ultraroten," *Zeitschrift für Phys.*, vol. 84, no. 11–12, pp. 677–685, Nov. 1933.

[24] A. C. Menzies and J. Skinner, "The growing of crystals by the methods of Kyropoulos and of Stöber," *Discuss. Faraday Soc.*, vol. 5, no. 0, pp. 306–312, Jan. 1949.

[25] K. Chamberlain, "The Growing of Large, Single Crystals of Potassium Bromide," *Rev. Sci. Instrum.*, vol. 9, no. 10, pp. 322–324, Oct. 1938.

[26] J. P. Ciraldo, J. Levine, and H. Ganegoda, "Improvements to crystal quality of sapphire grown by the Kyropoulos method," 2014, vol. 9127, p. 91271C–91271C–7.

[27] P. Rudolph, "Fundamentals and engineering of defects," *Prog. Cryst. Growth Charact. Mater.*, vol. 62, no. 2, pp. 89–110, 2016.

[28] M. Velazquez and P. Veber, "Méthodes de cristallogenèse par solidification pour l'élaboration de cristaux massifs," p. 21, 2015.

[29] K. Nakajima, R. Murai, S. Ono, K. Morishita, M. M. Kivambe, D. M. Powell, and T. Buonassisi, "Shape and quality of Si single bulk crystals grown inside Si melts using the noncontact crucible method," *Jpn. J. Appl. Phys.*, vol. 54, no. 1, p. 15504, Dec. 2014.

[30] K. Nakajima, R. Murai, and K. Morishita, "Growth of square Si single bulk crystals with large side-face widths using noncontact crucible method," *Jpn. J. Appl. Phys.*, vol. 53, no. 2, p. 25501, Jan. 2014.

[31] K. Nakajima, S. Ono, R. Murai, and Y. Kaneko, "Growth of Si Bulk Crystals with Large Diameter Ratio

Using Small Crucibles by Creating a Large Low-Temperature Region Inside a Si Melt Contained in an NOC Furnace Developed Using Two Zone Heaters," *J. Electron. Mater.*, vol. 45, no. 6, pp. 2837–2846, Jun. 2016.

[32] D. T. J. Hurle, "Convective transport in melt growth systems," *J. Cryst. Growth*, vol. 65, no. 1, pp. 124–132, Dec. 1983.

[33] D. Franke, T. Rettelbach, C. Häßler, W. Koch, and A. Müller, "Silicon ingot casting: process development by numerical simulations," *Sol. Energy Mater. Sol. Cells*, vol. 72, no. 1, pp. 83–92, 2002.

[34] I. Steinbach, M. Apel, T. Rettelbach, and D. Franke, "Numerical simulations for silicon crystallization processes—examples from ingot and ribbon casting," *Sol. Energy Mater. Sol. Cells*, vol. 72, no. 1, pp. 59–68, 2002.

[35] O. Bertrand, B. Binet, H. Combeau, S. Couturier, Y. Delannoy, D. Gobin, M. Lacroix, P. Le Quéré, M. Médale, J. Mencinger, H. Sadat, and G. Vieira, "Melting driven by natural convection A comparison exercise: first results," *Int. J. Therm. Sci.*, vol. 38, no. 1, pp. 5–26, 1999.

[36] H. Miyazawa, L. Liu, S. Hisamatsu, and K. Kakimoto, "Numerical analysis of the influence of tilt of crucibles on interface shape and fields of temperature and velocity in the unidirectional solidification process," *J. Cryst. Growth*, vol. 310, no. 6, pp. 1034–1039, 2008.

[37] A. Popescu and D. Vizman, "Numerical Study of Melt Convection and Interface Shape in a Pilot Furnace for Unidirectional Solidification of Multicrystalline Silicon," *Cryst. Growth Des.*, vol. 12, no. 1, pp. 320–325, Jan. 2012.

[38] D. Vizman, J. Friedrich, and G. Mueller, "3D time-dependent numerical study of the influence of the melt flow on the interface shape in a silicon ingot casting process," *J. Cryst. Growth*, vol. 303, no. 1, pp. 231–235, May 2007.

[39] X. Huang, T. Taishi, T. Wang, and K. Hoshikawa, "Measurement of temperature gradient in Czochralski silicon crystal growth," *J. Cryst. Growth*, vol. 229, no. 1, pp. 6–10, 2001.

[40] K. Kakimoto, M. Watanabe, M. Eguchi, and T. Hibiya, "Ordered structure in non-axisymmetric flow of silicon melt convection," *J. Cryst. Growth*, vol. 126, no. 2, pp. 435–440, 1993.

[41] A. Muiznieks, A. Krauze, and B. Nacke, "Convective phenomena in large melts including magnetic fields," *J. Cryst. Growth*, vol. 303, no. 1, pp. 211–220, 2007.

[42] K. Kakimoto, M. Eguchi, H. Watanabe, and T. Hibiya, "Flow instability of molten silicon in the Czochralski configuration," *J. Cryst. Growth*, vol. 102, no. 1, pp. 16–20, Apr. 1990.

[43] H. S. Fang, Z. L. Jin, M. J. Zhang, Z. Zhang, and C. J. Zhao, "Role of internal radiation at the different growth stages of sapphire by Kyropoulos method," *Int. J. Heat Mass Transf.*, vol. 67, pp. 967–973, 2013.

[44] C.-H. Chen, J.-C. Chen, C.-W. Lu, and C.-M. Liu, "Numerical simulation of heat and fluid flows for sapphire single crystal growth by the Kyropoulos method," *J. Cryst. Growth*, vol. 318, no. 1, pp. 162–167, 2011.

[45] H. Fang, Z. Zhang, Z. Jin, S. Wang, and J. Xu, “Characteristics of melt convection during Kyropoulos sapphire crystal growth,” *Int. J. Mater. Res.*, vol. 105, no. 10, pp. 961–967, Oct. 2014.

[46] S. E. Demina, E. N. Bystrova, V. S. Postolov, E. V. Eskov, M. V. Nikolenko, D. A. Marshanin, V. S. Yuferev, and V. V. Kalaev, “Use of numerical simulation for growing high-quality sapphire crystals by the Kyropoulos method,” *J. Cryst. Growth*, vol. 310, no. 7–9, pp. 1443–1447, Apr. 2008.

[47] S. E. Demina, E. N. Bystrova, M. A. Lukanina, V. M. Mamedov, V. S. Yuferev, E. V. Eskov, M. V. Nikolenko, V. S. Postolov, and V. V. Kalaev, “Numerical analysis of sapphire crystal growth by the Kyropoulos technique,” *Opt. Mater. (Amst).*, vol. 30, no. 1, pp. 62–65, 2007.

[48] A. Popescu and D. Vizman, “Numerical study of the influence of melt convection on the crucible dissolution rate in a silicon directional solidification process,” *Int. J. Heat Mass Transf.*, vol. 54, no. 25–26, pp. 5540–5544, Dec. 2011.

[49] V. V. Timofeev, V. V. Kalaev, and V. G. Ivanov, “3D melt convection in sapphire crystal growth: Evaluation of physical properties,” *Int. J. Heat Mass Transf.*, vol. 87, pp. 42–48, Aug. 2015.

Appendix 1

Determination of the required power distribution to obtain a seeding point

Kyropoulos process requires a melt where the seeding central point on the surface is at lower temperature. The following algorithm was used to obtain the required set of power distribution for the seeding state based on these conditions (temperature of the seeding point, minimum temperature on the side edge wall of silicon charge, minimum temperature on the bottom wall of the silicon charge, vertical and horizontal ΔT)

1) **First part: Conditions based on absolute temperatures on the edge walls**
    - The seeding point T_{seed} is at (T_m + 2 °K)
    - The minimum temperature on the silicon side wall T_{side} is above (T_m + 2 °K)
    - The minimum temperature on the silicon bottom wall T_{bottom} is above (T_m + 2 °K)
2) **Second part: Conditions based on relative horizontal and vertical ΔT**
    - The seeding point is at (T_m + 2 °K)
    - The temperature difference along to the central vertical axis is 10°K
    - The temperature difference according to the diagonal line on the surface is 10°K

The algorithm iterates by upgrading the power according to the proposed conditions and resolving the case.

- The seeding temperature was mainly controlled by adjusting the power in the top heater
- The horizontal ΔT was adjusted using the power in the side heater
- The vertical ΔT was mainly adjusted using the power in the bottom heater.

End of Appendix 1

Appendix 2

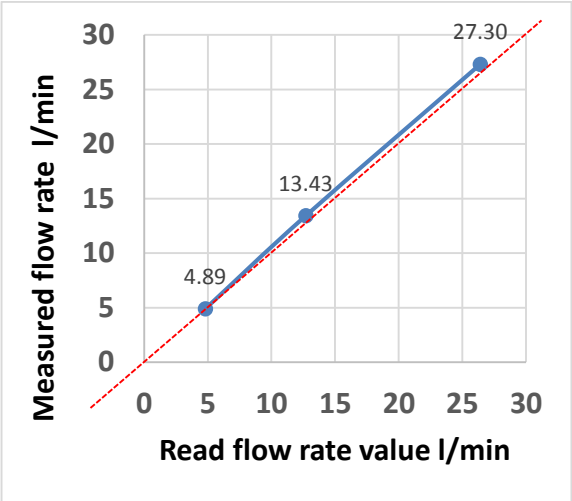

Comparison of measured and read values of water flow rates in the cooling system for the verification of credibility of flow measurements

The cooling water in the experimental furnace was monitored by flow meters. The verified measurement error was less than 2% in the range of used flow (3 to 30 l/min).

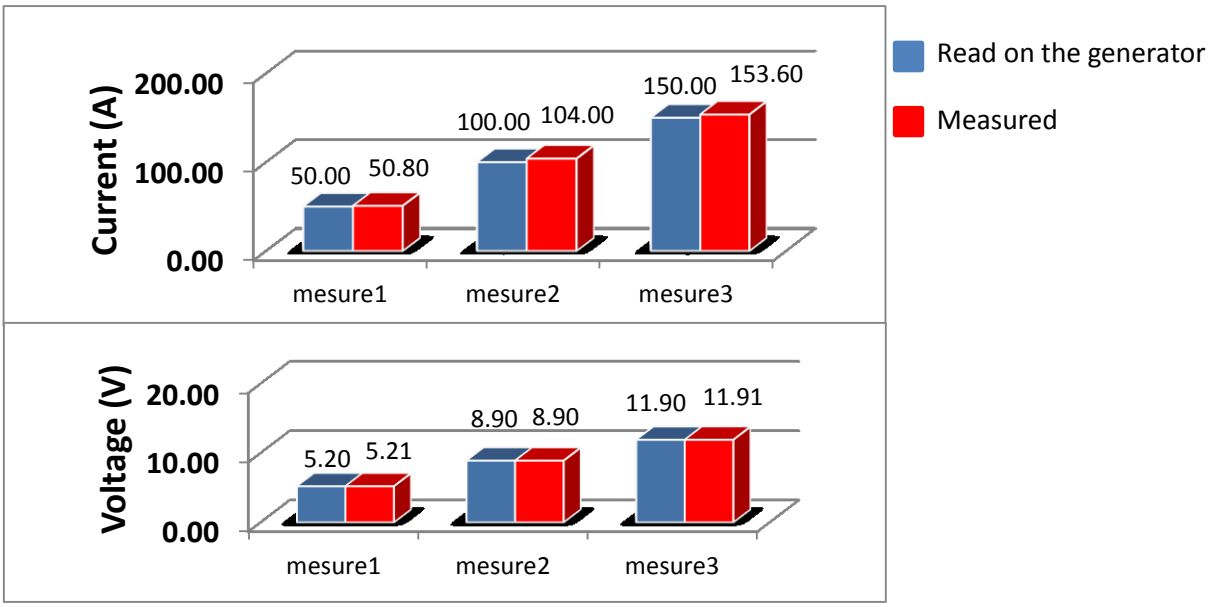

Comparison between measured and read values of tension and current in the generator

The power delivered by the generator was monitored and registered by mean of current and tension values. These values were acquired directly on the generator.

A set of manual measurements, using high precision voltmeter and ammeter, was performed to verify the accuracy of the readings. The error in power measurements was less than 4%.

End of Appendix 2